

**MINIATURIZED DIFFRACTION BASED
INTERFEROMETRIC DISTANCE
MEASUREMENT SENSOR**

A Thesis
Presented to
The Academic Faculty

By

Byungki Kim

In Partial Fulfillment of the Requirements for
the Degree Doctor of Philosophy
in Mechanical Engineering

Georgia Institute of Technology
July 2004

Copyright © 2004 by Byungki Kim

**MINIATURIZED DIFFRACTION BASED
INTERFEROMETRIC DISTANCE
MEASUREMENT SENSOR**

Approved by:

Dr. Thomas R. Kurfess, Advisor

Dr. F. Levent Degertekin, Advisor

Dr. Peter J. Hesketh

Dr. Thomas K. Gaylord

Dr. Farrokh Ayazi

July 6, 2004

DEDICATION

To my family:

My wife, Yunah

My two daughters, Yoojin, Irene

For their love and understanding.

ACKNOWLEDGMENT

First and foremost, I would like to thank the Lord blessing me and allowing me such opportunities as to initiate and complete my Ph.D. I would like to thank my advisor, Dr. Thomas Kurfess for his support and encouragement to get through many obstacles in this research. I would like to thank my advisor, Dr. Levent Degertekin for his support and guidance throughout the completion of the dissertation. It is not possible to complete Ph.D. without my advisors' feedback and insight. I have really enjoyed and felt fruitfulness during my working with them at Georgia Tech. I would like to thank my reading committee, Dr. Thomas Gaylord, Dr. Peter Hesketh, and Dr. Farrokh Ayazi for their comments and support. I would like to thank my colleagues at PMRC and MIST, especially Mike, Wook, and Ali for their contribution and support for this research, and Neal, Jeff, Guclu and James for their support and valuable discussion. I would like to thank MIRC cleanroom users and staffs for their comments and suggestions, especially Moses and Seungkeun for helping me to dice my wafers. I would like to thank Dr. Ravi at PRC and Steven at PRMI for helping me to use their facilities. I would like to thank my family and parents for their love and understanding.

This work has been funded by National Science Foundation under Grant Number DMI-0200331 and funded by Faculty Research Commercialization Program at Georgia Tech. The government has certain rights in this material. Any opinion, finding and conclusions or recommendation are those of author and do not necessarily reflect the views of the National Science Foundation.

TABLE OF CONTENTS

DEDICATION.....	iii
ACKNOWLEDGMENT	iv
TABLE OF CONTENTS.....	iv
LIST OF TABLES.....	x
LIST OF FIGURES	xi
NOMENCLATURE	xix
SUMMARY.....	xxi
CHAPTER 1	1
INTRODUCTION	1
1.1 MOTIVATION.....	1
1.2 PROBLEM STATEMENT.....	2
1.3 THESIS OUTLINE.....	5

CHAPTER 2	7
LITERATURE REVIEW	7
2.1 3-D METROLOGY	7
2.1.1 CONTACT METHODS	7
2.1.2 NONCONTACT METHODS.....	8
2.2 MEMS METROLOGY.....	11
2.3 MICROLENS AND GRATING.....	12
2.4 VERTICAL TRAVEL ACTUATOR.....	13
CHAPTER 3	15
DESIGN AND ANALYSIS	15
3.1 DESIGN STUDY FOR GRATING MICROINTERFEROMETER.....	15
3.1.1 MICHELSON INTERFEROMETER.....	16
3.1.2 DIFFRACTION BASED OPTICAL DISPLACEMENT DETECTION	17
3.1.3 FOCUS SENSING.....	21
3.1.4 SENSOR STRUCTURE.....	22
3.1.5 SCALAR DIFFRACTION THEORY	27
3.1.6 COUPLED-WAVE ANALYSIS.....	28
3.1.7 PHASE DISTRIBUTION IN PLANO-CONVEX LENS	33
3.1.8 SYSTEM SIMULATION.....	35
3.1.9 EXPERIMENTAL VALIDATION OF FEASIBILITY ANALYSIS.....	44

3.2 MICROLENS	48
3.3 DEFORMABLE GRATING	50
3.3.1 DESIGN PARAMETERS STUDY	50
3.3.2 FEM ANALYSIS.....	56
3.4 MICROMACHINED SCANNING INTERFROMETER	69
3.5 SUMMARY	70
CHAPTER 4	72
FABRICATION	72
4.1 MICROLENS	73
4.1.1 PROCESS DEVELOPMENT	73
4.1.2 CHARACTERIZATION	77
4.2 DEFORMABLE GRATING	82
4.2.1 PROCESS DEVELOPMENT	82
4.2.2 CHARACTERIZATION	93
4.3 INTEGRATED SYSTEM	98
4.3.1 MICROLENS AND DEFORMABLE GRATING INTEGRATION.....	98
4.3.2 INTEGRATED OPTOELECTRONICS.....	99
4.3.3 PACKAGING	102
4.4 SUMMARY	105
CHAPTER 5	106

EXPERIMENTS	106
5.1 SINGLE POINT MEASUREMENT	106
5.2 PHASE SENSITIVE DETECTION	110
5.3 LATERAL IMAGING PERFORMANCE	113
5.4 DC METROLOGY PERFORMANCE	115
5.4.1 EXPERIMENT WITH A NON-INTEGRATED μ SI.....	115
5.4.2 EXPERIMENT WITH AN INTEGRATED μ SI.....	120
5.5 VIBRATION AND MODE SHAPE MEASUREMENT	125
5.5.1 EXPERIMENT WITH A NON-INTEGRATED μ SI.....	125
5.5.2 EXPERIMENT WITH AN INTEGRATED μ SI.....	129
5.6 NOISE.....	132
5.7 EFFECT OF CONTROL	137
5.8 INTEGRATED SYSTEM	144
5.9 SUMMARY	146
CHAPTER 6	148
DISCUSSION AND CONCLUSION.....	148
6.1 SUMMARY	148
6.2 CONCLUSION.....	150
6.3 CONTRIBUTION.....	150
6.4 RECOMMENDATION AND FUTURE WORK.....	153

APPENDICES 155

BIBLIOGRAPHY 161

LIST OF TABLES

Table 1. Technology comparison for MEMS measurement techniques [8]	3
Table 2. The field and the angular spectrum at specific z coordinate.....	36
Table 3. Comparison of location of each diffracted order	46
Table 4. Distances at each plane from the scale 0 plane.....	80
Table 5. DC sputterer process time vs. aluminum deposition thickness	159

LIST OF FIGURES

Figure 1. A schematic of a μ SI with a photo detector.....	5
Figure 2. Schematic of Michelson interferometer	16
Figure 3. Detector signal when the target moves at constant speed	17
Figure 4. Schematics showing that the diffraction pattern depends on distance to reflecting surface	18
Figure 5. Distribution of the reflected light on an observation plane	20
Figure 6. The variation of the intensity of the zeroth and first diffraction order with distance d on an observation plane	20
Figure 7. Schematic of a regular focus sensing system	21
Figure 8. Intensity at the detection as a function of normalized distance to object surface	22
Figure 9. Schematic of a focus sensing system with an integrated diffraction grating for distance measurement.....	23
Figure 10. Calculated first diffraction order intensity as a function of distance from the focal point of the lens. The envelope is the intensity of Figure 8.....	24
Figure 11 Schematic of a focus sensing system with an integrated diffraction grating at wafer level	25
Figure 12. Schematic of a μ SI	26
Figure 13. Schematic of a μ SI with photo diode integration	26
Figure 14. Coordinate system for angular spectrum calculation	28
Figure 15. Schematic of a diffraction-based acoustic sensor [95]	29

Figure 16. Calculated reflected diffraction efficiencies of the zero order $[DE_0(0)]$ and first order $[DE_0(\pm 1)]$ for $\Lambda = 4 \mu\text{m}$. [95]	31
Figure 17. Calculated reflected diffraction efficiencies of the zero order $[DE_0(0)]$ and first order $[DE_0(\pm 1)]$ for $\Lambda = 2 \mu\text{m}$. [95]	32
Figure 18. Diffraction efficiencies of the zero order $[DE_0(0)]$ and first order $[DE_0(\pm 1)]$ using the scalar diffraction theory including the absorption loss in the metal layers. [95]	33
Figure 19. Distribution of a beam passed through a plano-convex lens	34
Figure 20. The coordinate system of the device	36
Figure 21. Intensity variation on the plane with photo detector. Photo detector plane is $1000 \mu\text{m}$ behind from diffraction grating. Target moves $\pm 0.23 \mu\text{m}$ at the focal point	42
Figure 22. Photo detector signal variation. Lens and diffraction grating are on different sides. Photo detectors located at $216 \mu\text{m}$ from principal axis, $1000 \mu\text{m}$ behind the diffraction gratings. Target moves $\pm 1 \mu\text{m}$ at the focal point	43
Figure 23. Phase at lens back plane	43
Figure 24. Intensity distribution on the target in analysis	45
Figure 25. Schematic of the experiment set-up	45
Figure 26. Measured Intensity distribution on the target in the experiment	46
Figure 27. Schematic of the experiment set-up	47
Figure 28. Measured diffraction intensity at the detector in normalized distance	47
Figure 29. Focal length of the designed plano-convex lens at each axial lay displacement	49
Figure 30. Focal length of the designed convex-plano lens at each axial lay displacement	50

Figure 31. Schematic of an electrostatic actuated beam	52
Figure 32. Force diagram for a small element in the beam	54
Figure 33. Beam with electrostatic forces and residual tension forces.....	55
Figure 34. Force diagram for the beam in Figure 33	55
Figure 35. Deflection of the beam in different voltages (a) without residual tension (b) with residual tension	56
Figure 36. Schematic of a grating and an electrode for the case analysis	57
Figure 37. Grating deformation for the different electrode length with no offset	58
Figure 38. Deformation for the different electrode length with no offset (a) numerical analysis result (b) FEM analysis result.....	59
Figure 39. Grating deformation for the same electrode length of 50 μm with different L_0	59
Figure 40. Grating deformation with and without increase of thickness at center	60
Figure 41. FEM analysis results showing an increased thickness at the beam center	61
Figure 42. Further improvement by reducing membrane thickness from 1 μm to 0.8 μm	61
Figure 43. A quarter model of the grating membrane	62
Figure 44. Vertical deformation contour for 15V voltage in FEM analysis (a) oblique view (b) top view (c) side view	64
Figure 45. Modified shape of the grating membrane.....	65
Figure 46. Vertical deformation contour for 15V voltage in FEM analysis (a) oblique view (b) top view (c) side view	67
Figure 47. Deformation of the grating during actuation	67
Figure 48. Deformation at the illumination zone during actuation.....	68
Figure 49. DC bias vs. gap.....	68

Figure 50. Modal analysis result showing the first bending mode of 140 kHz	69
Figure 51. Designed micromachined scanning interferometer (μ SI).....	70
Figure 52. A microlens and a deformable grating	72
Figure 53. PR thickness vs. PR spinning speed of the fabricated lenses	74
Figure 54. Focal length vs. PR spinning speed of the fabricated lenses.....	75
Figure 55. Profile of the fabricated lens that is spun at 2500 rpm	75
Figure 56. Focal length vs. PR spinning speed of the fabricated lenses on the aperture...	76
Figure 57. SEM image of the fabricated micro lenses.....	77
Figure 58. Surface profile of the fabricated microlens	78
Figure 59. Histogram of deviation of the measured microlens surface profile from a fitted sphere of 612 μ m diameter	78
Figure 60. Set-up to measure focusing performance of the microlens	79
Figure 61. Measured images that come from the microlens and aperture	80
Figure 62. An image at focal plane.....	81
Figure 63. Measured intensity profile at focus	82
Figure 64. Deposited aluminum electrode and PECVD oxide on the electrode.....	83
Figure 65. Patterned PR sacrificial layer	84
Figure 66. Sputtered aluminum layer on the sacrificial PR.....	85
Figure 67. Defined center region by RIE process.....	86
Figure 68. SEM picture showing etched shape by standard aluminum RIE process	86
Figure 69. SEM pictures of grating PR pattern.....	89
Figure 70. Etched grating.....	90
Figure 71. Released grating pattern	91

Figure 72. Measure profile of the released grating membrane	91
Figure 73. Deformable grating fabrication processes	93
Figure 74. Grating surface profile at 0V and 27V DC bias by optical profilometer	94
Figure 75. Gap measurement at different DC bias levels	94
Figure 76. Set-up for deformable grating test	96
Figure 77. Measured PD output as a function of DC bias	96
Figure 78. Measured PD output as a function of gap	96
Figure 79. AC ($\pm 0.5V$) response at certain DC bias at Figure 77	97
Figure 80. Measured frequency response of the deformable grating	97
Figure 81. The deformable grating and lens in integration	98
Figure 82. A fabricated array of 3x3 detectors	100
Figure 83. Grating and PD location	100
Figure 84. Diced 3x3 detectors for ready to mount on PCB	101
Figure 85. Intensity at photo diode plane showing 3 rd diffraction order	102
Figure 86. Schematics of the package	103
Figure 87. A wire bonded photo diode chip and a spacer	104
Figure 88. An assembled deformable grating chip on a detector chip	104
Figure 89. An assembled microlens chip on the top of the package	105
Figure 90. Micromachined microphone (a) SEM picture (b) electrostatic actuation by bottom electrodes	107
Figure 91. Experimental set-up	107
Figure 92. Detector signal for 5, 10, 15 burst	108
Figure 93. Experiment set-up	109

Figure 94. Detector signal showing an interference curve	110
Figure 95. Magnification of data presented in Figure 94.....	110
Figure 96. Schematics of μ SI scanning system with lock-in amp	112
Figure 97. Physical experiment set-up.....	112
Figure 98. Scanning results using phase sensitive detector	113
Figure 99. A trace in the cMUT that is used in the lateral scanning.....	114
Figure 100. Fine scan on the trace	114
Figure 101. Results on the cross-section of A in Figure 100.....	115
Figure 102. Schematics of experiment set-up.....	116
Figure 103. Optical microscopy image of a cMUT showing membrane diameter and trace width	117
Figure 104. Static profile of a cMUT using a Veeco white light interferometer.....	118
Figure 105. Average DC image of a cMUT	119
Figure 106. Values of the cross section A-A in Figure 105.....	119
Figure 107. Picture of the experiment set-up.....	121
Figure 108. Scanning set-up for integrated μ SI.....	121
Figure 109. Diffracted beam pattern after μ SI.....	122
Figure 110. Microscope picture of one of the scanned cMUT	122
Figure 111. The cMUT surface profile at 30V	123
Figure 112. Average DC image of a cMUT	123
Figure 113. Cross-section (a) A-A (b)B-B (c)C-C in Figure 112.....	124
Figure 114. (a) First vibration mode shape (b) Second vibration mode shape	126

Figure 115. (a) Measured amplitude of the first vibration mode (b) Numerical model of the first vibration mode (c)Cross-section A-A (d)Cross-section B-B	127
Figure 116. (a) Measured amplitude of the second vibration mode (b) Numerical model of the second vibration mode (c)Cross-section A-A (d)Cross-section B-B .	128
Figure 117. Measured amplitude of the first vibration mode	130
Figure 118. (a)Cross section A-A in Figure 117 (b)Curve fitting to A)	131
Figure 119. Electrical equivalent noise circuit	135
Figure 120. Noise density as a function of DC photocurrent measured at 20kHz [106].	135
Figure 121. cMUT integrated with PD[106].....	136
Figure 122. Measured minimum detectable displacement in the integrated acoustic sensor obtained at 20kHz and 100kHz. Also shown is the shot-noise limited detectable displacement for comparison [106]	136
Figure 123. Typical optical intensity curve as a function of path difference	138
Figure 124. Control system block diagram.....	139
Figure 125. Measured optical intensity, first harmonic, and second harmonic curves as a function of path difference.....	140
Figure 126. Power in the second harmonic.....	141
Figure 127. Power spectrum of the photodetector signal	141
Figure 128. (a) A scanned trace without control (b) A scanned trace with control (c) Cross-section A-A in (a) (d) Cross-section A-A in (b).....	142
Figure 129. (a) A scanned cMUT without control (b) A scanned cMUT with control (c) Cross-section A-A in (a) (d) Cross-section A-A in (b).....	143
Figure 130. Control system block diagram.....	143

Figure 131. PD signal showing (a) 10kHz vibration on 40Hz ramp (b)after band pass filtering around 10kHz.....	145
Figure 132. Magnified signals in 0.125-0.15 sec showing magnitude envelop that depends on measurement sensitivity.....	145
Figure 133. Decomposed grating and cMUT signal from PD signal at 900kHz vibration of cMUT	146
Figure 134. Integrated metrology in advanced process control	152
Figure 135. μ SI combined with confocal microscopy	154

NOMENCLATURE

α	: Direction cosines to x
β	: Direction cosines to y
ε_0	: Permissivity of the air
λ	: Wavelength of light source
Λ	: Period of a grating
ρ	: Radius of curvature of a beam
ϕ	: Phase of a plane wave
d	: Distance from a grating to an objective
d_s	: Sag of a lens
D_{G-PD}	: Distance from a grating to a photo diode
D_{PD}	: Distance from a photo diode hole center to a photo diode
DE_0	: Diffraction efficiency
E	: Young's modulus
f, f_0	: Focal length of a lens
F_e	: Electrostatic force
\mathcal{F}	: Fourier transform operator
\mathcal{F}^{-1}	: Inverse Fourier transform operator
f_i	: Uniformly distributed force per unit length
h	: Offset from a principal axis
h_g	: Gap between an electrode and grating

I	: Moment of inertia
I_0	: Intensity of the zero diffraction order
I_1	: Intensity of the first diffraction order
k	: Wave number
L_e	: Half length of an electrode
L_m	: Half length of a grating membrane
M	: Number of harmonics
M_b	: Bending moment
n	: Refraction index of a lens
n_s	: Refraction index of a substrate
R	: Outer radius of a lens
T	: Tensile force by residual stress in a beam
u	: Field
U	: Angular spectrum of u
U_0	: Angular spectrum of $u(x, y, 0)$
u_r	: Field in reflection
U_r	: Angular spectrum of u_r
V	: Applied voltage
V_s	: Surface force
W	: Width of an electrode

SUMMARY

In this thesis, new metrology hardware is designed, fabricated, and tested to provide improvements over current MEMS metrology. The metrology system is a micromachined scanning interferometer (μ SI) having a sub-nm resolution in a compact design. The proposed microinterferometer forms a phase sensitive diffraction grating with interferometric sensitivity, while adding the capability of better lateral resolution by focusing the laser to a smaller spot size. A detailed diffraction model of the microinterferometer was developed to simulate the device performance and to suggest the location of photo detectors for integrated optoelectronics.

A particular device is fabricated on a fused silica substrate using aluminum to form the deformable diffraction grating fingers and AZ P4620 photo resist (PR) for the microlens. The details of the fabrication processes are presented. The structure also enables optoelectronics to be integrated so that the interferometer with photo detectors can fit in an area that is 1mm x 1mm.

The scanning results using a fixed grating μ SI demonstrated that it could measure vibration profile as well as static vertical (less than a half wave length) and lateral dimension of MEMS. The μ SI, which is integrated with photo diodes, demonstrated its operation by scanning a cMUT. The PID control has been tested and resulted in improvement in scanned images. The integrated μ SI demonstrated that the deformable grating could be used to tune the measurement keep the interferometer in quadrature for highest sensitivity.

CHAPTER 1

INTRODUCTION

1.1 MOTIVATION

Aspirations for miniaturization of optical and mechanical devices have spurred many research activities in microoptoelectromechanical systems (MOEMS) and microelectromechanical systems (MEMS) for last three decades. A significant part of MEMS research so far has concentrated on developing process technology and optimizing individual device performance. However, as the technology and market potential are being realized, a sophisticated MEMS quality control scheme needs to be developed. This requires metrology throughout the design, fabrication, wafer level test, post-package test and reliability testing processes [1]. Most of the MEMS processes have been developed from lithography-based microfabrication and micromachining techniques. These kinds of techniques are borrowed from the microelectronics industry and offer the potential of great cost reduction in batch fabrication processes for high volume manufacturing [2]. Though the MEMS processes can be cost effective, there are still many barriers to MEMS commercialization. One of them is the lack of concern for product testing in mass production level [3]. Two statistics in the MEMS industry and semiconductor industry support this claim. In the MEMS industry, about 25% of the production cost is spent on quality inspection for a product yield of 40-70%. These

numbers are not good in comparison to the semiconductor industry, where 10% of the cost of products is spent on quality inspection for a yield of 90% [4]. The uniqueness of many MEMS devices from semiconductor devices lies in their mechanical dynamics. For example, both static and dynamic characteristics of micro-transducers and grating-light-valves (GLV) need to be measured to validate their design and fabrication processes. Nagel and Zaghloul [5] pointed out that the testing of MEMS devices is more complex than the testing of ICs because of the integrated electronics and mechanical nature of MEMS. For ICs, testing involves only electric inputs and outputs. For MEMS, inputs can be vibrations or other particular conditions of pressure, humidity and chemical vapor composition. Also, for most MEMS, critical device dimensions ($10\text{-}1000\ \mu\text{m} \pm 10\%$) fall between silicon IC ($<10\ \mu\text{m} \pm 10\ \text{\AA}$) and conventional machining ($>1000\ \mu\text{m} \pm 10\ \mu\text{m}$). Therefore, MEMS metrology demands methods different from those used in either of these cases [6]. A MEMS metrology system must have sub-micron precision, a sub-millisecond sensing, a reliable and robust performance in harsh environment, and miniaturized hardware that can be easily integrated in existing systems [7].

1.2 PROBLEM STATEMENT

Table 1 shows a brief technology comparison of several methods used for making dynamic MEMS measurements. Although some commercial metrology tools are available for this purpose, their bulky size, high cost and slow speed are major drawbacks. From a mass manufacturing point of view, only traditional stand-alone platforms (off-

line) are currently available, which require the wafer to be taken out of the production line for inspection.

Table 1. Technology comparison for MEMS measurement techniques [8]

Features	MEMS Motion Analyzer	Vibrometer	Profilometer
Z measurement Technique	Strobe laser interferometer	Laser Doppler vibrometer	White light interferometer
XY measurement Technique	Strobe machine vision	N/A	N/A
Profilometry resolution	5 nm	N/A	< 1 nm
Dynamic motion measurement capability	Yes, in X,Y, and Z	Yes, in Z only	No
Maximum Z velocity	1 m/s	10 m/s	No
Maximum XY velocity	50 m/s	N/A	N/A

There are three questions that need to be answered in order to improve existing MEMS metrology tools. The first question is that what kind of sensor structure is appropriate for in-line inspection. As described in the literature [9] for semiconductor industry, in-line systems are not a just replacements of off-line tools. They reduce wafer handling cost by detecting faulted wafer in the middle of process line and reduce cycle times because everything is done on the fabrication platform, without removing the wafer. Moreover, with shrinking geometries and more chips on a larger wafer, metrology refines the process to achieve the best possible yield. Of course, this conclusion is still valid for the mass production of MEMS devices. In-line inspection capability is more important in the production of MEMS devices than in the production of semiconductors since a wafer-to-wafer control is required in MEMS production to increase the yield. The integrated

metrology is immature and the technology is still being qualified for semiconductors. Many sensors lack the performance capability of today's leading stand-alone tools [9].

The second question concerns how to accurately measure dynamic characteristics as well as static characteristics of MEMS devices. Is the system fast enough to measure high speed of vibrating microbeam and how well does it shows deformed or displaced structures? These required capabilities can be partially achieved by using a strobe white light interferometer. It can measure microstructures vibrating at less than 1 MHz. Many MEMS devices are operate at less than 1 MHz, but some devices such as RF switches operate at higher speed. Accurate deformation information is needed to inspect a required deformed shape of devices. For example, GLV needs a flat surface to maintain high diffraction efficiency during operation.

The third question is how to improve the measurement speed of MEMS. This is important factor for an in-line metrology system to compete with dominant stand-alone solutions in current market. Current metrology tools in the semiconductor industry rely on X-Y accuracy and repeatability of the measurement. This requires a stable, mechanically isolated environment which is easily implemented in a stand-alone fashion. But, the current interferometers measure a small fixed area and can't be expanded to larger areas.

1.3 THESIS OUTLINE

In this thesis, new metrology hardware is designed, fabricated, and tested to provide improvements over current MEMS metrology. The metrology system is a micromachined scanning interferometer (μ SI) having a sub-nm resolution in a compact design. The proposed microinterferometer measures distance using a reflective diffraction grating on a transparent substrate and a microlens fabricated using a photoresist reflow technique on the other side. This structure forms a phase sensitive diffraction grating with interferometric sensitivity, while adding the capability of better lateral resolution by focusing the laser to a smaller spot size. Figure 1 shows the schematic of a μ SI with a photo detector.

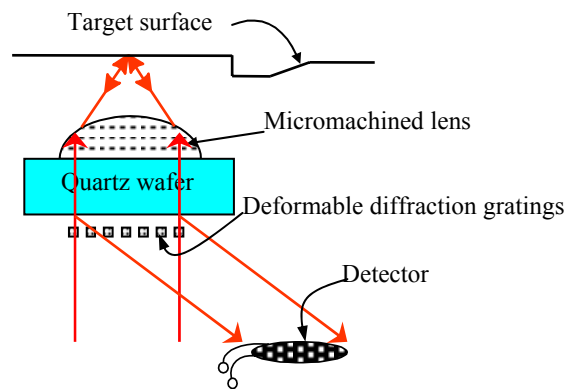


Figure 1. A schematic of a μ SI with a photo detector

Depending on the distance between a diffraction grating and a target surface, the diffraction pattern at the detector plane is changed. By monitoring the intensity of a

certain diffraction order with the detector, a profile change on the target surface can be mapped. A detailed diffraction model of the microinterferometer was developed to simulate the device performance and to suggest the location of photo detectors for integrated optoelectronics. To optimize interferometric sensitivity at a scanning point, a deformable diffraction grating is introduced in CHAPTER 3.

A particular device is fabricated on a fused silica substrate using aluminum to form the deformable diffraction grating fingers and AZ P4620 photo resist (PR) for the microlens. The details of the fabrication processes are presented in CHAPTER 4. The structure also enables optoelectronics to be integrated so that the interferometer with photo detectors can fit in an area that is 1mm x 1mm. The packaging procedure is also presented in the same chapter.

The feasibility of μ SI was demonstrated for measurement of moving microstructures [10]. The μ SI has shown its capability to measure vibration profiles up to 1.25 MHz of 190 μ m diameter capacitive Micromachined Ultrasonic Transducer (cMUT). Detail experimental results are presented in CHAPTER 5. CHAPTER 6 summarizes the research results and concludes this thesis.

In summary, this thesis presents a new metrology tool, μ SI for measuring dynamic and static characteristics of MEMS devices. The design concept of the μ SI is an in-line MEMS inspection device that can answer three questions in the problem statement. Theoretical analysis and validation test results are presented to show the feasibility of the μ SI. A MEMS fabrication process was developed and is presented. Finally, fabricated sensors were tested with cMUT.

CHAPTER 2

LITERATURE REVIEW

2.1 3-D METROLOGY

Research on accurate measurement of the 3-D shapes has been increasing in industry, because the benefit of qualification allows manufacturing companies to make more accurate products. In this section, some 3-D metrology techniques are summarized in several categories: contact and noncontact for the mesoscale ($>100\ \mu\text{m}$), microscale (100 nm to 100 μm), and nanoscale ($<100\ \text{nm}$) static surface.

2.1.1 CONTACT METHODS

Conventional contact measurement has been a reliable method for hard surfaces. Coordinate measurement machines (CMM) are in use by a wide range of industries covering a broad array of applications [11]. There has been research to develop a high accuracy CMM or nano-CMM. Peggs *et al.* [12]-[13] designed and built a high-accuracy CMM to a target uncertainty of 50 nm within a 50 mm x 50 mm x 50 mm working

volume. The most difficult issue was contact probes. They use a 0.3 mm diameter ball. The probe has a working force of 0.1 mN and a resolution of 3 nm. Takaya *et al.* [14]-[15] developed a laser trapping probe for the nano-CMM. It can reach a resolution of 10 nm and has a measuring force of 0.01mN. This contact pressure force makes it possible to achieve nanometer sensitivity, similar to atomic force microscopy (AFM). Stylus methods have been used to monitor chemical mechanical planarization (CMP) performance in electronics fabrication [16] and measurement of Young's modulus on microfabricated structures [17]. A silicon micro-probe with a sharp tip was used to measure the inner profile of high aspect-ratio microstructures [18]. AFM [19]-[21] has been popular for measuring microstructure dimensions. They can measure deflections that are much less than 1 Å [20].

2.1.2 NONCONTACT METHODS

Noncontact measurement is of significant interest because it avoids deformation of the products and mechanical errors in the contact measurement. The basic principle of an active noncontact range finding system is to project a wave-radio, ultrasonic, or optical source onto an object and process the reflected signal to determine its range. If a high-resolution rangefinder is needed, an optical source must be chosen because it can be focused adequately. Historically, laser distance measurement research papers are well represented in literature [22]. Recent optical range and shape measurement research has been focused on triangulation methods, time of flight methods, conventional confocal

methods, and interferometry [23]. Among them, the triangulation methods and time of flight methods are critically reviewed and their respective fundamental limitations are discussed in the literature [24].

Triangulation methods and time of flight methods cannot measure on the scale of sub μm to hundreds of μm efficiently. Triangulation methods require interpolation to determine the third dimension as well as a very good and expensive projection system to achieve high-resolution images. There have been efforts to improve this technique for high precision distance measurement. Pierce *et al.* [25] reached an accuracy of 3 μm over a depth of field of 2 mm at a distance of 100 mm from a target. Oka *et al.* [26] fabricated an optical triangulation distance sensor by LIGA technology. It measured around 6mm distance with 2% error. The pulse time of the flight method requires a very small time interval in measurement to achieve high accuracy. For example, to obtain 1mm accuracy, the accuracy of the time interval in measurement is 6.7 ps [24].

Engelhardt and Häusler [27] presented a simple focus sensing technique for diffusely reflecting objects but the depth resolution was not very high. Day *et al.* [28] proposed a focused laser optical feedback image technique. Though these kinds of traditional range findings methods which use a focus analysis are effective, large lenses are required to reduce the depth of the field for high accuracy.

Confocal scanning optical microscopes (CSOM) were used early to measure the topography of tissues and 2-D profiles [29]. In the early 1980s, this technique was introduced for 3-D measurement [30]. Udupa *et al.* [31]-[32] applied CSOM to micro and macro surface irregularity and concluded that it was a useful tool for this purpose. Phyyawattanametha *et al.* [33] reported the first MEMS non-interferometric differential

confocal microscope and they expected that it could be used for endoscopic imaging applications. For a small scale depth or shape, μm or even nm scale measurements can be achieved if a confocal microscope or other 3-D microscope is used, but it requires a very short standoff distance from the object and makes scanning difficult.

Interferometry is popular for a surface profiling. Wyant and Prettyjohns [34] presented surface metrology system having a Mirau interferometer mounted on the piezoelectric transducer (PZT). This technique demonstrated 1 nm accuracy of a known reference standard step height. With the same instrument but two wavelength sources, Creath [35] measured a large step height that a single wavelength could not measure. Himilton and Sheppard [36] presented a confocal interference microscope which could separate a normal confocal image and an interference image. Elements of coherence scanning microscopy were first published by Davison *et al* [37]-[38]. Lee and Strand [39] demonstrated that coherence scanning microscopy could be used on large steps, multiple layer structures, and rough surfaces. Dresel *et al.* [40] demonstrated coherence radar, a combination of time of flight and interferometer on rough surface. But they could not eliminate speckled images. Yi *et al.* [41] achieved a standard deviation of the measurement error of 2.7nm in monitoring a 1.5 μm moving distance by detecting a fringe peak which is linearly proportional to the displacement of object. Hemmert *et al.* [42] applied interference microscopy to detect in-plane and out-of-plane motion of MEMS accelerometers. Rugar *et al.* [43] applied fiber-optic interferometers for AFMs. A grating interferometer which does not need a beam splitter was built in AFM tip array [19], encoder read-out [44], and cMUT [45], [46]. It was also applied to sense the position of a specular object in a simple set-up [47], [48]. Drawbacks of an interferometer

are that it cannot read discontinuities of the object geometry and only works in relative coordinate space. But these have been overcome by combining an interferometer with other technique such as confocal microscopy without reducing its sensitivity.

2.2 MEMS METROLOGY

There have been several approaches to MEMS metrology. Some techniques for MEMS have been introduced in the prior section, but most of them are for static micro structures. In this section, techniques for dynamic MEMS structures are summarized.

To detect motion of MEMS in all three directions, high resolution is required in-plane and out-of-plane. Davis and Freeman [49] used a light microscope to measure in-plane motion in nanometer accuracy. By adding an interferometer to this system, Hemmert et al. [42] could also reach less than 1 nm resolution for out-of-plane and 2.5 nm resolution for in-plane rigid body motion of a micromachined accelerometer. He drove an LED with a 1/8 duty cycle pulse-train synchronized with one of eight equally spaced phases of the excitation signal to stroboscopically freeze the MEMS motion. He collected a sequence of interferograms for different axial locations of the reference to determine the best fitting information on the pixel (i.e., local point of MEMS). The stroboscopic interferometer has been used to make a measurement for single frequency harmonic analysis of MEMS device vibration [50]-[52]. Hart *et al.* [50] demonstrated static and dynamic characterization of a micromirror. They got out-of-plane surface profiles of the micromirror when it was driven at 2.2 kHz. Their repeatabilities were

better than 1.5 nm. Rembe and Muller [51] expanded their system to in-plane motion. By saving strobed cinematographic images, they computed in-plane motion of MEMS with resolutions within 5 nm. Their out-of-plane resolution was 0.7 nm. Novak *et al.* [52] measured an in-plane resonator which was actuated at 4 kHz. The microcavity interferometer with a reference in the wafer was proposed to avoid misalignment between reference and device [53]. Lawton *et al.* [54] used a scanning Laser-Doppler Vibrometer to measure the velocity of a moving surface by detecting the Doppler frequency shift of a reflected laser beam. The displacement at a local spot on the surface is computed by integrating the velocity data. For high frequency responses and high spatial resolution, a spatial phase sensitive optical scanning interferometer was introduced [55]-[57]. It demonstrated surface profiles of a thin-film resonator operating near 2 GHz and an out of plane resolution of $\sim 0.003 \text{ \AA}$ [57]. Stroboscopic interferometer system [58] and scanning Laser-Doppler Vibrometers [59] are commercially available.

In summarizing efforts over a few years for MEMS metrology, the interferometer has been dominant due to its capability for high resolution and fast speed for the motion of objects. These techniques still need large set-ups and offer only off-line solutions.

2.3 MICROLENS AND GRATING

A microlens and diffraction grating are the main components of the device developed in this work. As the demand for arrays of lenses with a diameter of less than 1mm has grown over the past 20 years, a wide range of techniques from the

microlithography industry have been used to make these small lenses [60]. Borrelli [61] classified the fabrication methods for micromolding/embossing [62] and photoresist reflow technique [63]-[66], microjet [67], and photosensitive glass technique. The refractive microlens was fabricated on an out-of-plane surface [68]. The diffractive microlens was fabricated on the substrate [69]-[72]. The profiles of fabricated lenses on the substrate can be copied to the substrate using a dry etching process [73]-[74]. AZ P4620 photoresist is used for this research as it is a good material for the lens fabrication using a reflow technique because of its high resistance to spreading, and chemical thermal stability [68]. Details of the microlens fabrication are provided in CHAPTER 4.

The photoresist surface-relief diffraction grating [75]-[78] and metal deposited diffraction grating [46] can also be fabricated on a substrate. The grating can be fabricated in fused silica by reactive ion etching (RIE) of patterning photoresist [79].

2.4 VERTICAL TRAVEL ACTUATOR

Mechanical actuators are used to convert electrical (or other) energy into mechanical energy such as displacement. The fundamental actuation principle in electrostatic actuators is the attraction of two oppositely charged plates. These electrostatic actuators have been used extensively in MEMS devices, since it is simple to fabricate closely spaced gaps between conductive plates and they require very low power [80]. Examples of this type of actuation are Polychromator [81], [82], GLV [83]-[86], electrostatic motor [87], electrostatic gripper using comb drive [88], and RF switch [89].

Depending on the designed structure, the displacement could be vertical which is perpendicular to the substrate, lateral which is parallel to the substrate, or rotational about an axis. The grating in the application discussed in this dissertation needs vertical motion by changing power between the conductors. The vertical travel actuator in the Polychromator designed by Hocker *et al.* [81] has width of 10 μm , length of 1 cm, and travel length of 2 μm to detect 3-5 μm wavelengths. The one designed by Deutsch [90] has width of 20 μm , length of 1.2 cm, and travel length of 4-6 μm to detect 8-12 μm wavelengths. It requires a flat large travel length; thus, they designed a two-beam structure in which the lower beam underwent bending while the top beam deflected vertically without flexion. The GLV designed by Bloom [83] has a length of 20 μm , pitch of 5 μm , and pull-down distance of 1300 \AA or approximately one-quarter wavelength of green light. The one beam structure of ribbons in GLV is pulled down by a bottom electrode and the switching speed is 20 nanoseconds because of its small size and mass. Mechanical analysis of GLV is well established in the literature [91].

CHAPTER 3

DESIGN AND ANALYSIS

3.1 DESIGN STUDY FOR GRATING MICROINTERFEROMETER

The interferometer is a suitable tool for MEMS in terms of speed and resolution as discussed in literature review. Yaralioglu *et al.* [92] demonstrated its capability in their noise analysis for a grating interferometer that is fabricated in the AFM to monitor a displacement change of the AFM tip. In their calculation, minimum detectable distance (MDD) is 0.0078 \AA in 1 kHz bandwidth. Graebner *et al.* [57] also demonstrated that the scanning interferometer could measure surface profiles of a thin-film resonator operating near 2 GHz and out of plane resolution of $\sim 0.003 \text{ \AA}$ by a scanning interferometer [57]. In this chapter, a design study for a new scanning interferometer is presented. To apply existing grating interferometer concept to MEMS metrology, design steps and operating principles of the new scanning interferometer are discussed. The operating principles are validated by simulations and experiments. The main components of the system are microlenses and deformable gratings. Designs of these are presented at each section. Finally, μ SI is presented with electronics integration.

3.1.1 MICHELSON INTERFEROMETER

Michelson interferometer which is shown in Figure 2 was found in 1887 and resulted in a Nobel Prize for Michelson in Physics in 1907. By using the interference due to a path difference between a reference mirror and a target, displacement of the target can be measured. Figure 3 shows a detector signal when the target moves at a constant speed. The period of the signal is a half of the wavelength ($\lambda/2$) of the monochromatic light source. By counting the number of period, the displacement of the target is measured. Even the speed of the target is measured by counting the number of periods during certain time period. Thus, the resolution of the measurement is $\lambda/2$ in this case. If a particular interference curve is used for the measurement, the resolution can be increased. Thus, commercially available interferometers provide $\lambda/1024$ resolution at speed of 10 MHz [93]. This interferometer is bulky in size and, therefore it is not feasible for a parallel operation to measure multiple targets.

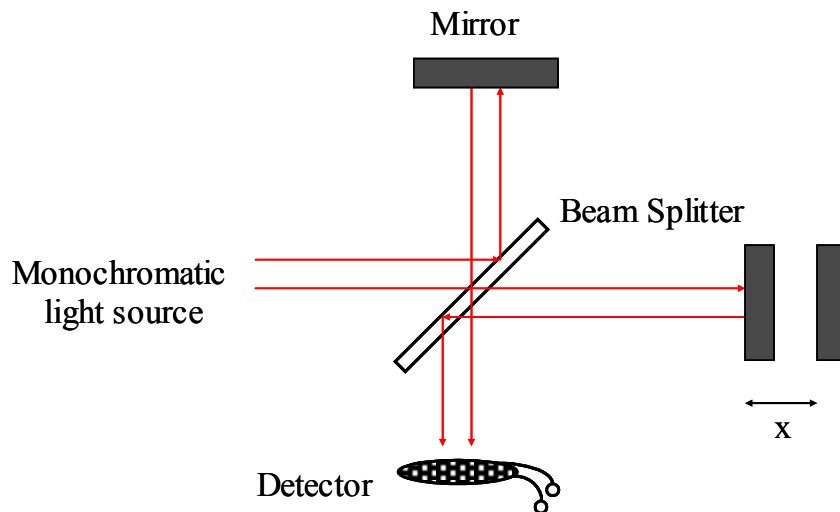


Figure 2. Schematic of Michelson interferometer

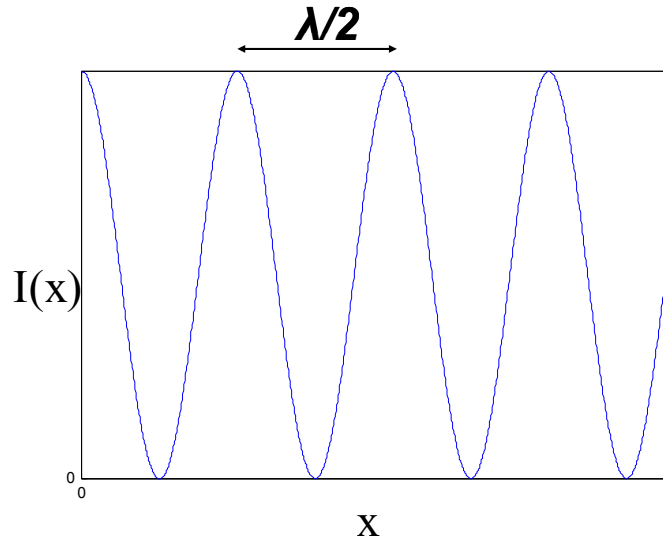


Figure 3. Detector signal when the target moves at constant speed

3.1.2 DIFFRACTION BASED OPTICAL DISPLACEMENT DETECTION

The main feature of the grating interferometer is a phase sensitive optical diffraction grating, in which the diffraction pattern is determined by the distance between a stationary (reference) reflective grating and the reflecting surface. It is assumed that the reference diffraction grating is formed on a transparent substrate and illuminated through the transparent substrate by a laser. As seen in Figure 4, the substrate with the reference fingers and the location of the reflecting surface change the diffraction pattern. The incident light is reflected back to the zeroth order when the distance, d , is an integer

multiple of half of wavelength of incident beam, $\lambda/2$, and to the odd diffraction orders when d is an odd multiple of $\lambda/4$.

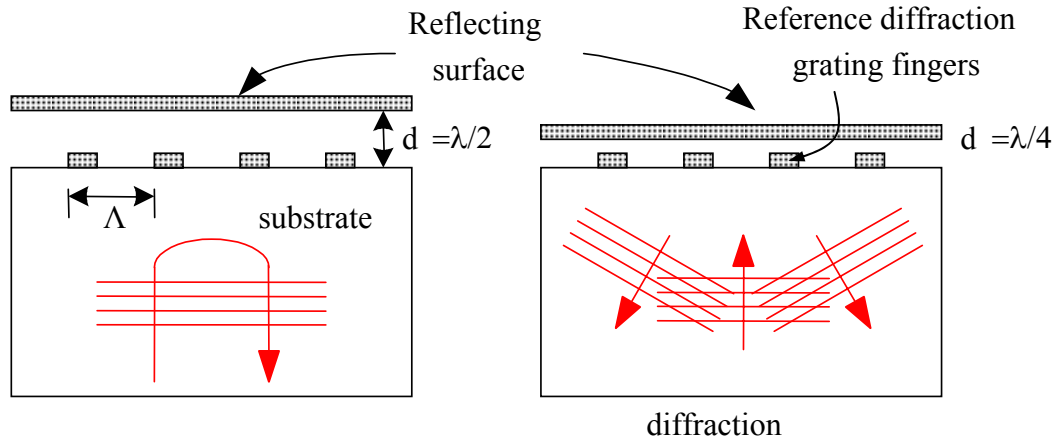


Figure 4. Schematics showing that the diffraction pattern depends on distance to reflecting surface

The diffraction pattern of such a structure can be found by applying diffraction theory to determine the location and the dimension of the photo detectors. Figure 5 shows an example of a diffraction pattern for HeNe laser ($\lambda=632.8\text{nm}$), 10 reference fingers with $\Lambda=2\mu\text{m}$ as an example. The light intensity distribution on an observation plane 1mm away is calculated and plotted for different substrate-reflecting surface distance values. Fourier analysis of the far field diffraction pattern shows that the diffraction order intensities are related to the gap thickness, d , by the relations $I_0 \propto \cos^2\left(\frac{2\pi}{\lambda}d\right)$ and $I_1 \propto \sin^2\left(\frac{2\pi}{\lambda}d\right)$ as depicted in Figure 6. Thus, the grating interferometer works just like a monochromatic Michelson interferometer except diffraction. The good things in the grating interferometer are: it is fabricated in a small

size and optimization of the measurement to increase measurement resolution can be conveniently implemented by controlling the distance the grating to the target. Important points to note in grating interferometer are:

a) Dependence of reflected mode intensity to relative distance between the grating and the reflecting surface is periodic.

b) By monitoring the intensity of any of the reflected orders, interferometric precision can be achieved. Furthermore, Figure 5 also shows that with these parameters, a $100\mu\text{m}$ wide photo detector at either $x=0$ or $x=300\mu\text{m}$ is ideal for optical intensity detection. The bandwidth of the detection scheme depends only on the speed of the photo detectors and the following electronics. These devices can be used up to GHz range with appropriate electronics. Assuming that the coherence length of the laser is long enough and the reflecting surface is parallel to the substrate containing the grating, the intensity dependence shown in Figure 6 can be observed for all distances. This is a problem for absolute distance measurements, since one cannot tell the difference between a distance d and $d + \lambda/2$. To solve this problem, a lens with a known focal distance can be integrated to the diffraction grating.

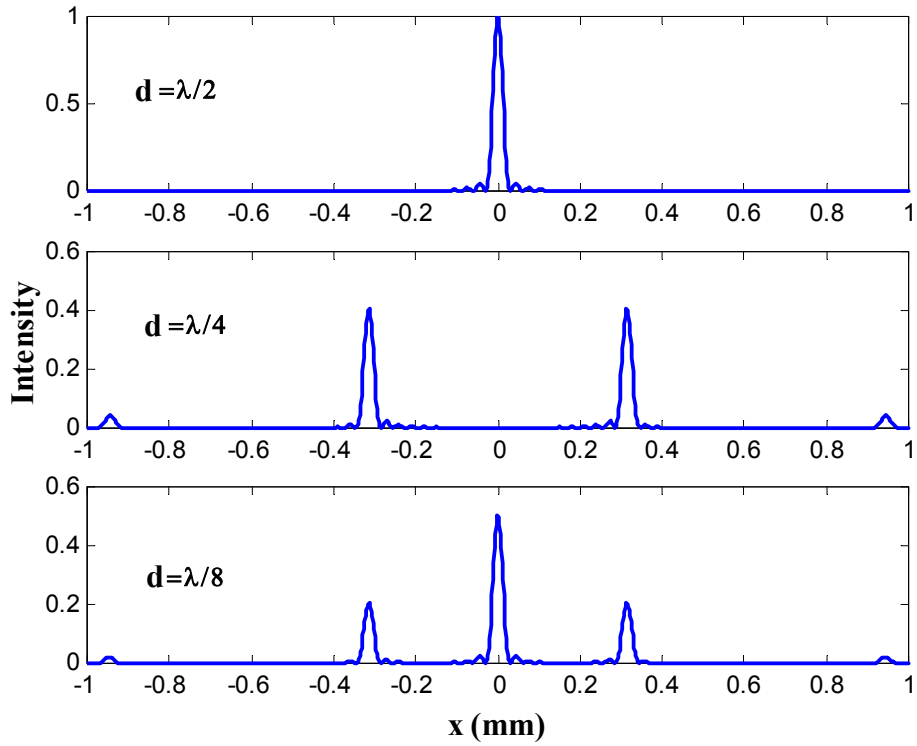


Figure 5. Distribution of the reflected light on an observation plane

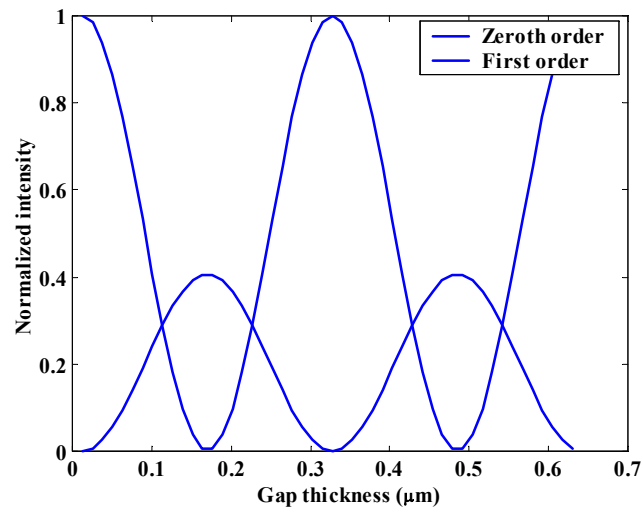


Figure 6. The variation of the intensity of the zeroth and first diffraction order with distance d on an observation plane

3.1.3 FOCUS SENSING

Focus sensing uses limited depth of focus of an optical lens to determine the distance from a known reference to the surface of the object under investigation. Figure 7 shows such a system with a coherent light source and a beam splitter. As seen in Figure 8, the detector signal that is reflected from the target has maximum intensity at the lens focal point. In order to get very good resolution at the focal point, a narrow depth of width is required. The accuracy of the system depends on the depth of focus. Figure 8 shows the dependence of the photo detector output to the difference between the lens-target object distance, x , and the focal distance, f_0 , in wavelength units. In the calculation, the paraxial approximation is assumed and a lens with F-number of ~ 2 is used. Focus sensing systems try to determine the maximum of this intensity curve and assign that distance to the focal distance, f_0 . The accuracy of this system depends on the depth of focus, i.e. 3dB width of the main intensity lobe around the focal distance, which is about 20λ for the given parameters.

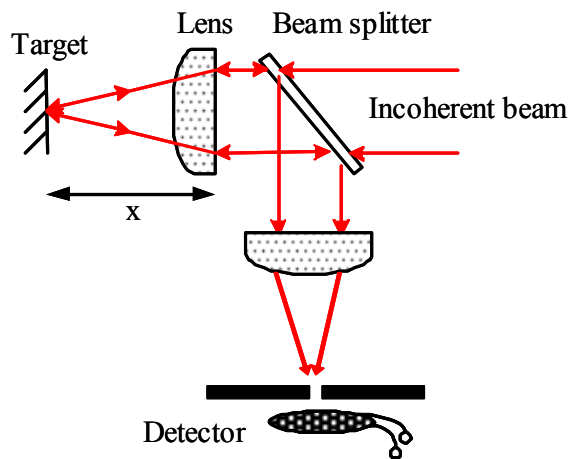


Figure 7. Schematic of a regular focus sensing system

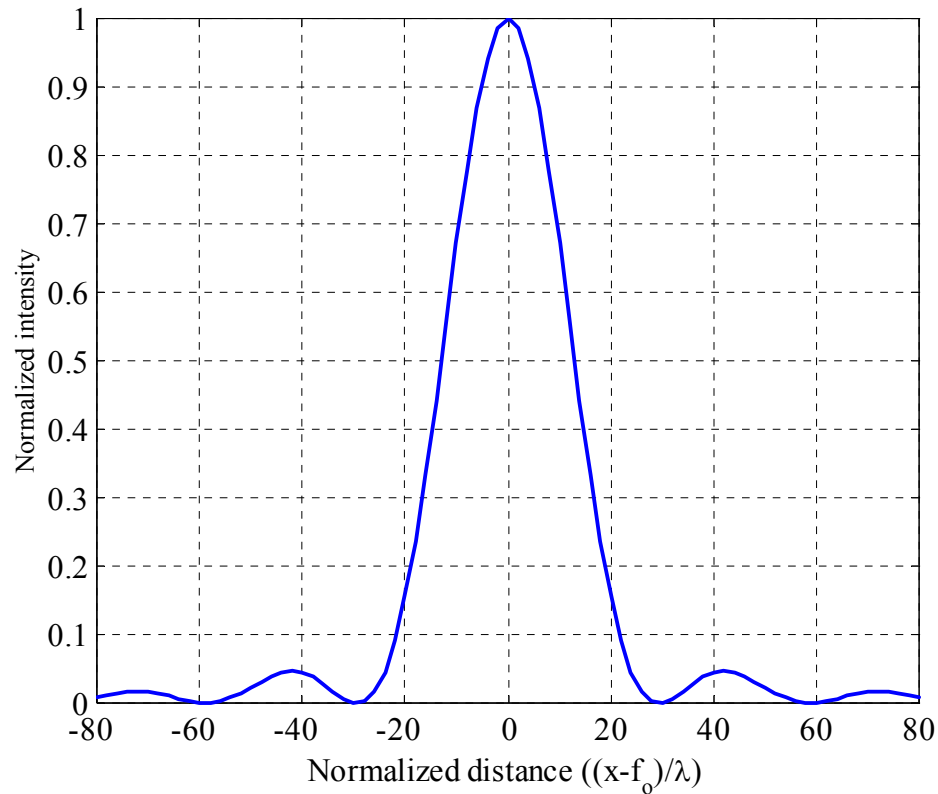


Figure 8. Intensity at the detection as a function of normalized distance to object surface

3.1.4 SENSOR STRUCTURE

To add an absolute distance measurement capability to the grating interferometer, the focus sensing structure needs to be added to the grating interferometer as seen in Figure 9. This structure forms a phase sensitive diffraction grating to have interferometric sensitivity, while adding the capability of absolute distance measurement. In addition, the need for the beam splitter is eliminated and the detector is moved to a plane parallel

to the lens enabling a compact design for miniaturization. The advantages of this structure are clearly seen in Figure 10, which shows the variation of the diffracted intensity as a function of the normalized object-lens separation. In this case, the intensity is an amplitude-modulated version of the curve in Figure 8, where the period of the modulation is $\lambda/2$. Hence, there is more than a 40 times improvement in the width of the main lobe of this intensity curve, because of the interferometric sensitivity. Moreover, the absolute distance can be easily determined by simply counting the intensity cycles around the focal depth of the lens. This yields resolutions around $0.3\mu\text{m}$ for a typical HeNe laser. The resolution of the system can be further enhanced considering the slope of each intensity cycle, yielding distance measurements with sub-nanometer resolution.

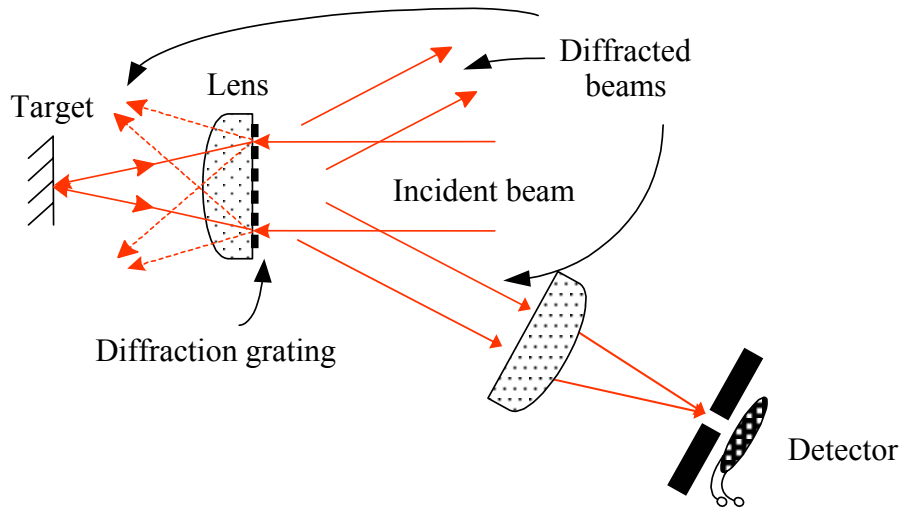


Figure 9. Schematic of a focus sensing system with an integrated diffraction grating for distance measurement

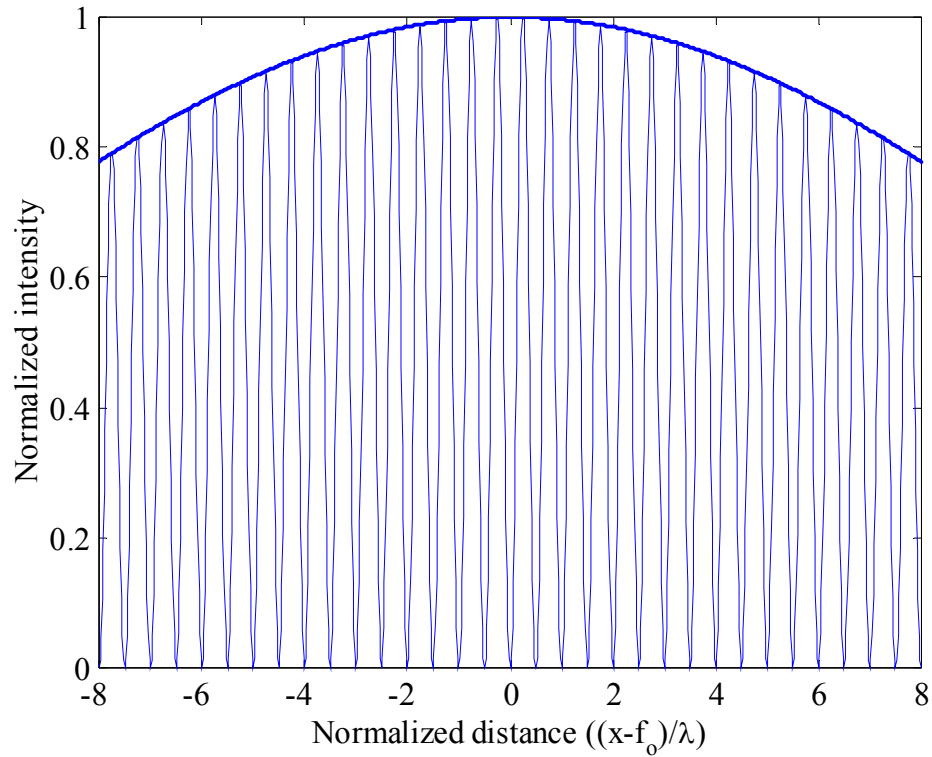


Figure 10. Calculated first diffraction order intensity as a function of distance from the focal point of the lens. The envelope is the intensity of Figure 8.

But this structure is hard to fabricate on wafer levels because the second lens and pinhole have to be fabricated on different wafers and have to be precisely aligned as depicted in Figure 11. Disadvantages of this system are:

- The two lenses must be identical.
- All four levels of the wafers must be aligned well each other at specific distance.

When made in array, each array cannot be calibrated independently in a fixed grating. An advantage is that the deformable diffraction grating which optimizes the sensitivity of the measurement by adjusting the distance from the grating to the target is not essential for the operation.

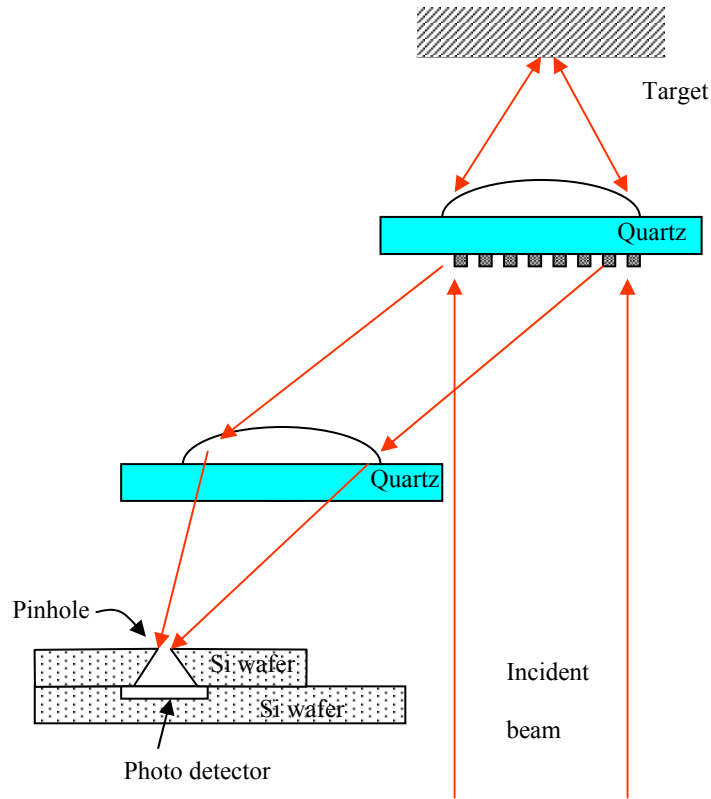


Figure 11 Schematic of a focus sensing system with an integrated diffraction grating at wafer level

Avoiding difficulties of fabrication and maintaining an interferometric sensitivity and depth and lateral resolution of the focus sensing, a deformable diffraction grating can be used with a lens for relative distance measurement. Figure 12 shows this structure. By keeping the distance from diffraction grating to target surface at a constant value of an odd multiple of $\lambda/8$ during scanning to the right, relative changes of the distance from initial scanning point can be measured. The odd multiple of $\lambda/8$ is the most sensitive point as shown in Figure 6. It is not feasible to measure the step more than $\lambda/8$ change. For an inclined surface, it is measurable if the scanning period is small enough to give

less than $\lambda/4$ distance change and the inclined angle is less than $2\text{tan}^{-1}\left(\frac{1}{2 \times \text{F-number}}\right)$. If the diffraction grating deforms $\lambda/4$ or a certain deformation limit, it requires switching back to initial deformation of the grating or another implementation to maintain the sensitivity for the next measurement. By counting the number of switches, the distance more than $\lambda/4$ is measurable. Figure 13 shows a detail schematic of μSI with electronics integration.

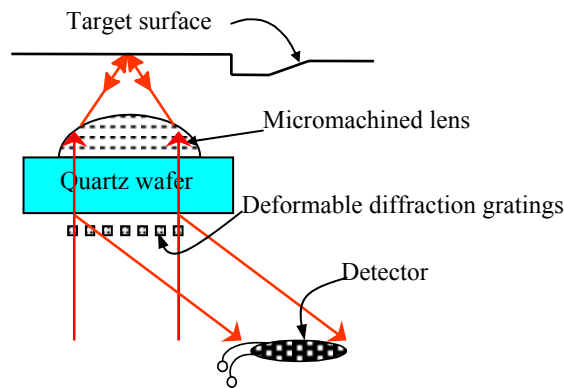


Figure 12. Schematic of a μSI

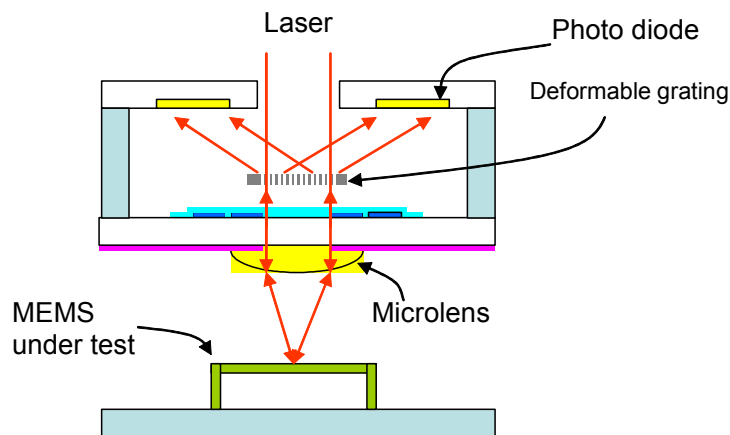


Figure 13. Schematic of a μSI with photo diode integration

3.1.5 SCALAR DIFFRACTION THEORY

To evaluate the optical performance of this device, one-dimensional scalar diffraction theory is used from literature [94]. This theory provides a means by which the spatial Fourier components of the field as plane waves traveling in different directions and the amplitude at any point in the field can be calculated by adding the contributions of all these waves. If the complex field distribution across any plane is Fourier analyzed, the various spatial Fourier components can be identified as plane waves traveling in different directions. The field amplitude at any other point can be calculated by adding the contributions of these plane waves. If a monochromatic source is incident on the (x, y) plane of Figure 14, traveling to the positive z direction, then the complex field across that plane can be represented by $u(x, y, 0)$. At a distance z from x-y plane, the field $u(x, y, z)$ can be written

$$u(x, y, z) = \int_{-\infty}^{\infty} \int_{-\infty}^{\infty} U\left(\frac{\alpha}{\lambda}, \frac{\beta}{\lambda}, z\right) \exp\left[j2\pi\left(\frac{\alpha}{\lambda}x + \frac{\beta}{\lambda}y\right)\right] d\frac{\alpha}{\lambda} d\frac{\beta}{\lambda} \quad (1)$$

where α and β are direction cosines to x and y . The field, u , must satisfy the Helmholtz equation, $\nabla^2 u + k^2 u = 0$ where $k = 2\pi/\lambda$. A solution for this equation can be written in the form

$$U\left(\frac{\alpha}{\lambda}, \frac{\beta}{\lambda}, z\right) = U_0\left(\frac{\alpha}{\lambda}, \frac{\beta}{\lambda}\right) \exp\left(j \frac{2\pi}{\lambda} \sqrt{1 - \alpha^2 - \beta^2} z\right) \quad (2)$$

where $U_0\left(\frac{\alpha}{\lambda}, \frac{\beta}{\lambda}\right)$ is the angular spectrum of $u(x, y, 0)$. This shows that when the direction cosines satisfy $\alpha^2 + \beta^2 < 1$, the effect of propagation to the z is a change in the relative phases of the various components of the angular spectrum. Finally, the field at (x, y, z) can be written in terms of the initial angular spectrum by inverse-transforming Equation (2)

$$u(x, y, z) = \int_{-\infty}^{\infty} \int_{-\infty}^{\infty} U_0\left(\frac{\alpha}{\lambda}, \frac{\beta}{\lambda}\right) \exp\left(j \frac{2\pi}{\lambda} \sqrt{1 - \alpha^2 - \beta^2} z\right) \exp\left[j 2\pi \left(\frac{\alpha}{\lambda} x + \frac{\beta}{\lambda} y\right)\right] d\frac{\alpha}{\lambda} d\frac{\beta}{\lambda} \quad (3)$$

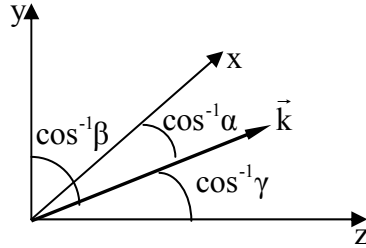


Figure 14. Coordinate system for angular spectrum calculation

3.1.6 COUPLED-WAVE ANALYSIS

Lee *et al.* [95] did a rigorous coupled-wave analysis to generalize a (2×2) matrix method in homogenous layered media for a grating-embedded multilayer structure with $(2M \times 2M)$ dynamic and propagation matrices in both TE and TM polarizations, where M

is the number of harmonics retained in the field expansion. His numerical results using a rigorous coupled-wave analysis for a diffraction-based opto-acoustic sensor shown in Figure 15 that consists of a reflective movable membrane and fixed grating fingers on a transparent quartz substrate are compared with the scalar diffraction method. Following is their numerical results.

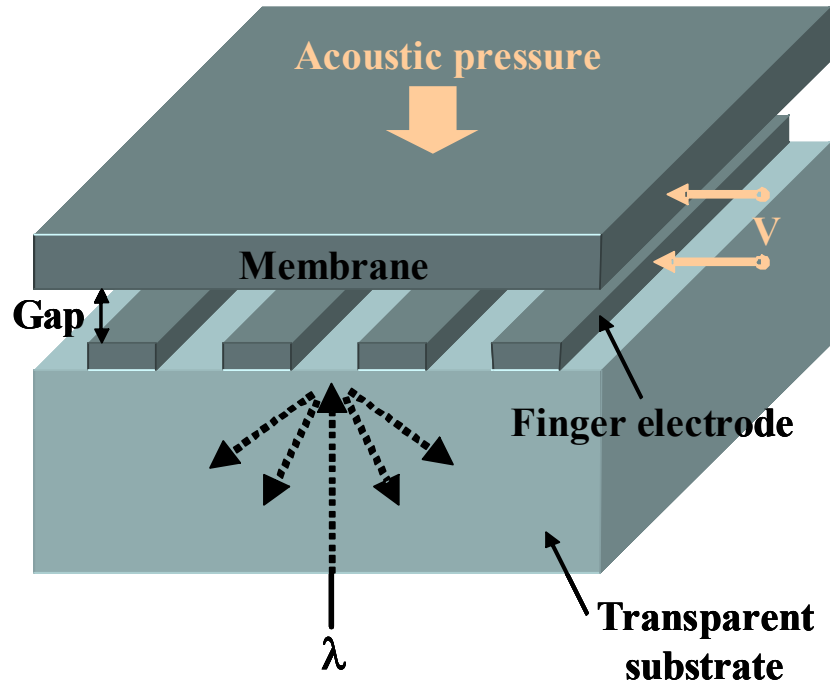


Figure 15. Schematic of a diffraction-based acoustic sensor [95]

A linearly polarized VCSEL light ($\lambda = 0.85 \mu\text{m}$) coupled from the back generates reflected beams of multiple diffraction orders. The intensity variation of the diffracted beams depends on the membrane displacement (i.e., the change in the gap thickness) in response to acoustic pressure or electrostatic actuation by applying a voltage V between the membrane and the finger electrodes. Figure 16 and Figure 17 show the calculated

reflected diffraction efficiencies of the zero and first orders [$DE_0(0)$ and $DE_0(\pm 1)$] as a function of the gap thickness for $\Lambda = 4 \mu\text{m}$ and $\Lambda = 2 \mu\text{m}$, respectively. Here Λ is a period of the grating. The finger width is $\Lambda/2$, and the plane wave is assumed to be normally incident. For comparison, the diffraction efficiencies of the zero and first orders are also calculated from the scalar diffraction theory with the same input parameters as plotted in Figure 18.

Numerical results for $\Lambda = 4 \mu\text{m}$ (Figure 16) show periodic diffraction pattern with $\lambda/2$ periodicity, and the polarization effect is not significant. The diffraction curves are similar to those calculated using the scalar diffraction theory as presented in Figure 18. The results get closer as the grating period is increased [96]. In the case of $\Lambda = 2 \mu\text{m}$ (Figure 17) where the grating size is comparable to the wavelength, anomalous diffraction characteristics, which cannot be predicted from the scalar approach, are observed – extra peaks in the diffraction curves appear so that the periodicity of $\lambda/2$ is broken and the polarization dependency is apparent, especially in the zero-order diffraction. These results show that the scalar method cannot accurately evaluate optical characteristics of diffractive optical devices as the grating size is miniaturized as comparable to or less than the optical wavelength. Thus, a scalar diffraction theory should be used when the grating size is more than the optical wavelength.

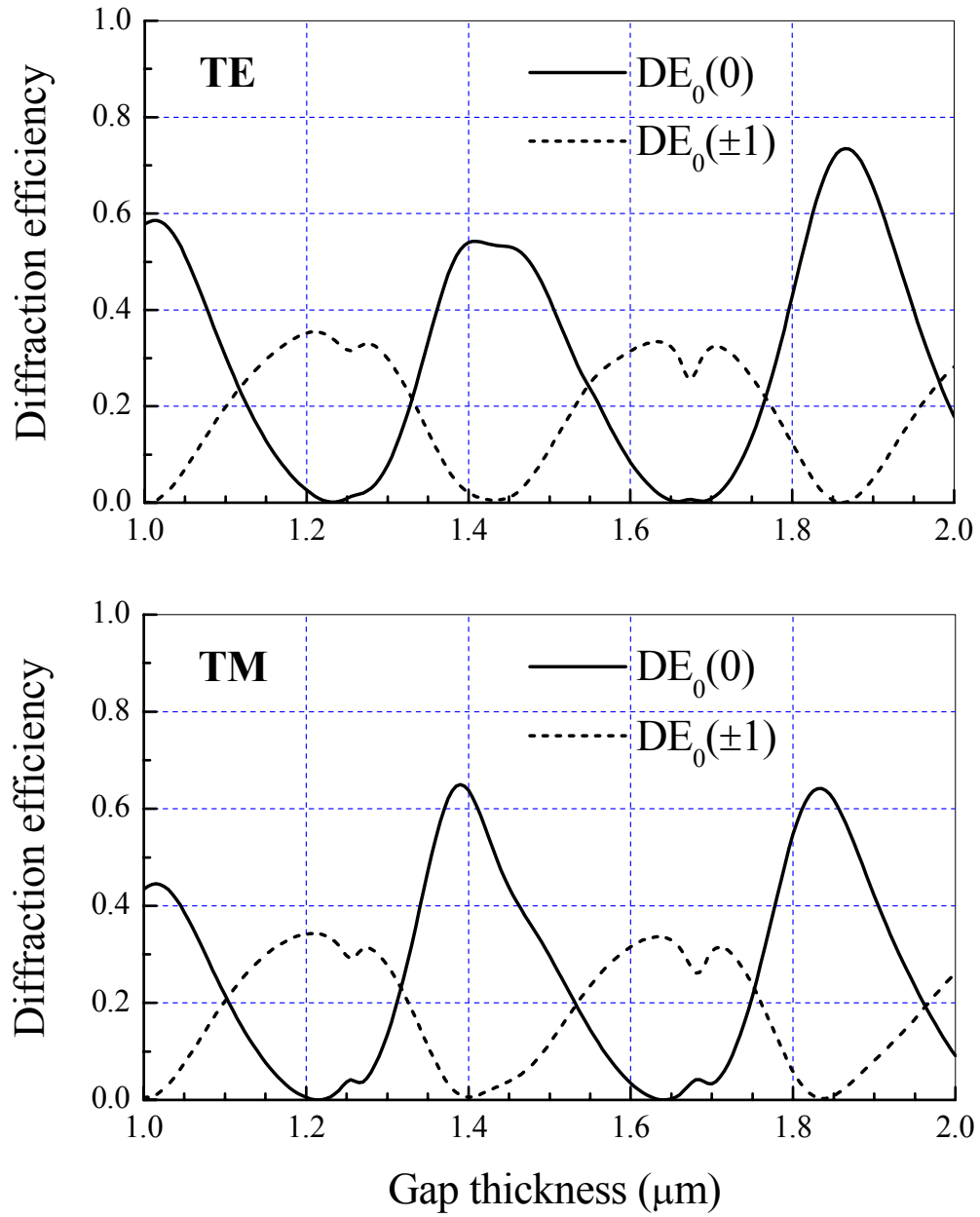


Figure 16. Calculated reflected diffraction efficiencies of the zero order [$DE_0(0)$] and first order [$DE_0(\pm 1)$] for $\Lambda = 4 \mu\text{m}$. [95]

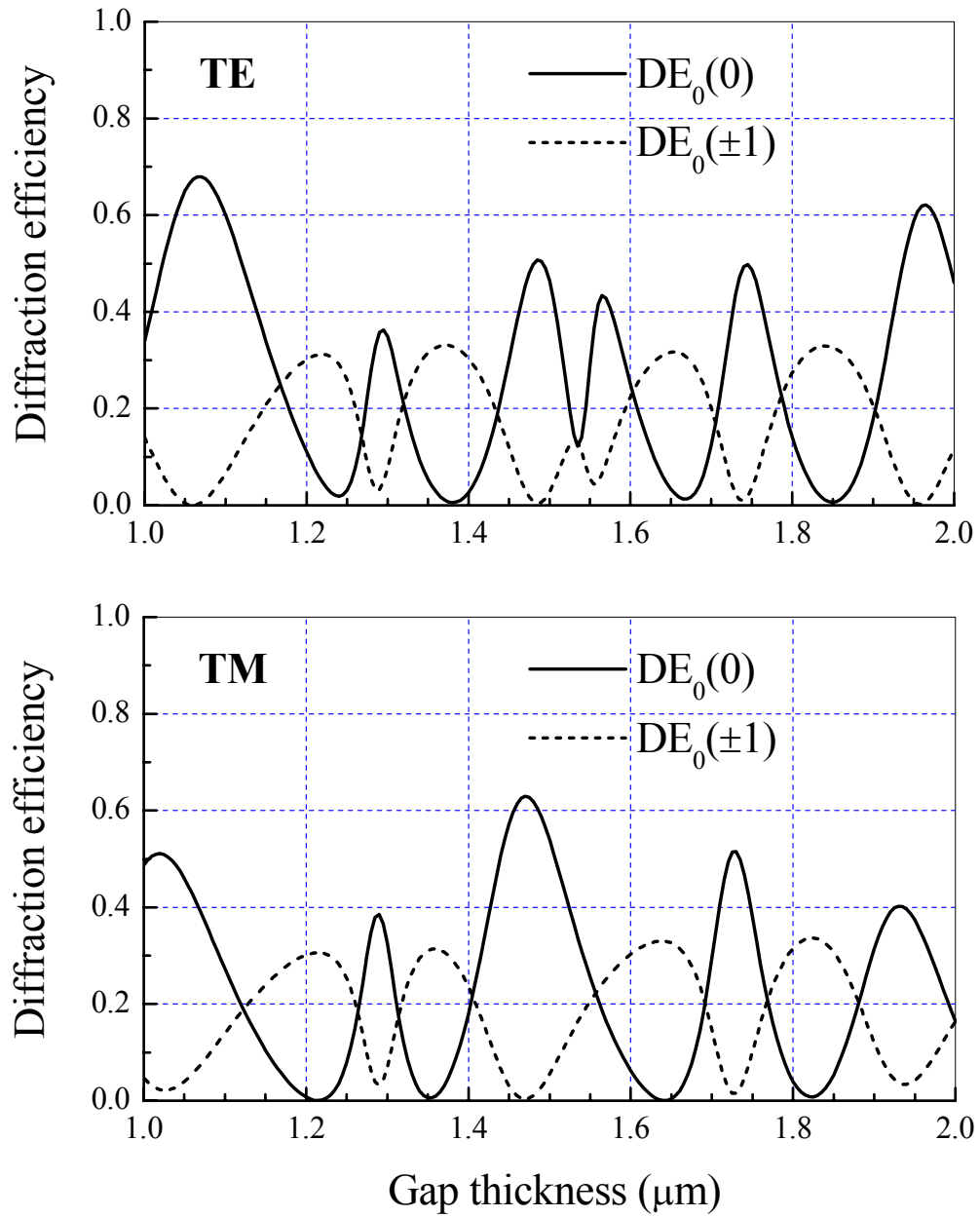


Figure 17. Calculated reflected diffraction efficiencies of the zero order [$DE_0(0)$] and first order [$DE_0(\pm 1)$] for $\Lambda = 2 \mu\text{m}$. [95]

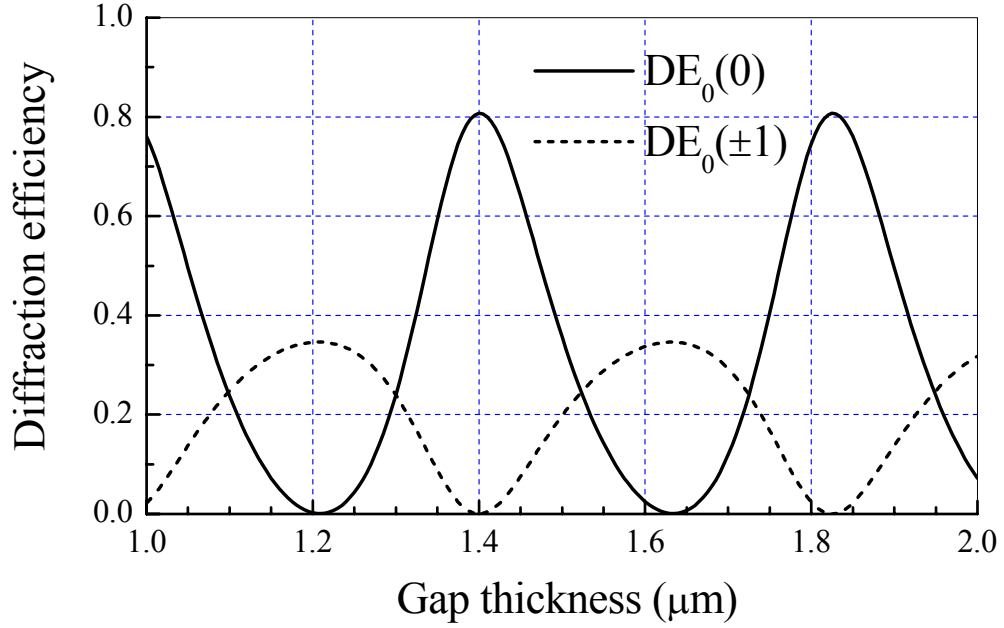


Figure 18. Diffraction efficiencies of the zero order [DE₀(0)] and first order [DE₀(±1)] using the scalar diffraction theory including the absorption loss in the metal layers.[95]

3.1.7 PHASE DISTRIBUTION IN PLANO-CONVEX LENS

Phase distribution in plano-convex lens can be easily approximated as derived in literature [97]. The contour of a plano-convex lens is made in such a way that light from a point source becomes a parallel beam after passing through the lens. This condition gives the hyperbolic contour of the lens. As seen in Figure 19, the lens contour can be written

$$\frac{(z-c)^2}{a^2} - \frac{x^2}{b^2} = 1 \quad (4)$$

where $a = \frac{f}{n+1}$, $b = \sqrt{\frac{n-1}{n+1}}f$, $c = \frac{n}{n+1}f$, f : focal length, n : refraction index of lens. The

phase of the plane wave passed through the lens at x is

$$\phi(x) = kt_0 + nkt_n = k[(a_0 - a - c) - t_n] + nkt_n = kn(a_0 - f) - k \frac{x^2}{2f} \quad (5)$$

where $k = 2\pi / \lambda$. $t_0, t_n, a + c$, and a_0 are defined in Figure 19. It holds in the y direction as the same way. Thus the phase can be written

$$\phi(x, y) = kn(a_0 - f) - k \frac{x^2 + y^2}{2f} \quad (6)$$

where $(a_0 - f)$ is the thickness of the lens

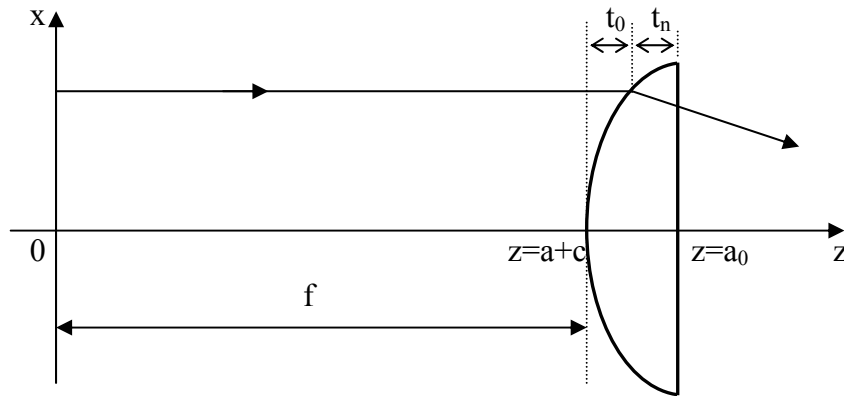


Figure 19. Distribution of a beam passed through a plano-convex lens

3.1.8 SYSTEM SIMULATION

For an analysis of this device, a coordinate system is defined in Figure 20. The analysis begins at the face of the diffraction grating (z_0^-) where the laser enters the device. The input beam is assumed to be a continuous plane wave with amplitude of unity. Since the diffraction grating is ideal, its effects are most easily modeled in the physical domain. In this case, a rectangular function modifies the field amplitude. Thickness of the diffraction grating is assumed 0. Immediately after the grating (z_0^+), the Fourier transform of the exiting field is calculated and propagated to the far edge of the substrate (z_S). The propagation is effectively described using the field's angular spectrum. For computational reasons, it is easier to propagate the field through the lens than calculating the Fourier transform of the field. The resulting field is located at the apex of the lens (z_L). The Fourier transform is then taken and propagated in a similar manner as previously discussed to the measurement surface of the target (z_T). The Fourier transform is reflected and then propagated back to the apex of the lens. The field is then propagated back through the device in the same manner but in reverse order. This process results in the transmitted field exiting the diffraction grating at the original starting point (z_0^-). The field is assumed to be zero from either side of the optical components. In a like manner, the Fourier domain is only evaluated between k and $-k$, as outside this region corresponds to evanescent waves. The reflected field from the face of the diffraction grating adds to the resulting field at the original starting point. This field is propagated to the detector plane (z_D). Table 2 shows the field equation and its angular spectrum that is used in analysis at specific z coordinate. \mathcal{F} and \mathcal{F}^{-1} in Table 1 stand for the Fourier transform and the inverse Fourier transform. u_r and U_r in Table 1 indicate the field and

the angular spectrum of the reflected beam from the surface of the target. n_s and n are indexes of refraction of the substrate and the lens.

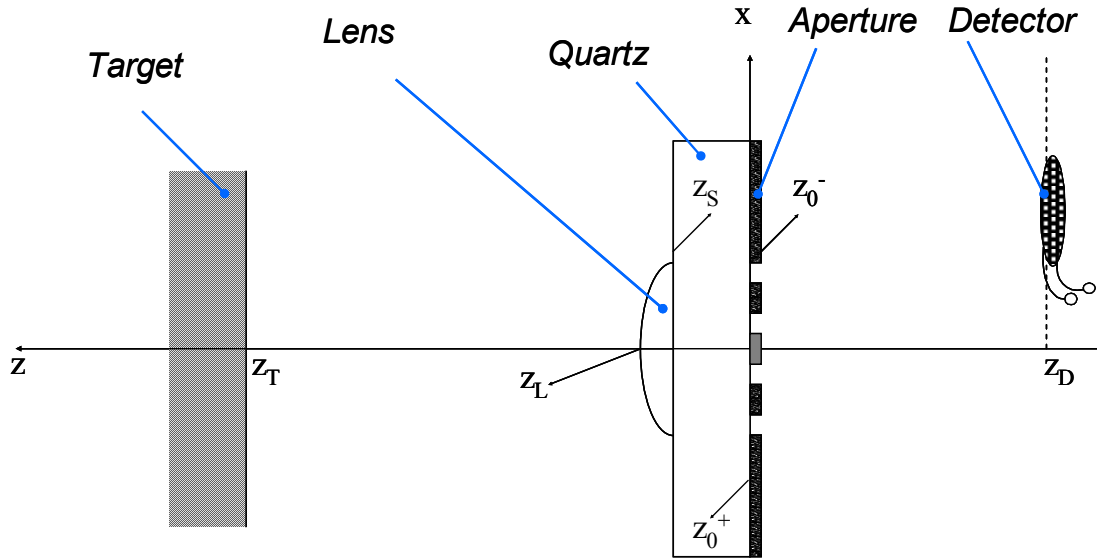
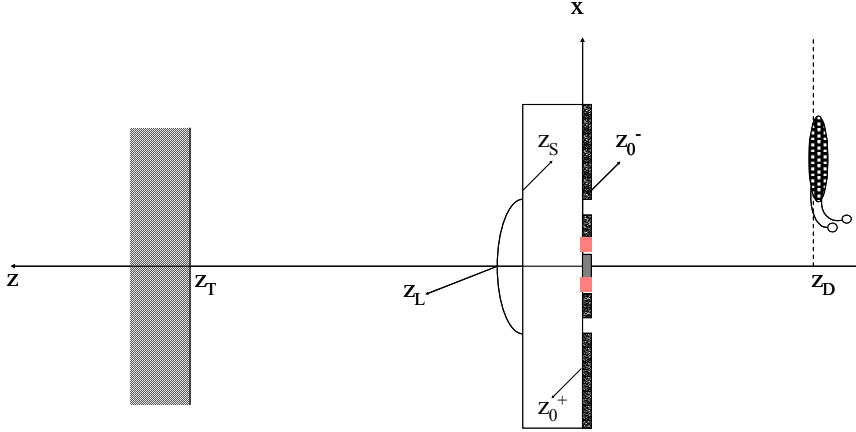
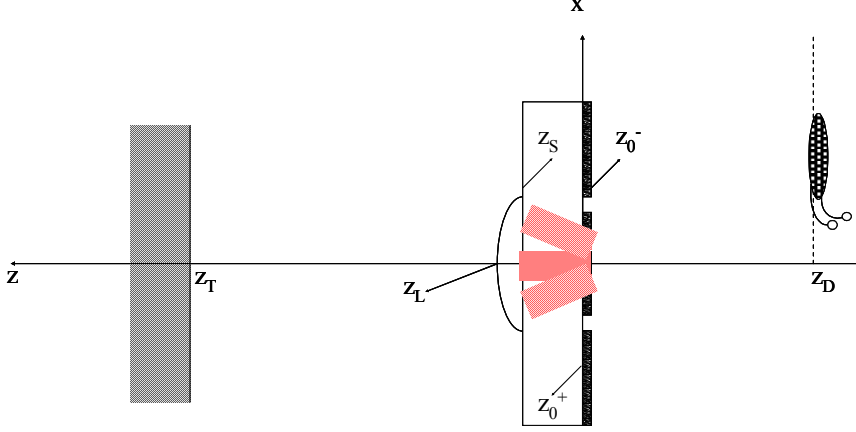
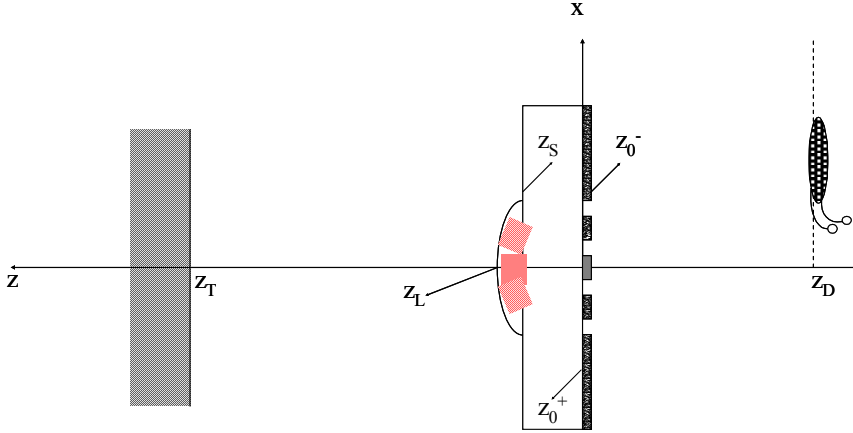
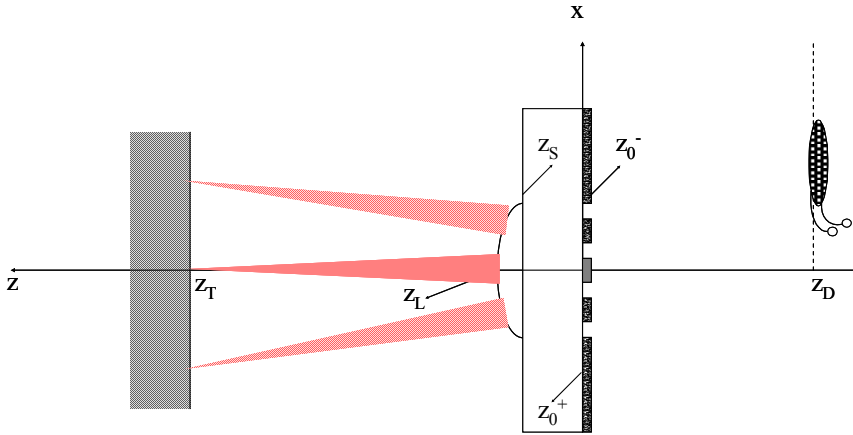


Figure 20. The coordinate system of the device

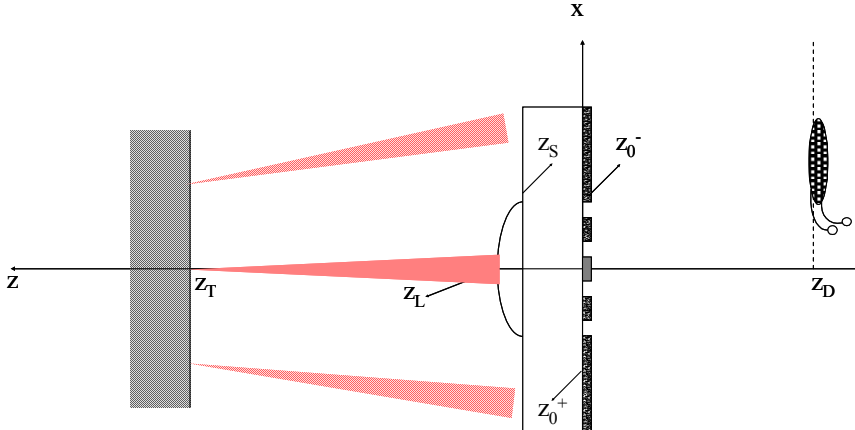
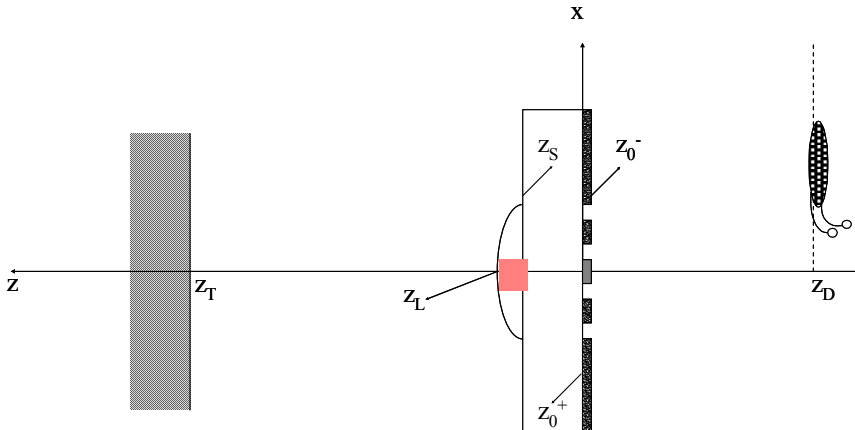
Table 2. The field and the angular spectrum at specific z coordinate

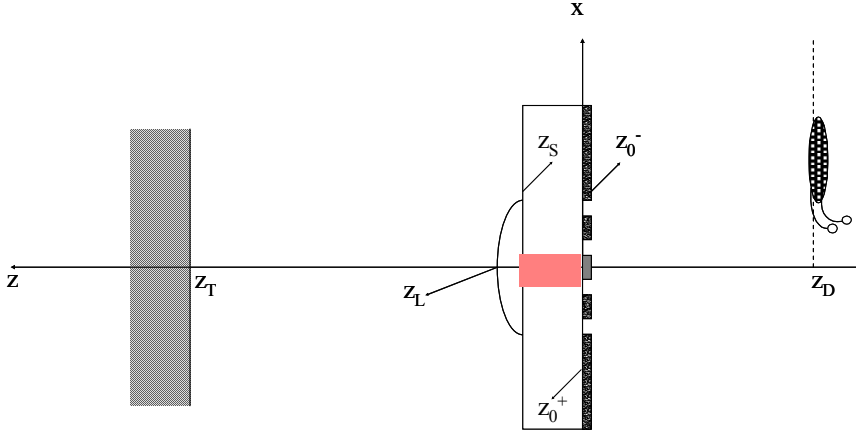
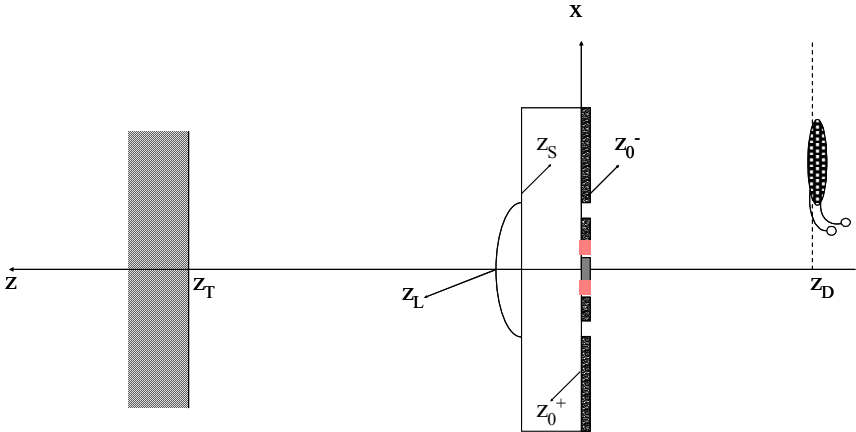
Plane	Field equation and angular spectrum
$z = z_0^-$	$u(x, y, z_0^-) = 1$

$z = z_0^+$	$u(x, y, z_0^+) = \begin{cases} 0 & \text{at diffraction fingers or outside of the diffraction grating} \\ 1 & \text{otherwise} \end{cases}$ $U\left(\frac{\alpha}{\lambda}, \frac{\beta}{\lambda}, z_0^+\right) = \mathcal{F}\left[u(x, y, z_0^+)\right]$ 
$z = z_S$	$U\left(\frac{\alpha}{\lambda}, \frac{\beta}{\lambda}, z_S\right) = U\left(\frac{\alpha}{\lambda}, \frac{\beta}{\lambda}, z_0^+\right) \exp\left(j \frac{2\pi}{\lambda} n_s \sqrt{1 - \alpha^2 - \beta^2} z_S\right)$ $u(x, y, z_S) = \mathcal{F}^{-1}\left[U\left(\frac{\alpha}{\lambda}, \frac{\beta}{\lambda}, z_S\right)\right]$ 

$z = z_L$	$u(x, y, z_L) = u(x, y, z_S) \exp \left\{ -j \frac{2\pi}{\lambda} \left[n(z_L - z_S) - \frac{x^2 + y^2}{2f} \right] \right\}$ $U \left(\frac{\alpha}{\lambda}, \frac{\beta}{\lambda}, z_L \right) = \mathcal{F} [u(x, y, z_L)]$  <p>The diagram shows a coordinate system with a vertical x-axis and a horizontal z-axis. A gray rectangular source plane is located at z = z_T. A lens is located at z = z_L, with a red shaded area representing the lens. A detector plane is located at z = z_D. The lens is centered at z = z_S. The detector plane is at z = z_D. The lens has focal length f. The detector plane is at a distance z_D from the lens. The lens is at a distance z_L from the source plane. The detector plane is at a distance z_D from the lens. The lens is at a distance z_S from the source plane. The detector plane is at a distance z_D from the lens. The lens is at a distance z_L from the source plane. The detector plane is at a distance z_D from the lens. The lens is at a distance z_S from the source plane. The detector plane is at a distance z_D from the lens.</p>
$z = z_T$	$U \left(\frac{\alpha}{\lambda}, \frac{\beta}{\lambda}, z_T \right) = U \left(\frac{\alpha}{\lambda}, \frac{\beta}{\lambda}, z_L \right) \exp \left[j \frac{2\pi}{\lambda} \sqrt{1 - \alpha^2 - \beta^2} (z_T - z_L) \right]$  <p>The diagram shows a coordinate system with a vertical x-axis and a horizontal z-axis. A gray rectangular source plane is located at z = z_T. A lens is located at z = z_L, with a red shaded area representing the lens. A detector plane is located at z = z_D. The lens is centered at z = z_S. The detector plane is at z = z_D. The lens is at a distance z_L from the source plane. The detector plane is at a distance z_D from the lens. The lens is at a distance z_S from the source plane. The detector plane is at a distance z_D from the lens. The lens is at a distance z_L from the source plane. The detector plane is at a distance z_D from the lens. The lens is at a distance z_S from the source plane. The detector plane is at a distance z_D from the lens.</p>

After the beam reflects from the surface of the target

<p>$z = z_L$</p>	$U_r\left(\frac{\alpha}{\lambda}, \frac{\beta}{\lambda}, z_L\right) = -U\left(\frac{\alpha}{\lambda}, \frac{\beta}{\lambda}, z_T\right) \exp\left[j \frac{2\pi}{\lambda} \sqrt{1 - \alpha^2 - \beta^2} (z_T - z_L)\right]$ $u_r(x, y, z_L) = \mathcal{F}^{-1}\left[U_r\left(\frac{\alpha}{\lambda}, \frac{\beta}{\lambda}, z_L\right)\right]$ 
<p>$z = z_S$</p>	$u_r(x, y, z_S) = u_r(x, y, z_L) \exp\left\{-j \frac{2\pi}{\lambda} \left[n(z_L - z_S) - \frac{x^2 + y^2}{2f}\right]\right\}$ $U_r\left(\frac{\alpha}{\lambda}, \frac{\beta}{\lambda}, z_S\right) = \mathcal{F}[u_r(x, y, z_S)]$ 

$z = z_0^+$	$U_r\left(\frac{\alpha}{\lambda}, \frac{\beta}{\lambda}, z_0^+\right) = U_r\left(\frac{\alpha}{\lambda}, \frac{\beta}{\lambda}, z_s\right) \exp\left(j \frac{2\pi}{\lambda} n_s \sqrt{1 - \alpha^2 - \beta^2} z_s\right)$ $u_r(x, y, z_0^+) = \mathcal{F}^{-1}\left[U_r\left(\frac{\alpha}{\lambda}, \frac{\beta}{\lambda}, z_0^+\right)\right]$ 
$z = z_0^-$	$u_r(x, y, z_0^-) = u_r(x, y, z_0^+) \text{diag}\left[u(x, y, z_0^+)\right] + u_{r0}(x, y, z_0^-)$ <p>where, $u_{r0}(x, y, z_0^-) = \begin{cases} 1 & \text{at diffraction fingers} \\ 0 & \text{otherwise} \end{cases}$</p> $U_r\left(\frac{\alpha}{\lambda}, \frac{\beta}{\lambda}, z_0^-\right) = \mathcal{F}\left[u_r(x, y, z_0^-)\right]$ 

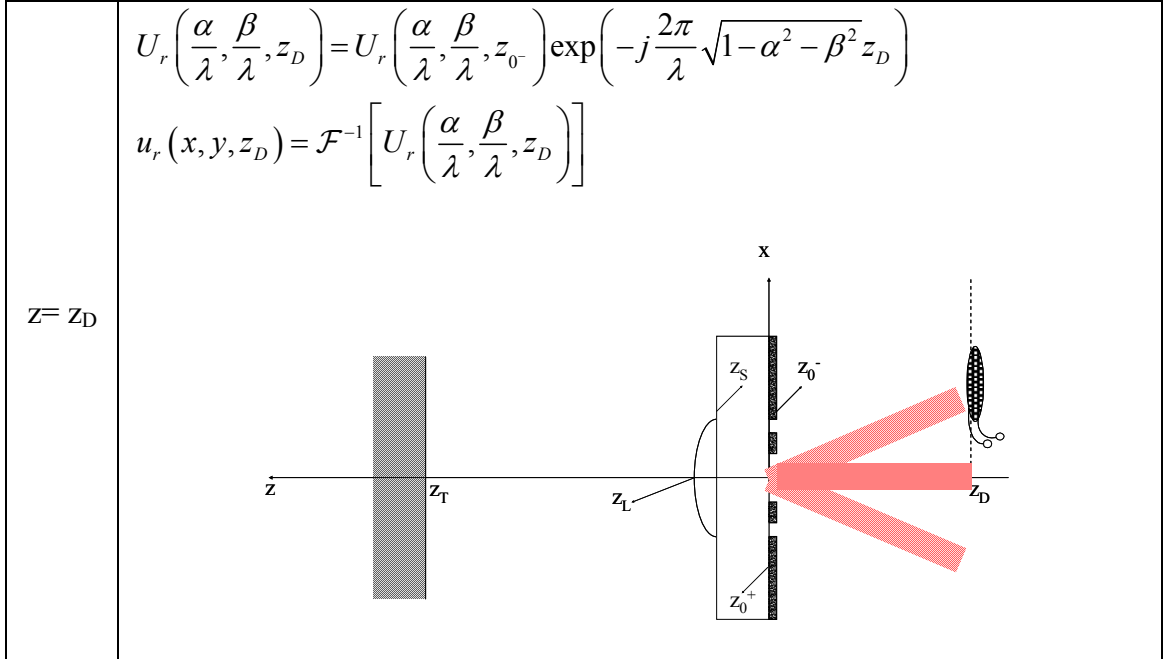


Figure 21 shows the intensity along the x -axis at detector positions for different target positions when the designed lens is used. It is a 1-D analysis on (x, z) plane. According to the 2-D diffraction theory, the 2nd lobe might be seen around $216 \mu\text{m}$ ($=1000 \times \tan[\sin^{-1}(0.6328/3)]$) if the photo detector is located at $1000 \mu\text{m}$ behind the diffraction grating. By locating the photo detector around this 2nd lobe, intensity variations can be used to identify different target positions. Figure 22 shows these variations by locating the photo detector having a $200 \mu\text{m}$ width at a $216 \mu\text{m}$ offset from the principal axis at $1000 \mu\text{m}$ behind the diffraction gratings. A $3 \mu\text{m}$ period and $1.5 \mu\text{m}$ of diffraction gratings is used in this simulation. As expected, it shows about $0.3 \mu\text{m}$ period. It is impressive that the photo detector signal shows strong interference. This apparent interference makes it easy to separate each signal to determine the distance change. Figure 23 shows the phase of the field at the back plane of the lens. It is 0° as expected. Good focusing can be expected by the same phase of the incident beam into the lens.

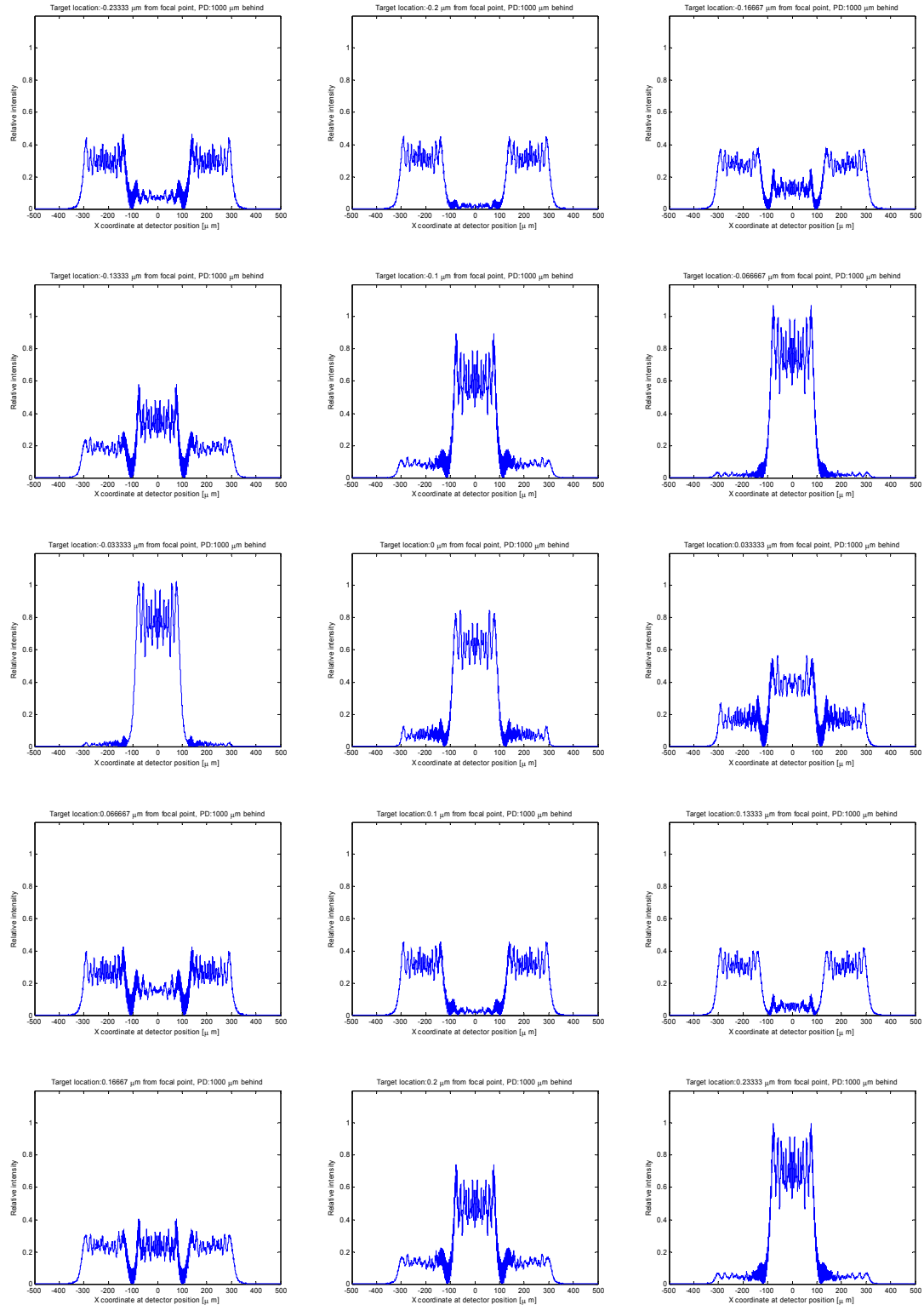


Figure 21. Intensity variation on the plane with photo detector. Photo detector plane is 1000 μm behind from diffraction grating. Target moves $\pm 0.23 \mu\text{m}$ at the focal point

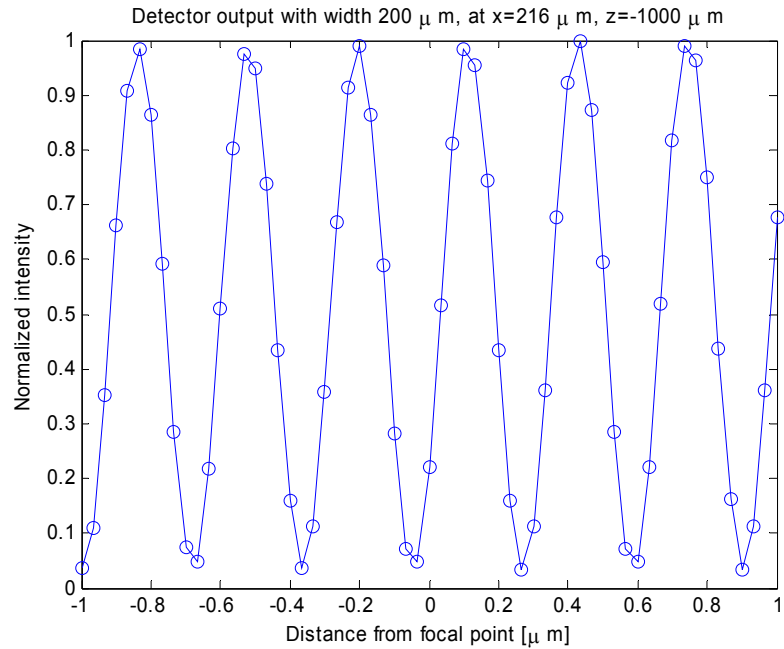


Figure 22. Photo detector signal variation. Lens and diffraction grating are on different sides. Photo detectors located at 216μm from principal axis, 1000 μm behind the diffraction gratings. Target moves ±1 μm at the focal point

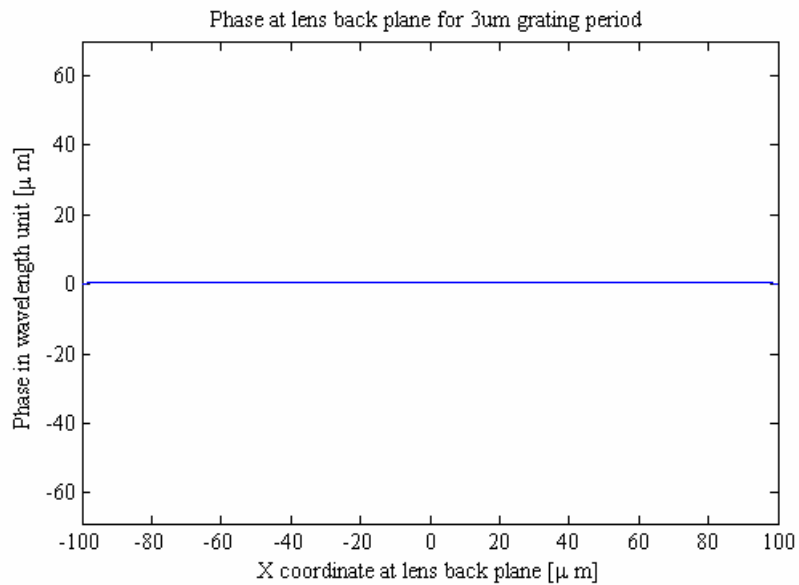


Figure 23. Phase at lens back plane

3.1.9 EXPERIMENTAL VALIDATION OF FEASIBILITY ANALYSIS

The purpose of the described experiment was to demonstrate the validity of the analysis results. In the experiment, the plano-convex lens having F-number 2.0, focal length 12.7mm, diameter 6.35mm, thickness 3.819mm and radius of curvature 6.563mm was used. The lens material is BK-7 having an index of refraction of 1.51059, at a wavelength 632.8 nm. The fabricated diffraction grating has $\Lambda=12\mu\text{m}$ and finger size, $3\mu\text{m}$. Figure 24 shows the analysis results of the intensity distribution on the target. It is a 1-D analysis on (x, z) plane. A monochromatic ray (HeNe laser) and no aberrations are assumed. The normalized intensity on the surface of the target was measured with a photo detector having 0.4mm width in experimental set-up as seen in Figure 25. Figure 26 shows the experimental results. The circle in Figure 26 represents measured constructively interfered wave vector position on the surface of the target. Table 3 compares it with calculated results from scalar diffraction theory. They show good agreement.

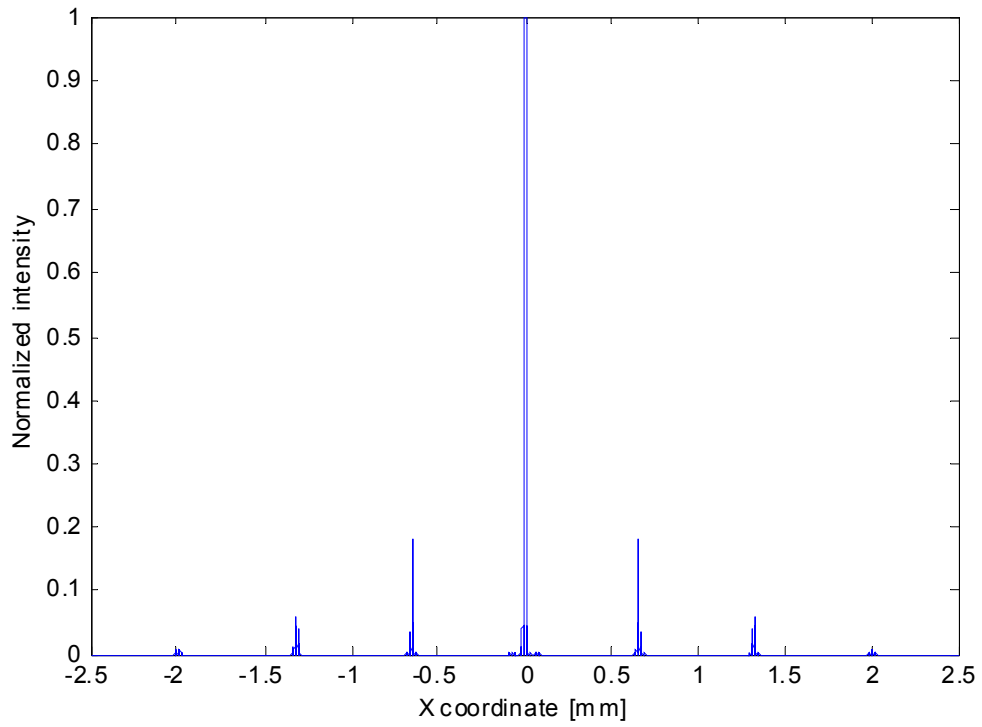


Figure 24. Intensity distribution on the target in analysis

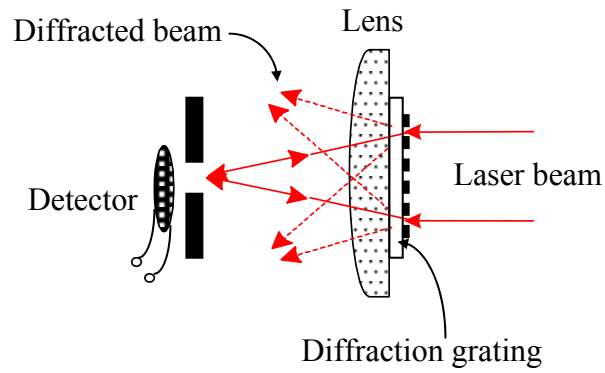


Figure 25. Schematic of the experiment set-up

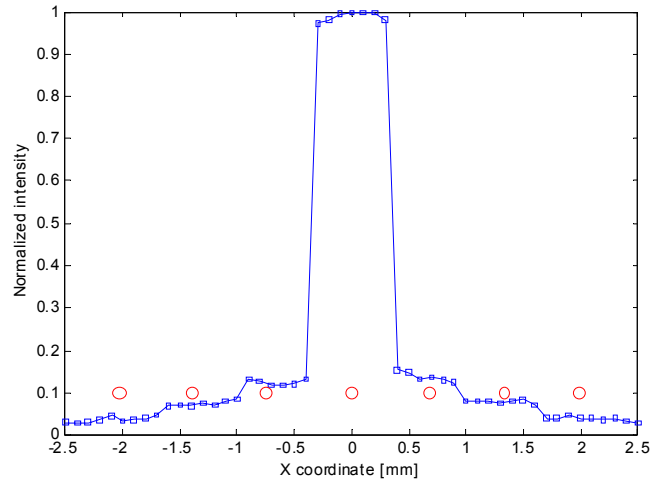


Figure 26. Measured Intensity distribution on the target in the experiment

Table 3. Comparison of location of each diffracted order

Order	Scalar diffraction theory	Experiment
0	0	0
1	0.66	0.67
2	1.39	1.33
3	1.99	1.98

To ensure the feasibility of the device, the interferometer experimental set-up in Figure 27 was used. The commercial plano-convex lens having focal length of 12.6mm and diameter of 6.35 mm and the fabricated diffraction grating having $\Lambda=12\mu\text{m}$ and finger size of $3\mu\text{m}$ was used in the experiment. A HeNe laser was employed as the light source and a mirror was used as the reflecting surface. Figure 28 shows the intensity at the detector as a function of distance from focal point to target (mirror). The intensity was changed when the target moves $\pm 1\text{mm}$ from focused position in the set-up. Figure 28

shows the 5th diffraction order intensity as a function of distance from the focal depth. The experiment seen in this figure shows one cycle per travel distance of $\lambda/2$. For HeNe laser ($\lambda=632.8\text{nm}$), the travel distance is about $0.3\ \mu\text{m}$. This agrees quite well with the expected intensity period as seen in Figure 22.

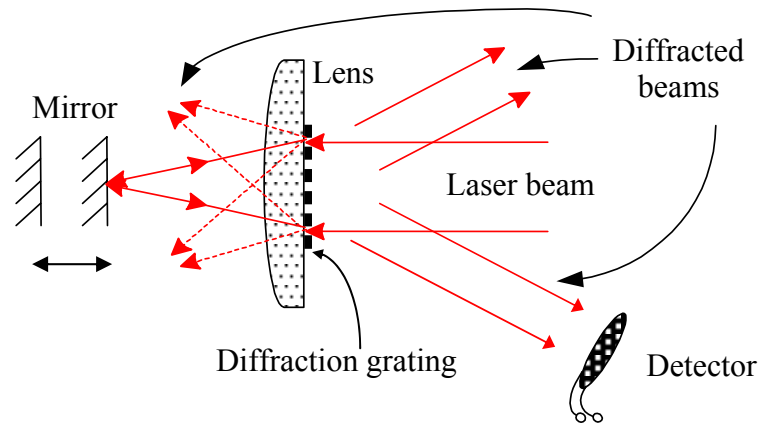


Figure 27. Schematic of the experiment set-up

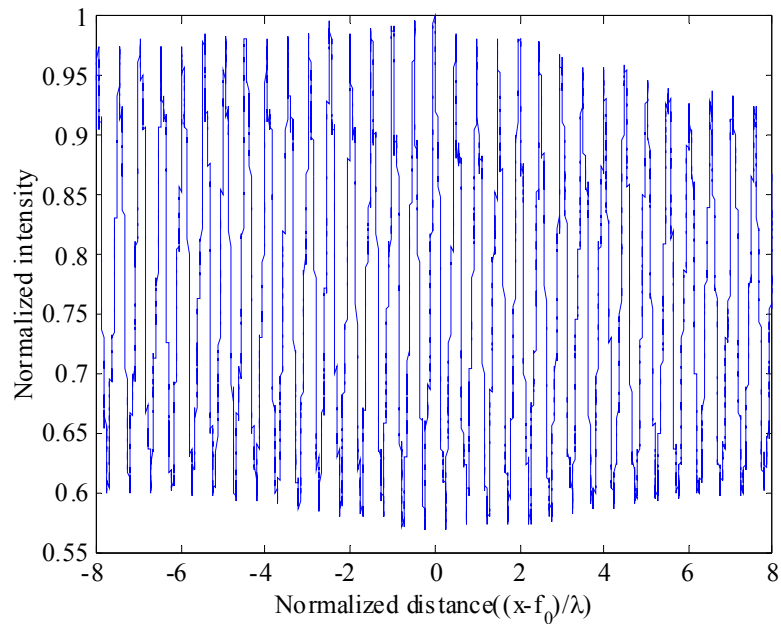


Figure 28. Measured diffraction intensity at the detector in normalized distance

3.2 MICROLENS

For ease of fabrication, the plano-convex or convex-plano lens is considered. A lower F-number is desirable to give the narrower depth of focus. The narrower depth of focus has the benefit of measuring inclined surfaces. A lens diameter of 200 μm and focal length of 1000 μm is chosen after considering feasible device size, commercial lens specifications, and feasible microlens specifications in [61]. Reflow of photo resist can be used to fabricate micro refractive lenses. Surface tension causes the melted photo resist to form a spherical shape if the mass of the fluid is negligible [73]. The fluid in the stable condition forms a shape to minimize surface area for the same volume. The surface tension causes the lens to have a minimum surface area and a minimum surface energy. This spherical shape can be used as a plano-convex or convex-plano lens. This type of lens has been made from AZ P4620. In literature [65], the lens has 300 μm diameter and 670 μm focal length. The refractive index of AZ P4620 is 1.6176. For plano-convex lens having a radius of curvature of R and a refraction index of n, the focal distance of f is

$$f = \frac{h}{\tan \left[\sin^{-1} \left(\frac{nh}{R} \right) - \sin^{-1} \left(\frac{h}{R} \right) \right]} - R + \sqrt{R^2 - h^2} \quad (7)$$

for an axial ray of offset h from the principal axis. Figure 29 shows this relationship of f and h for plano-convex lens that has radius of curvature from 616 μm to 620 μm . The focal length of each size for each axial lay displacement reveals that the 618 μm of a radius of curvature is the most desirable. The volume of this desirable lens is $1.2821 \times 10^5 \mu\text{m}^3$.

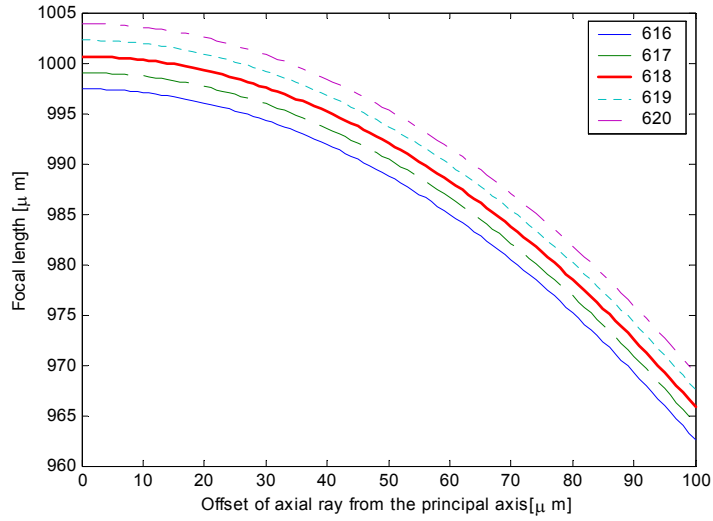


Figure 29. Focal length of the designed plano-convex lens at each axial ray displacement

For convex-plano lens, the focal distance is

$$f = \frac{\left[\left[\frac{h}{\left\{ n \sin \left[\sin^{-1} \left(\frac{h}{R} \right) - \sin^{-1} \left(\frac{h}{nR} \right) \right] \right\}} \right] + R - d_s \right] \tan \left[\sin^{-1} \left(\frac{h}{R} \right) - \sin^{-1} \left(\frac{h}{nR} \right) \right]}{\tan \left(\sin^{-1} \left\{ n \sin \left[\sin^{-1} \left(\frac{h}{R} \right) - \sin^{-1} \left(\frac{h}{nR} \right) \right] \right\} \right)} \quad (8)$$

where, d_s is a sag of the lens. Figure 30 shows this relationship of f and h for convex-plano lens that has radius of curvature from 619 μm to 623 μm . The focal length of each size for each axial ray displacement reveals that the 621 μm of a radius of curvature is the most desirable. The volume of this desirable lens is $1.2758 \times 10^5 \mu\text{m}^3$.

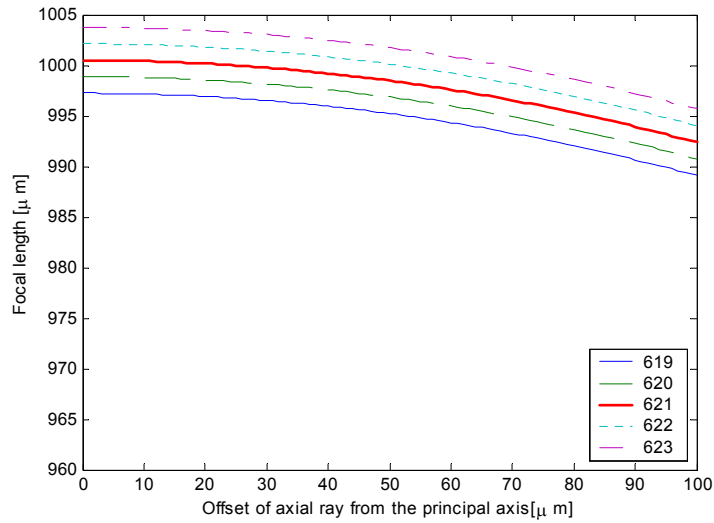


Figure 30. Focal length of the designed convex-plano lens at each axial ray displacement

3.3 DEFORMABLE GRATING

3.3.1 DESIGN PARAMETERS STUDY

The ultimate goal of this study is to implement a system shown in Figure 13 which consists of a deformable grating to adjust the sensitivity of the micro interferometer dynamically. The deformable grating is electrostatically actuated and combines the capability of optimization of measurement in a single device. The grating was designed to have 3-6 μm periods in order to accommodate a photo diode placed 1.5-3.0 mm above the grating. The important points in design of the deformable grating are as follows:

- a) The voltage for the electrostatic static force is within 50V.
- b) The working range of grating is larger than a half wavelength.
- c) The stiffness of the grating membrane gives enough band width, more than 10 kHz.
- d) The bottom electrode does not block the light source.
- e) A flat zone at illumination is desirable to increase diffraction efficiency.

To determine the bottom electrode location and size, a), b), d), and e) should be considered. To design a grating membrane, a), b), c), and e) should be considered. a) and b) requires a soft structure, but c) and e) requires a strong structure. Thus, a design compromise is needed to satisfy both requirements.

The design parameters are grating membrane's thickness and length and electrode's location and length. The grating material is fixed aluminum due to its high stiffness and good reflectivity. The grating membrane can be considered as a combination of many single beam structures. It is a convenient way to look at each parameter's change effect on the overall stiffness through a numerical analysis of the single beam. Figure 31 shows a beam and an underneath electrode. Since the grating beam is symmetric by a half, a whole beam can be analyzed by a half model with the constraint of $\Delta x=0$ at $x=L_m$, a half of grating length. The electrostatic force, $F_e(x)$ between the two conductors is

$$F_e(x) = \epsilon_0 \frac{WL_e V^2}{2h_g^2} \quad (9)$$

where, ε_0 : a permittivity of the air, WL_e : an overlapped area, V : an applied voltage, h_g : a gap. Thus, electrostatic force is proportional to overlapped area, voltage square, and 1/gap square. Beam in bending equation is

$$\frac{d^2}{dx^2} \left(EI \frac{d^2 y}{dx^2} \right) - T \frac{d^2 y}{dx^2} = f_l(x), \text{ where } f_l(x) = \varepsilon_0 \frac{WV^2}{2h_g^2} \quad (10)$$

where, E : Young's modulus of the beam material, I : moment of inertia about Z, T : tensile force by residual stress. The shape in bending depends on beam stiffness, residual stress, and electrostatic force/beam length.

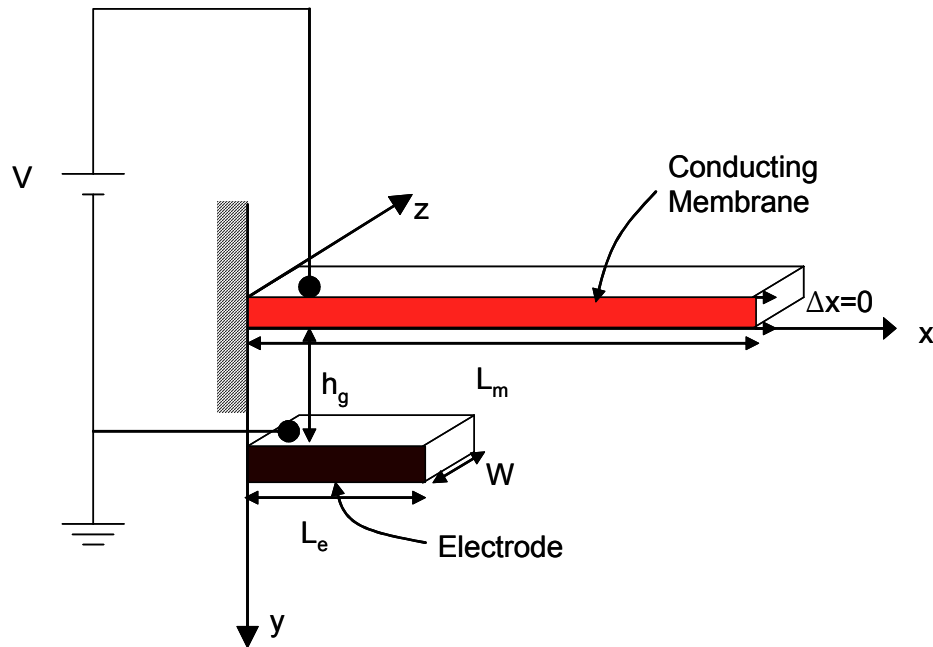


Figure 31. Schematic of an electrostatic actuated beam

Beam stiffness is determined from a selected material and a beam cross section shape. Residual stress in the beam is somewhat controllable in sputtered process and by

thermal treatment. But generally it is difficult to control precisely. Electrostatic force is determined from an electrode location, size and a sacrificial layer thickness between the two conductors. Since the electrode should not block the light source, it is located on the side of the membrane. That makes it harder to deform the membrane by the same size of electrode, gap and voltage. But it is useful to get a flat deflection in the middle of the grating where there is an illumination area. Figure 32 shows a force diagram of the small element of the beam. By applying a force summation,

$$\begin{aligned}
 \sum F_y = 0, \quad \frac{dV}{dx} + f_l + T \frac{1}{\rho} &= 0 \\
 \sum M_o = 0, \quad \frac{dM_b}{dx} + V &= 0 \\
 \text{Since, } \frac{1}{\rho} = \frac{M_b}{EI} \text{ and } M_b = EI \frac{d^2 y}{dx^2} & \\
 \therefore \frac{d^2}{dx^2} \left(EI \frac{d^2 y}{dx^2} \right) - T \frac{d^2 y}{dx^2} = f_l & \quad (11)
 \end{aligned}$$

where, M_b : a bending moment, V_s : surface force, f_l : distribution force per unit length.

The beam in bending has a force T from residual stress. It is assumed that radius of curvature of ρ is very big, i.e. small bending.

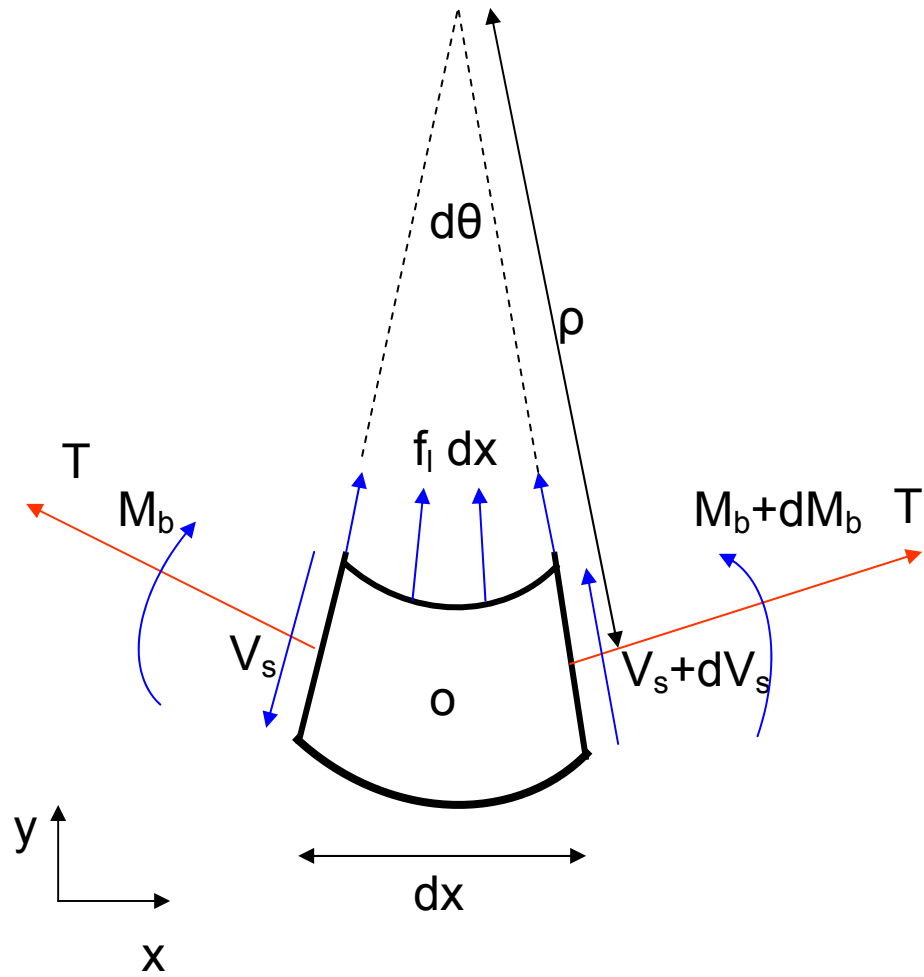


Figure 32. Force diagram for a small element in the beam

Figure 33 shows a conversion of the beam problem having a electrostatic force into a distributed force loaded beam problem for the whole grating beam. Figure 34 shows its force diagram. F_r is reaction force.

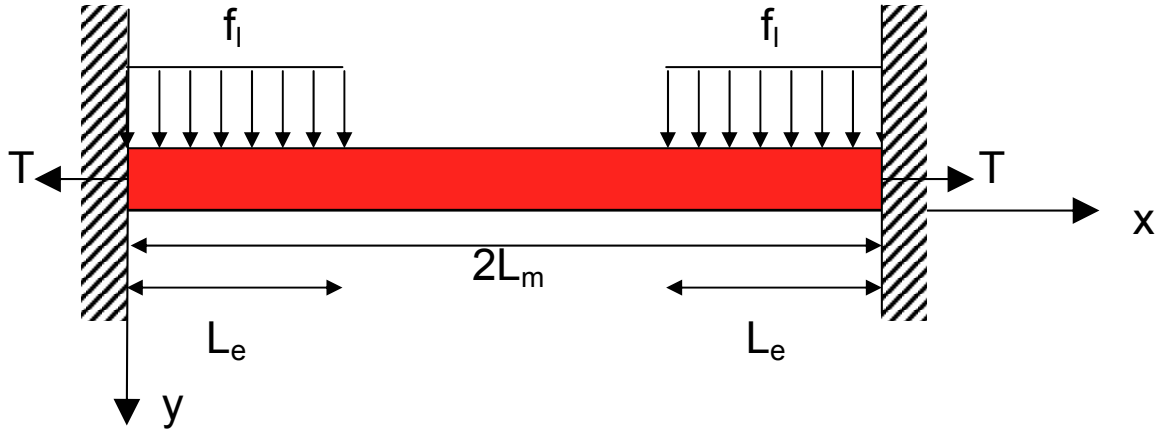


Figure 33. Beam with electrostatic forces and residual tension forces

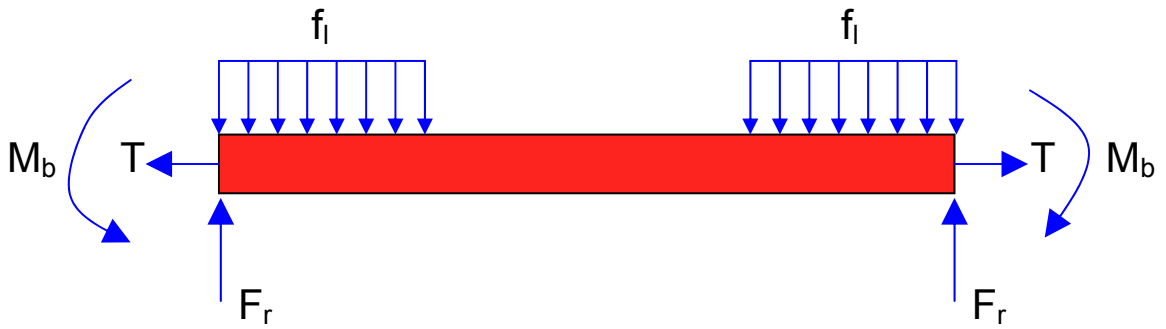


Figure 34. Force diagram for the beam in Figure 33

Solution of the bending equation with constant residual stress, constant EI and constant f_l (gap variation along the beam is ignored) as follows. Detail solution procedures are in appendices.

$$\text{At } 0 < x < L_e, EI \frac{d^2 y}{dx^2} - Ty = \frac{1}{2} f_l x^2 - F_r x + M_b \quad (12)$$

$$\text{At } L_e < x < L_m, EI \frac{d^2 y}{dx^2} - Ty = -\frac{1}{2} f_l L_e^2 + M_b \quad (13)$$

Figure 35 shows two examples of the case study. The assumed parameter was $h_g=1.8 \mu\text{m}$, $L_e=50 \mu\text{m}$, $L_m=100 \mu\text{m}$, $\epsilon_0=8.854 \times 10^{-12} \text{ F/m}$, tensile stress=5 Pa. (a) is without tension and (b) is with tension. It is clear that the tension causes an increase of electrostatic force for the same deflection magnitude but helps to get a zone at center if you compare the same deflection magnitude, $0.1 \mu\text{m}$ at both cases.

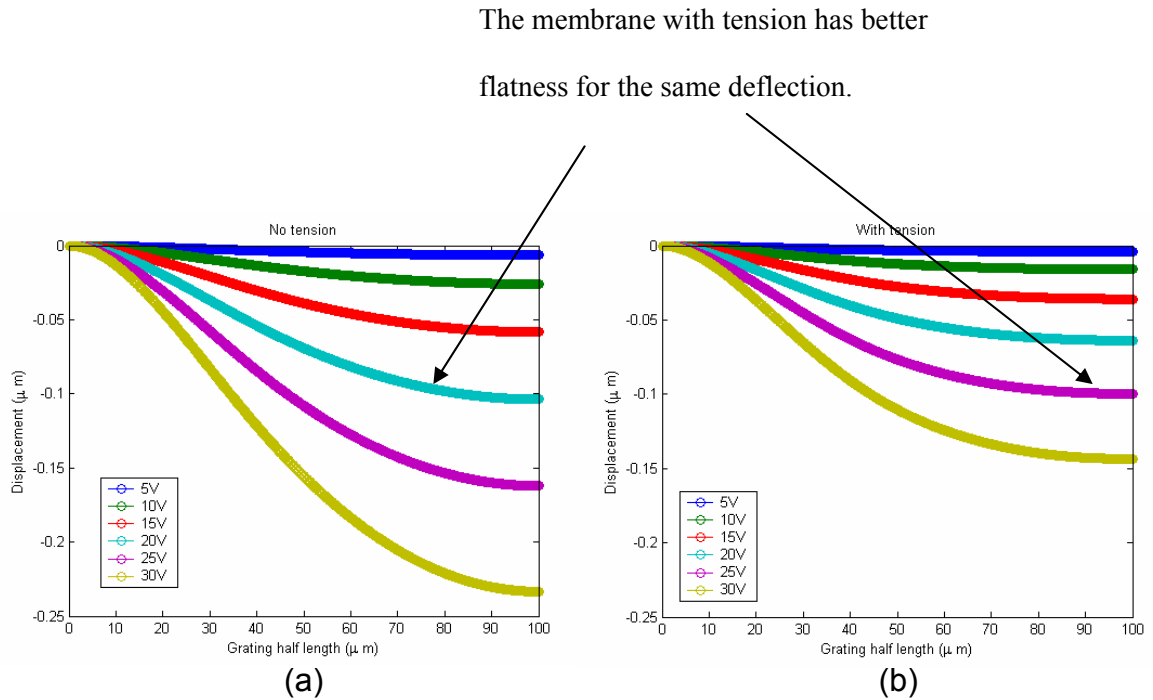


Figure 35. Deflection of the beam in different voltages (a) without residual tension (b) with residual tension

3.3.2 FEM ANALYSIS

ANSYS, a finite element analysis package, is used to design the grating beam. In ANSYS, an electric field model and a mechanical structure model are defined separately for the same geometry (mesh). In electric field model, two conductors and air's permittivity and voltage between two conductors are required. In a fabricated device, there is a 2000\AA oxide insulator on top of the bottom electrode. This layer is ignored in

the model. In mechanical structure model, material properties such as Young's Modulus, Poisson's ratio, and density are required. The solver runs the model until an electrostatic energy converges within a tolerance in electric field model and structural maximum displacement converges within a tolerance in mechanical structure model. Figure 36 shows parameters for the case studies. Figure 37 shows the beam deformation for three different electrode lengths (L_e) and zero offset. To compare the deformation along the beam, the cases of the same deflection magnitude at end are collected. Thus, electrode length are different, 25V, 13.5V and 10.3V are required to deflect $0.22\ \mu\text{m}$ for 50, 75, 100 μm electrode lengths. In this comparison, the shorter length of the electrode is the better to get a flat zone at the end but requires more voltage.

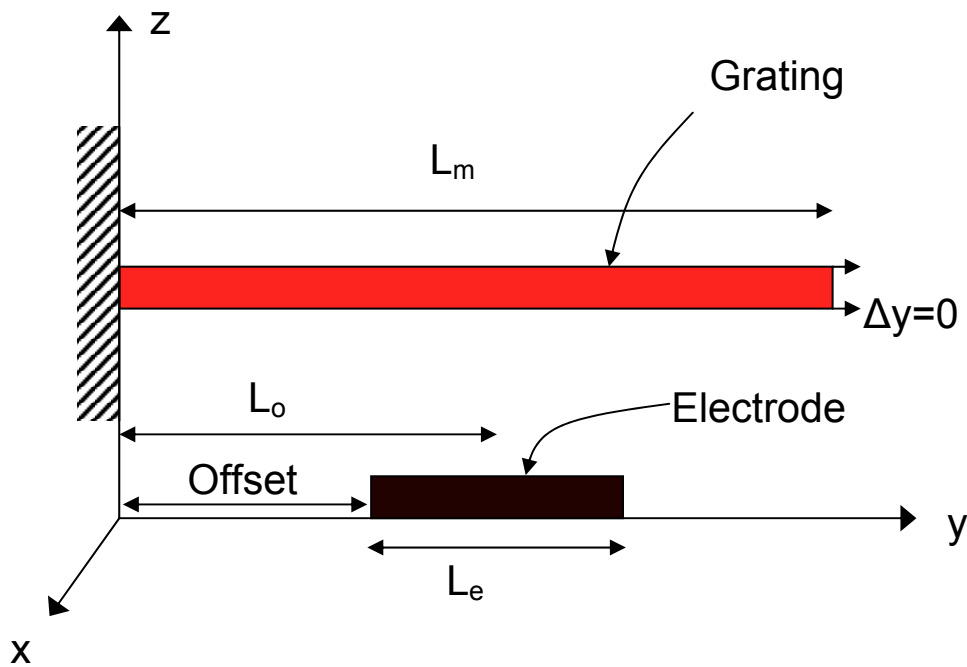


Figure 36. Schematic of a grating and an electrode for the case analysis

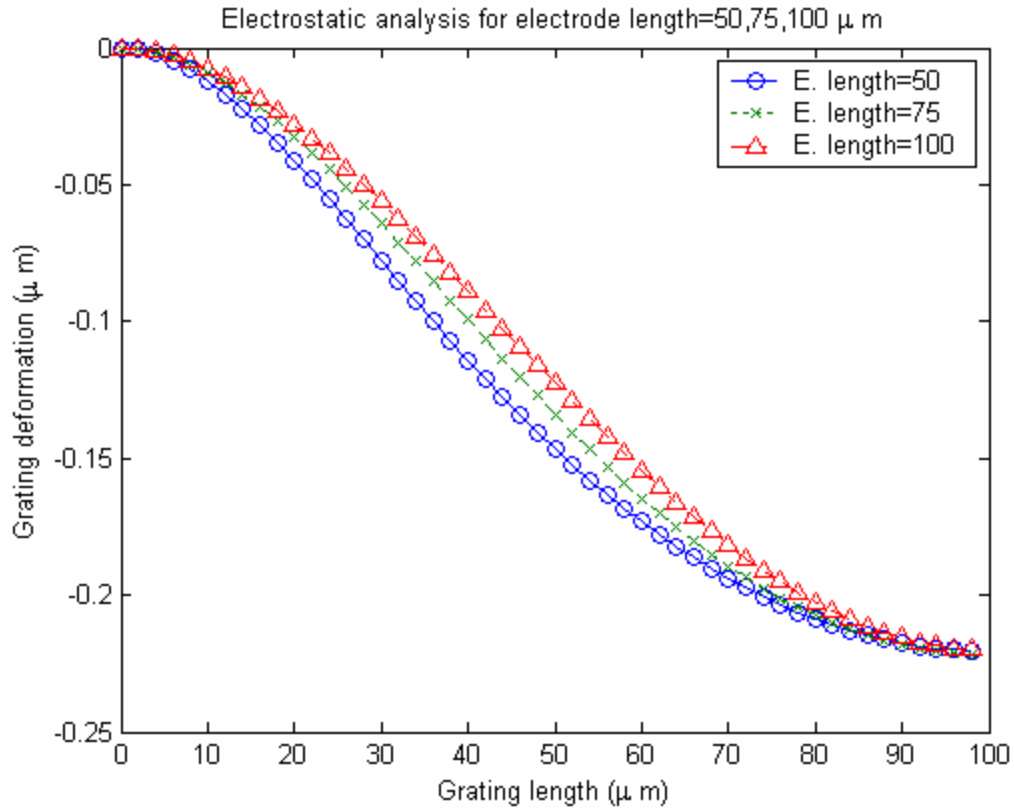


Figure 37. Grating deformation for the different electrode length with no offset

It is noticeable that the beam was bent more in the FEM analysis result than in the numerical result in Figure 38 for the same parameters. The reason is that the sidewall of the beam was modeled in FEM analysis, thus the sidewall contributes to the deformation of the beam. Another reason is the electrostatic force along the beam was constant in numerical model and but it increased along the beam at FEM model which is closer to real.

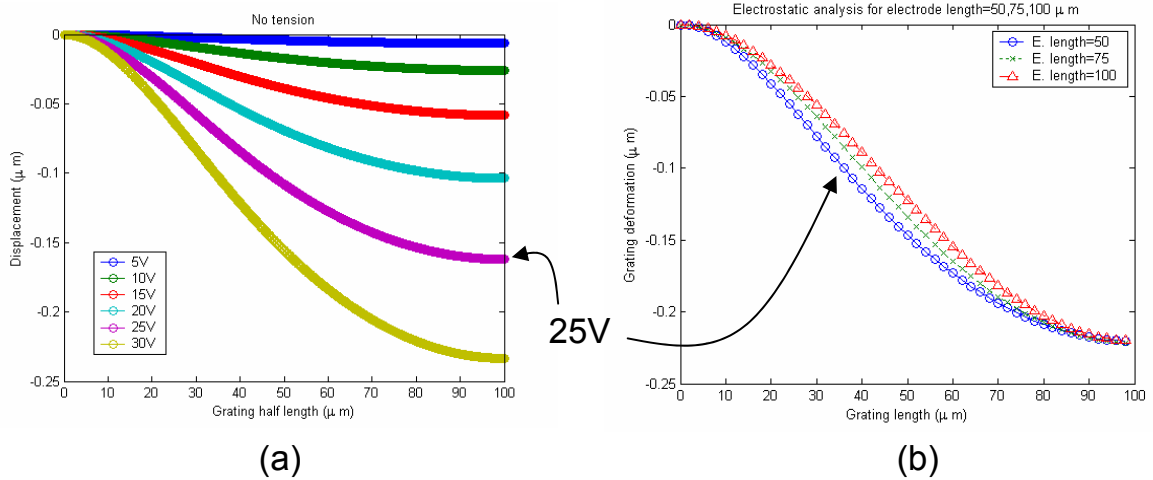


Figure 38. Deformation for the different electrode length with no offset (a) numerical analysis result (b) FEM analysis result

The study results for different electrode location of the same length of $50\ \mu\text{m}$ are shown in Figure 38. 25V, 15V and 11.3V are required to deflect $0.22\ \mu\text{m}$ in the middle of the grating for different electrode locations (L_0) from the beam edge of 25, 50, 75 μm electrode lengths. In this comparison, the shorter length of the electrode is the better to get a flat zone at the end but requires more voltage.

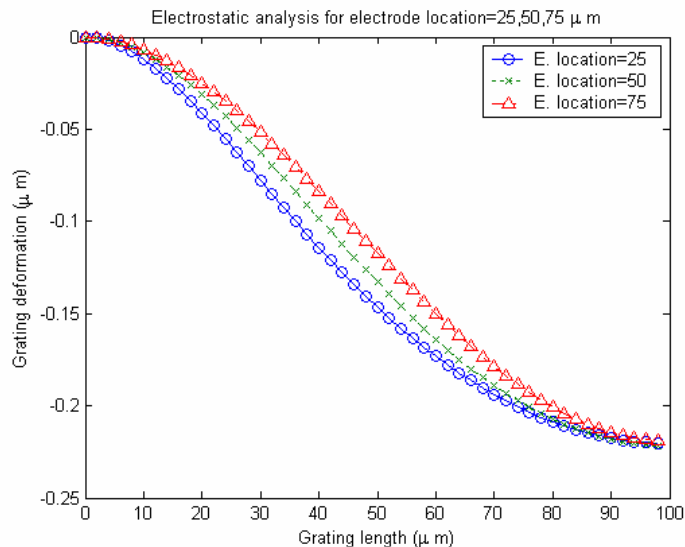


Figure 39. Grating deformation for the same electrode length of $50\ \mu\text{m}$ with different L_0

To get a further flat zone in the middle of the grating beam, thickness of the illumination region was increased from 1 μm to 2 μm . Figure 40 shows how this change makes a difference. 32.5V and 26.8V are required for 0.26 μm deformation in the middle of the grating of the grating beam with increasing thickness and without increasing thickness respectively. It is clear that increased stiffness of the illumination zone contributes to increasing flatness at the region with a cost of increased voltage.

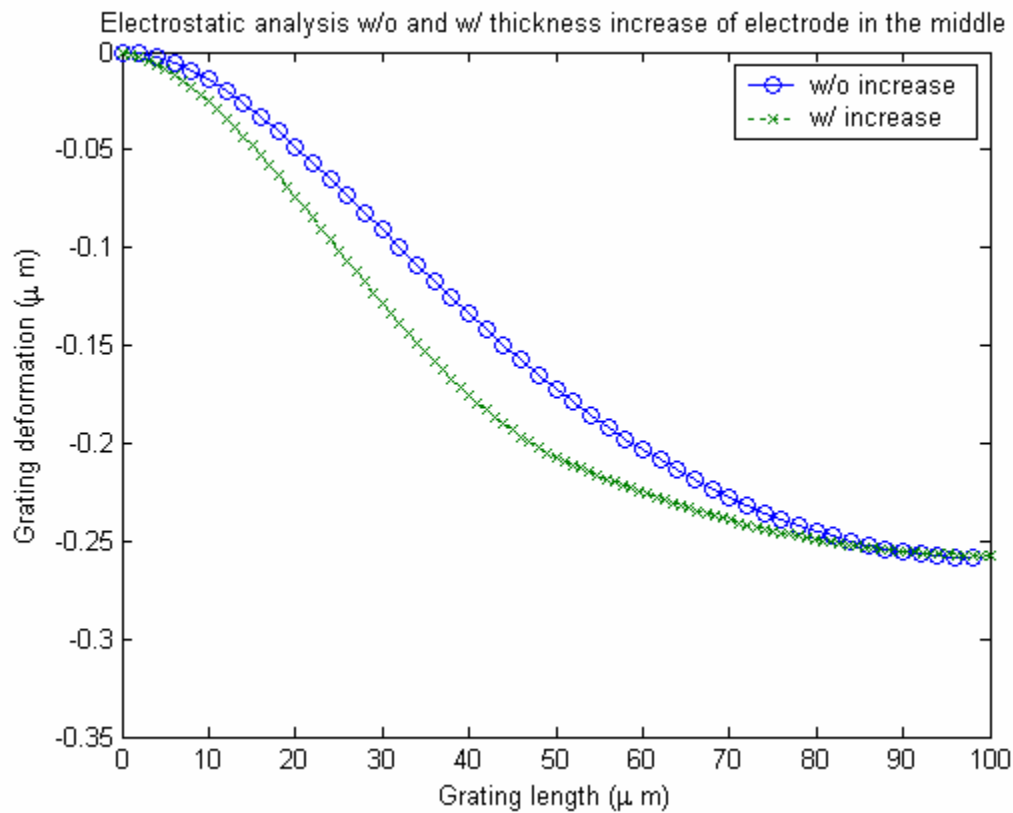


Figure 40. Grating deformation with and without increase of thickness at center

For the more improvement, the grating length was increased from 200 μm to 250 μm . The electrode size (L_e) was reduced 40 μm . L_o was 30 μm to get a margin of 10 μm from the sidewall to the electrode. Figure 41 shows the shape of the changed grating in the FEM analysis result. Figure 42 shows how flatness is further improved if the side beam thickness is decreased from 1 μm to 0.8 μm .

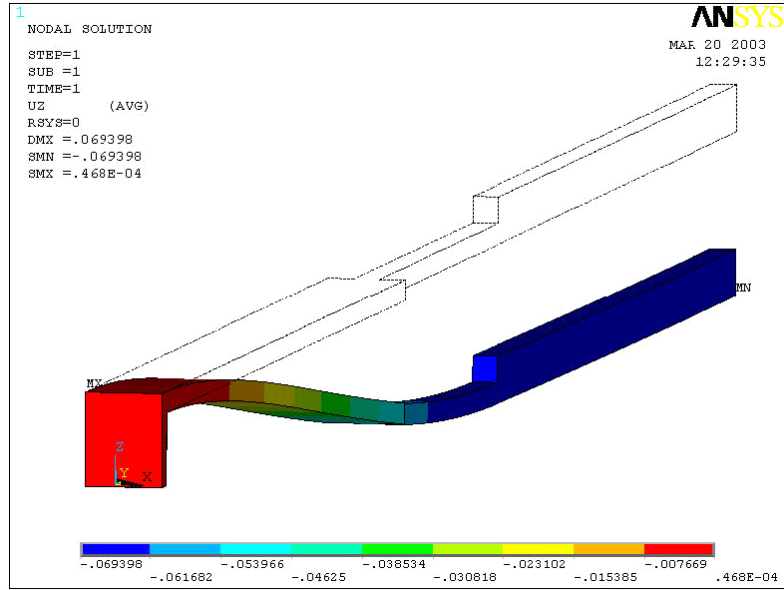


Figure 41. FEM analysis results showing an increased thickness at the beam center

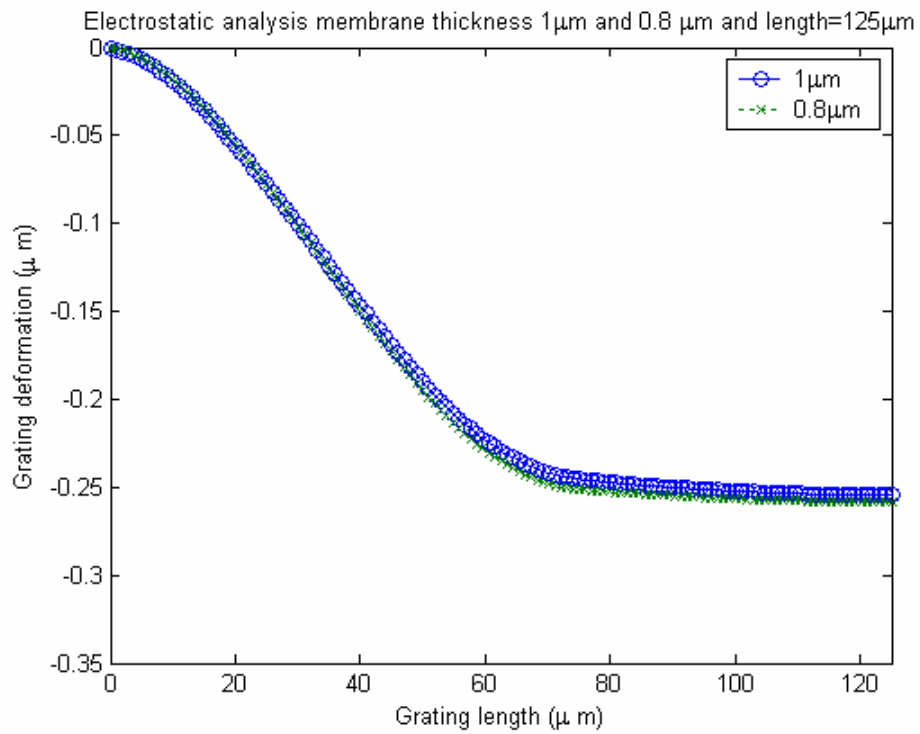


Figure 42. Further improvement by reducing membrane thickness from 1 μm to 0.8 μm

Based on the parameter study using the single beam model, further analysis was performed in a quarter model of the grating membrane as depicted in Figure 43. A quarter model is enough to express the grating membrane since the grating and electrode structure is symmetric quarterly. By applying studied parameters, Figure 44 shows deformation results for 15V for grating period of 3 μm and fill factor of 33%. Side membranes keep the grating from sticking to the bottom substrate during a release process.

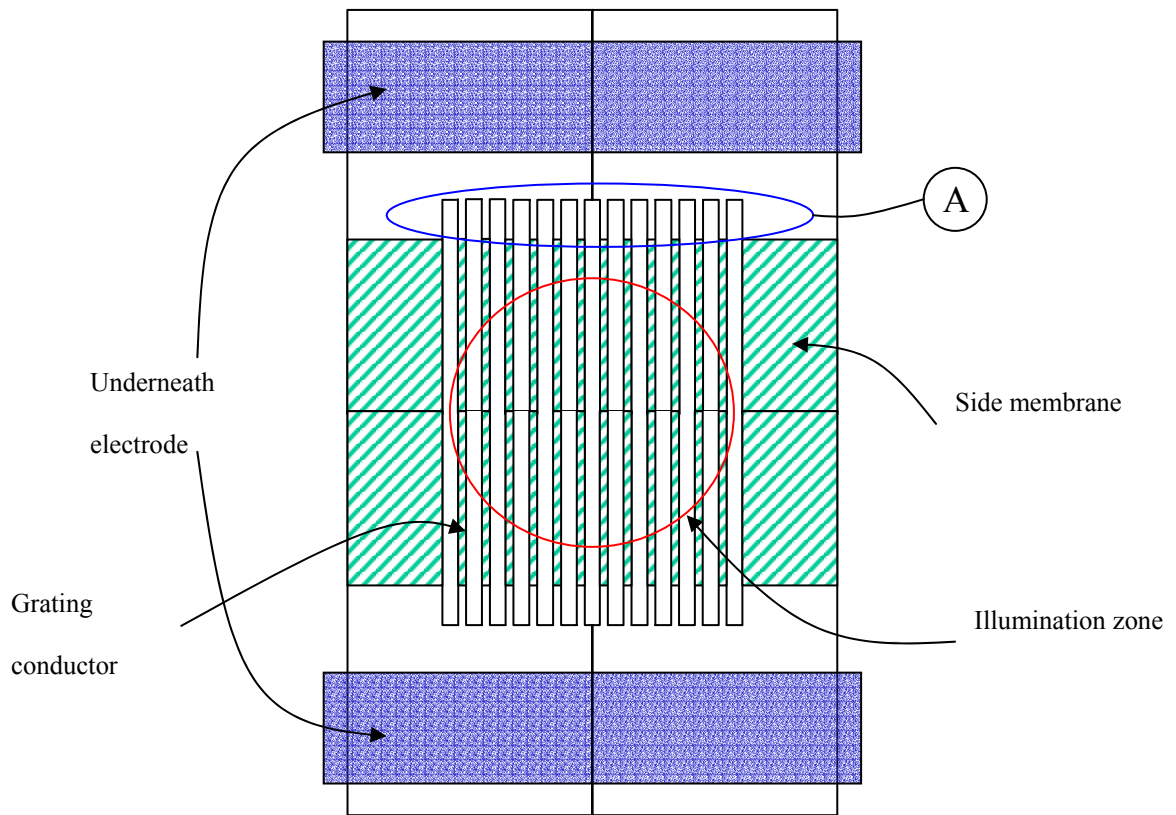
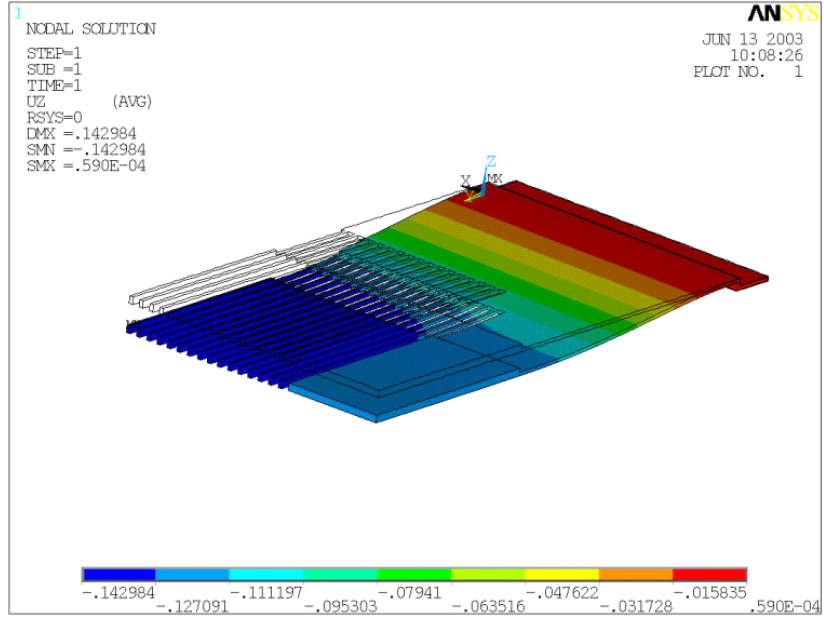
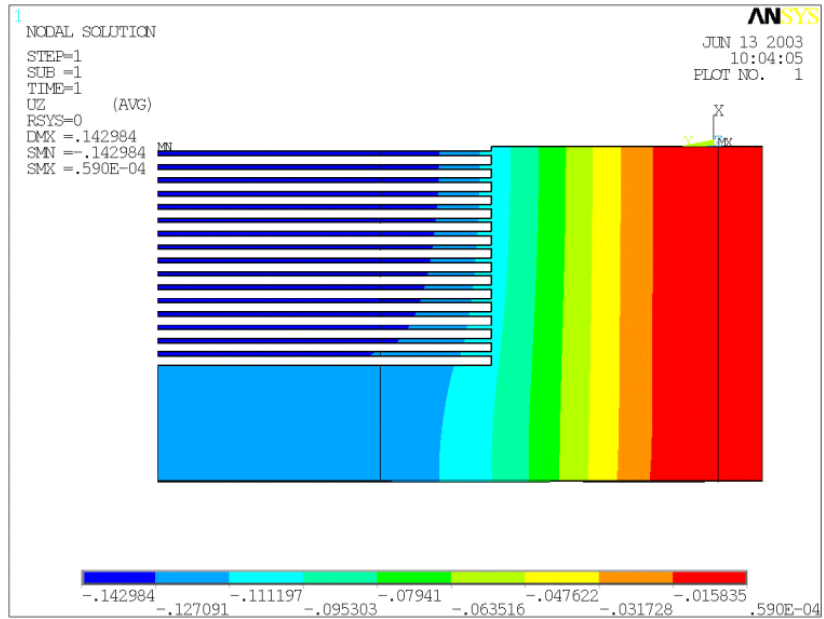


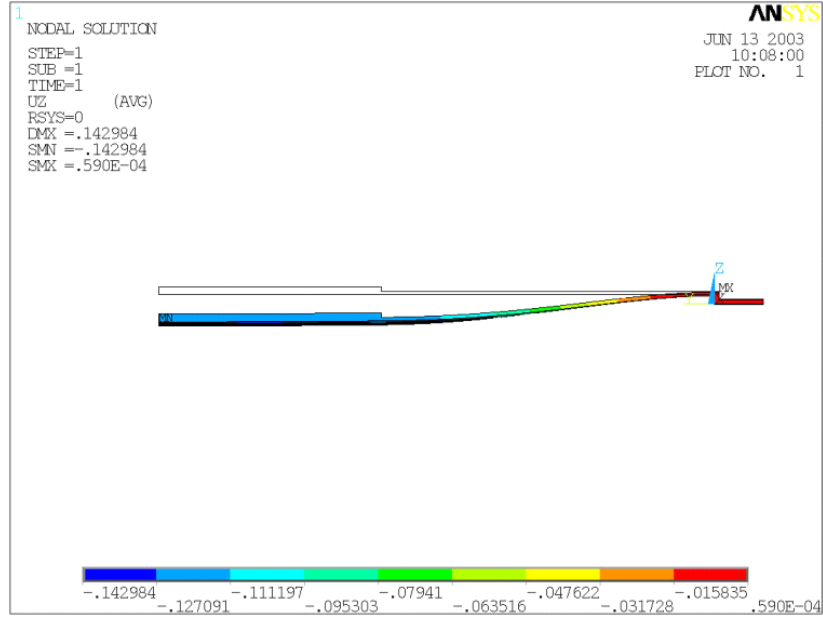
Figure 43. A quarter model of the grating membrane



(a)



(b)



(c)

Figure 44. Vertical deformation contour for 15V voltage in FEM analysis (a) oblique view (b) top view (c) side view

In etching process of grating pattern, $0.8 \mu\text{m}$ thickness of zone A in Figure 43 is overetched during etching of $1.8 \mu\text{m}$ thick part of the membrane. Thus, at worst case, the grating beams are not sustained due to overetched zone A. To avoid this problem, the shape of zone A is modified as seen in Figure 45. By increasing the distance between the gaps at zone A, the diffracted beam from zone A, which is not useful for interferometer, is not reflected to the photo detector location. In addition, the region can sustain overetching process as well. Figure 46 shows grating deformation results for 15V for grating period of $3 \mu\text{m}$ and fill factor of 33%. Figure 47 shows grating deformation results during the actuation. Figure 48 zooms out a flat illumination zone during the same actuation. A theoretical deflection of $0.4 \mu\text{m}$ which exceeds a half wavelength of a HeNe laser ($\lambda = 633 \text{ nm}$) is predicted for 25V DC bias. This is large enough to reach the linear region of maximum sensitivity from any initial path difference as shown in Figure 22.

This design yields a maximum deviation from flatness in the center portion of the membrane of less than 30 nm at 25V DC bias. Figure 49 shows DC bias vs. gap at the center of the grating which is come from Figure 47. Since the electrostatic force is proportion to the square of voltage, the gap is rapidly decreased as the DC bias increases.

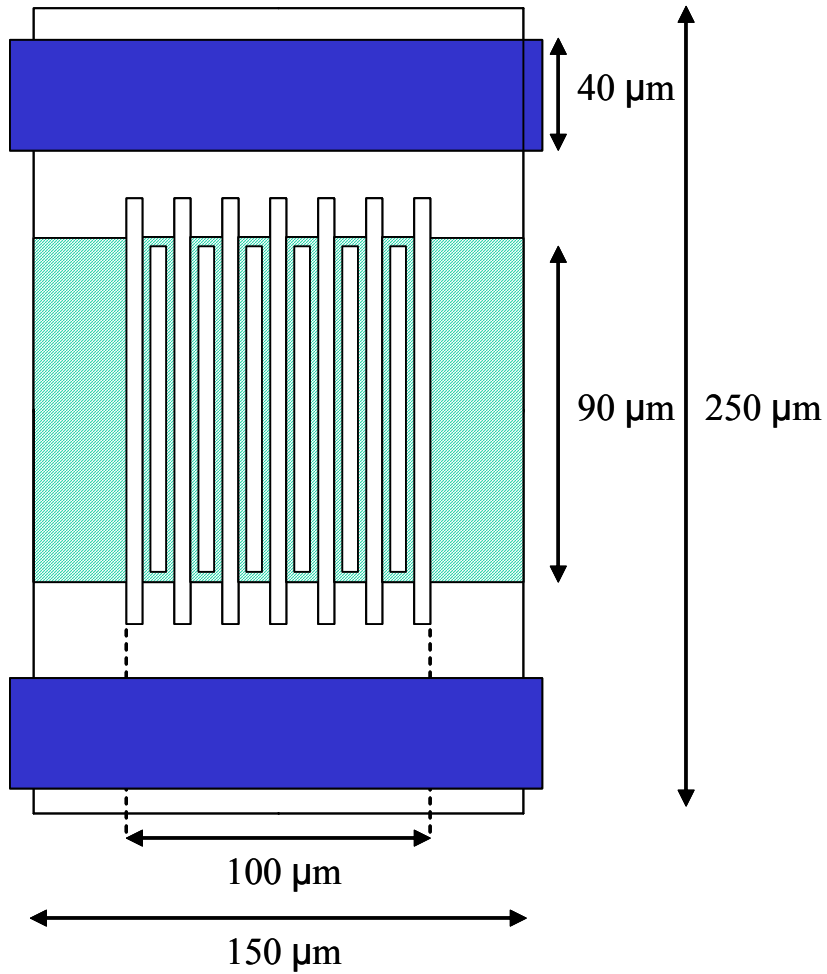
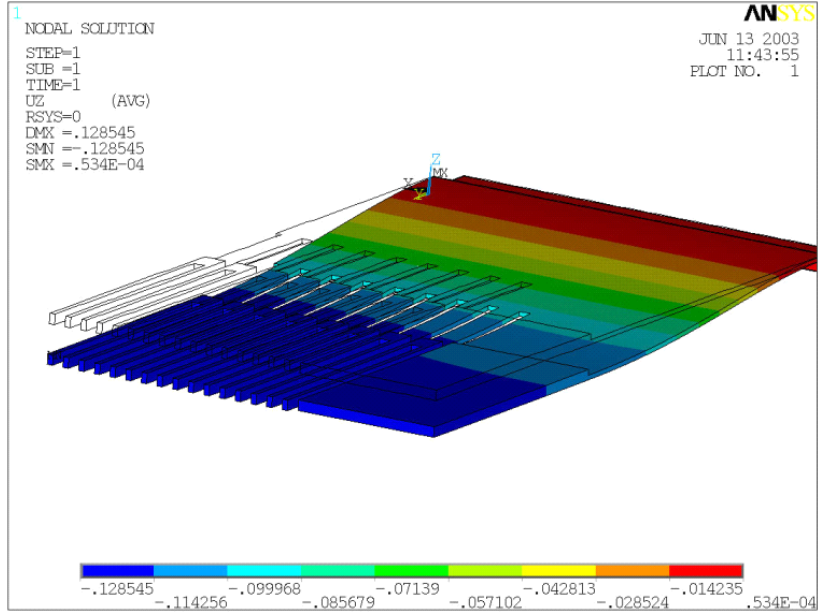
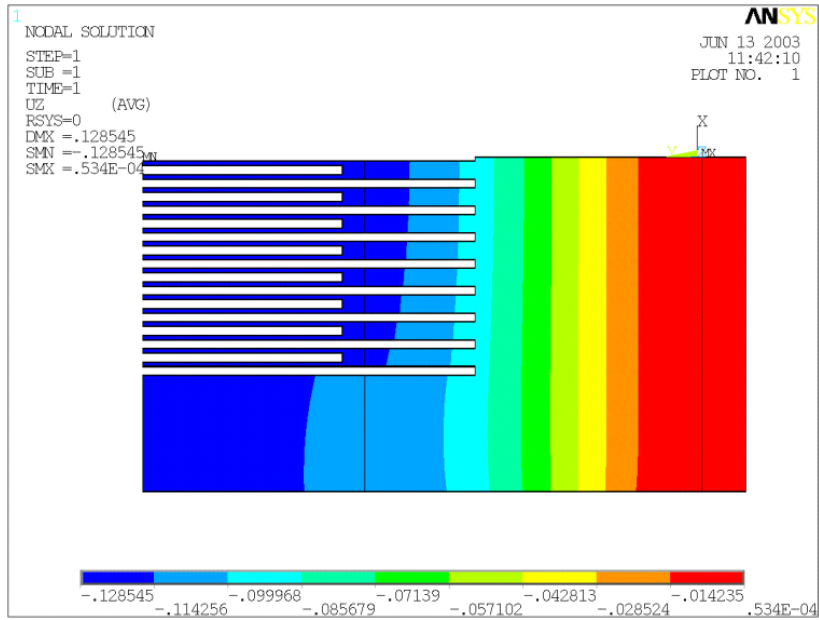


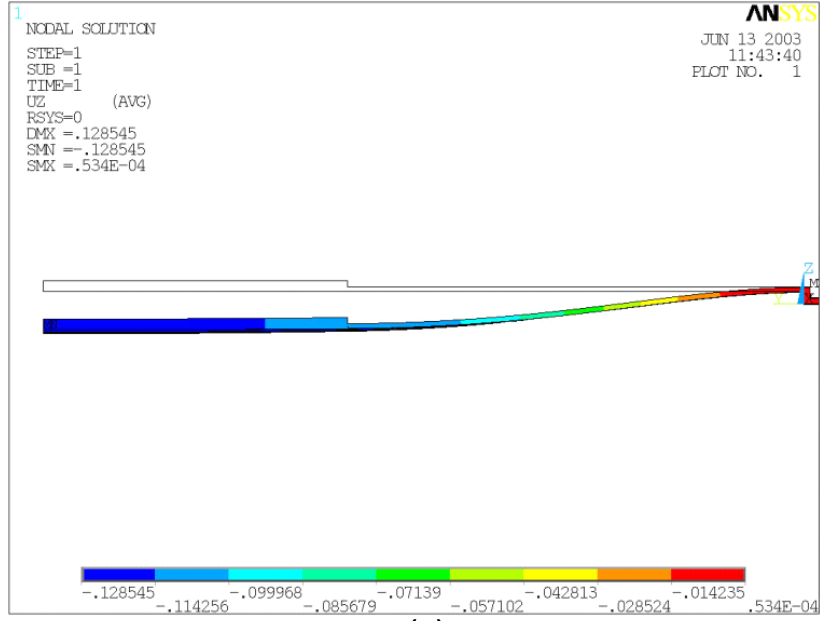
Figure 45. Modified shape of the grating membrane



(a)



(b)



(c)

Figure 46. Vertical deformation contour for 15V voltage in FEM analysis (a) oblique view (b) top view (c) side view

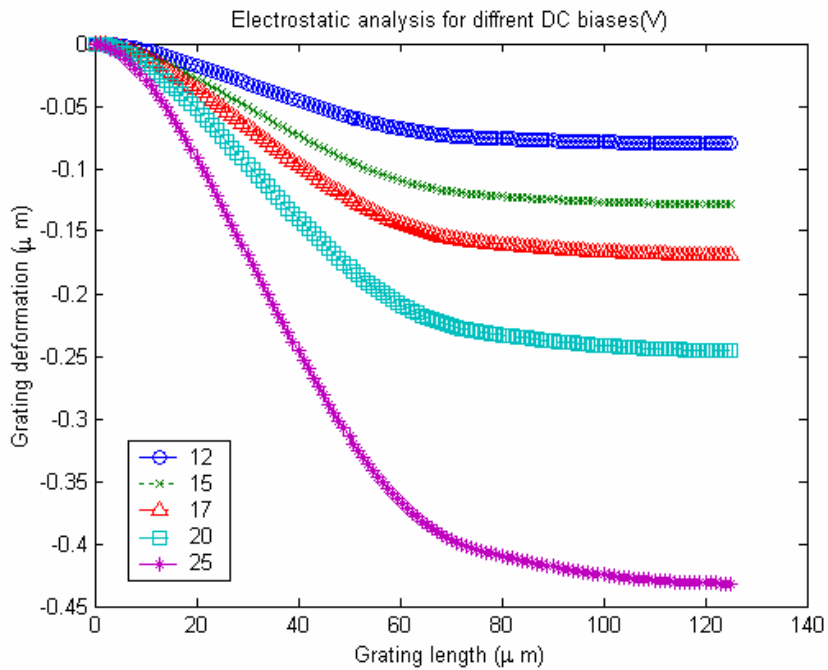


Figure 47. Deformation of the grating during actuation

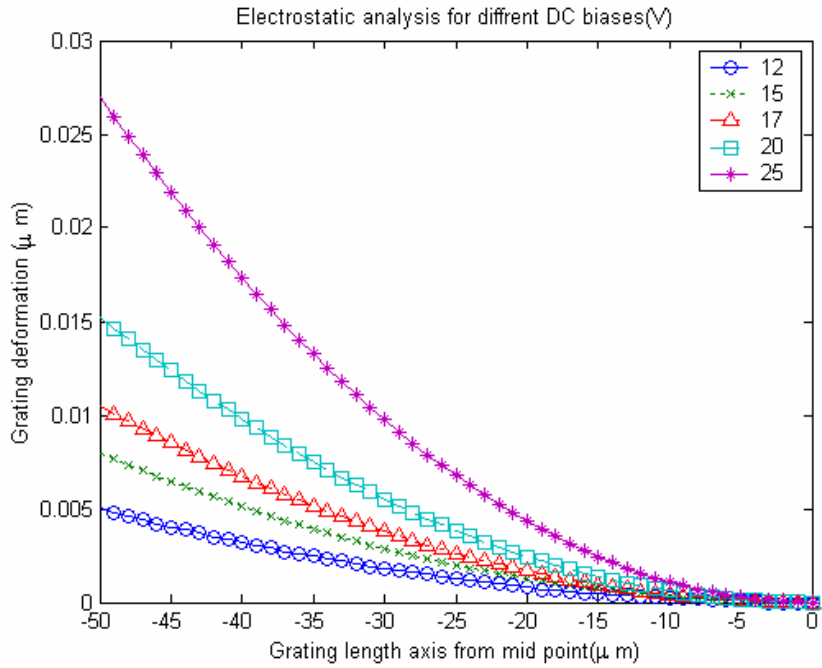


Figure 48. Deformation at the illumination zone during actuation

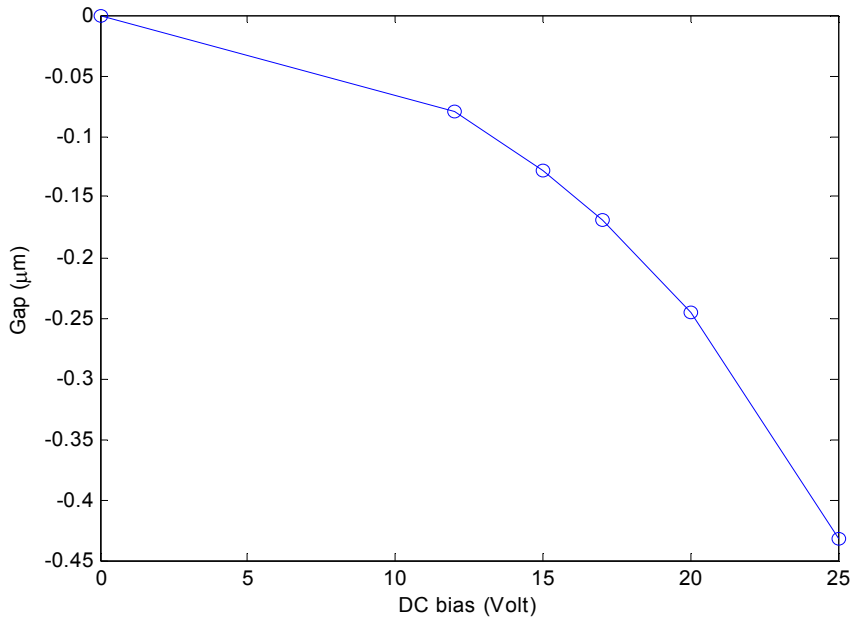


Figure 49. DC bias vs. gap

It is important to insure that the structure of the grating is stiff enough to avoid low frequency mechanical vibration, but not so stiff as to increase the operating voltage

required to pull down the grating. The natural frequency of the grating in the first bending mode is 140 kHz according to the modal analysis performed in ANSYS as shown in Figure 50. If the signal-to-noise ratio at this operating frequency is not sufficient, it is possible to operate the grating at frequencies up to 140 kHz bandwidth achieved for ample range of vibration reduction.

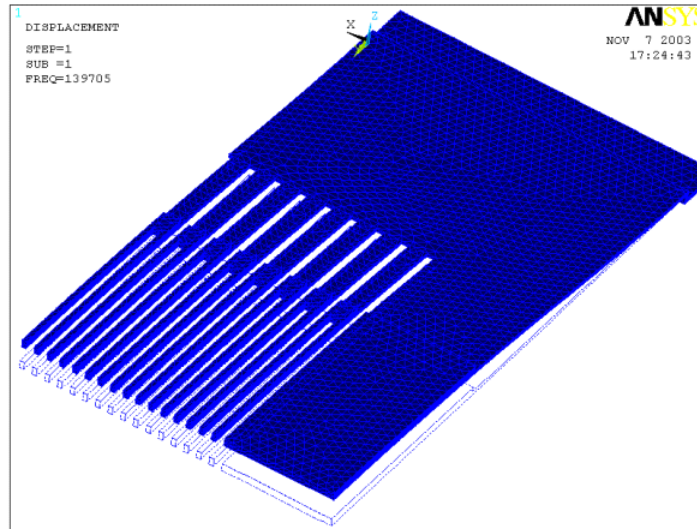


Figure 50. Modal analysis result showing the first bending mode of 140 kHz

3.4 MICROMACHINED SCANNING INTERFEROMETER

In Figure 51, the designed microlens and deformable grating are combined on different side of the same wafer. The photo diode which is fabricated on the Silicon wafer is also integrated with the deformable grating wafer. Depending on the period of grating, Λ and wavelength of the light source, λ , and photo diode location, D_{PD} , the distance from the grating to the photo diode, D_{G-PD} to pick up 1st diffraction order can be calculated as

$$D_{PD} = D_{G-PD} \times \tan \left[\sin^{-1}(\lambda / \Lambda) \right] \quad (14)$$

For example, $\lambda = 0.633\mu\text{m}$, $\Lambda = 4\mu\text{m}$, and $D_{PD} = 250\mu\text{m}$ gives D_{G-PD} about 1.6mm. Considering a two wafer thickness of 0.5mm and photo diode of $300\mu\text{m}$, the size of one μSI excluding light laser diode size fits in a $1 \times 1 \times 3\text{mm}^3$.

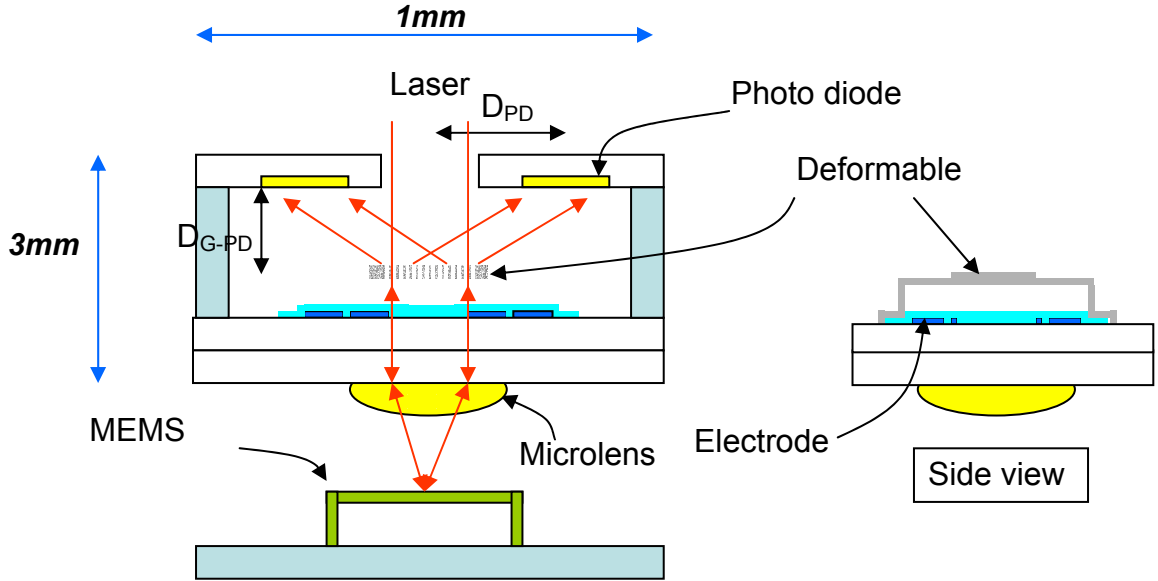


Figure 51. Designed micromachined scanning interferometer (μSI)

3.5 SUMMARY

It is important to design the grating structure with high stiffness for dynamic operation but sufficient enough to avoid a high actuation voltage. By simulation in ANSYS, appropriate dimensions of the grating membrane can be decided. From the simulation, the following constraints are satisfied.

- The voltage for the electrostatic static force was within 50V.

- The working range of grating was larger than a half wavelength.
- The stiffness of the grating membrane gave an enough band width more than 10 kHz.
- The bottom electrode did not block the light source.
- The flat zone at illumination was sufficient to increase diffraction efficiency.

Since the residual stress in the membrane was not a design consideration, any deformation that results from the residual stress in the fabrication processes could cause a different performance. Thus, this deformation should be monitored throughout the processes.

CHAPTER 4

FABRICATION

The designed μ SI shown in Figure 51 need three processes on three different wafers; a microlens, a deformable grating, and a photo diode. Fabrication processes on the microlens and the deformable grating are described in each section in detail. The photo diode which is fabricated at CMOS group of Georgia Tech is introduced in Section 4.3.2. Figure 52 shows again the hybrid type structure of the microlens and the deformable grating integration.

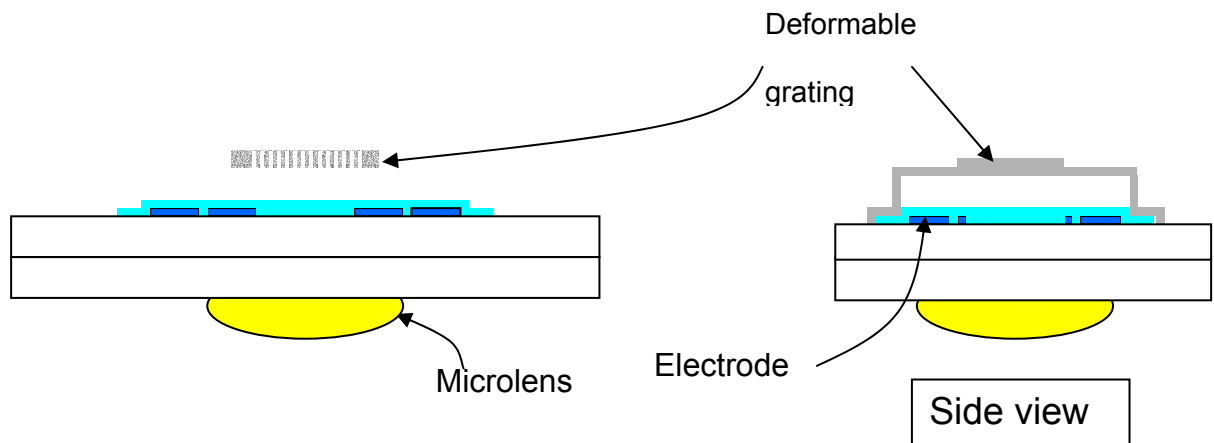


Figure 52. A microlens and a deformable grating

4.1 MICROLENS

4.1.1 PROCESS DEVELOPMENT

The plano-convex lens is fabricated on quartz substrate using a photoresist reflow technique [63]. Generally, the major problem in the microlens fabrication process based on melting of the lens material is the control of spreading. An excellent resist for the spreading of AZ P4620 can address this problem. The Details of the fabrication processing steps for F-number 5 plano-convex lens with 200 μm diameter on quartz substrate are:

- a) Spin AZ P4620 PR at 2000rpm with a ramp of 2500rpm/sec for 30 seconds
- b) Soft bake spun PR at 110°C in oven for 4 minutes
- c) Expose 450mJ of Ultra Violet light into the wafer at Constant intensity 1 mode (355 nm wavelength) with soft contact and 20 μm gap
- d) Develop the wafer in AZ 400K developer (2.5:1=water:developer) for 40 seconds
- e) Anneal the developed PR at 110°C in oven for 15minutes
- f) Cure the PR at 180°C in oven for 20minutes
- g) Turn off the oven and open it for cooling of the cured PR

Figure 53 shows AZ P4620 PR thickness after developing at four different PR spinning speeds on quartz substrate. Since the diameter of the lens pattern is 200 μm , the volume of the PR cylinder can be estimated. For example, 8.5 μm thickness at 2000 rpm gives $2.7 \times 10^5 \mu\text{m}^3$. Figure 54 shows calculated focal lengths of the fabricated

microlenses at four different PR spinning speeds on quartz substrate. The interesting point is that the focal length dropped at 2500 rpm even though the PR thickness of that speed is less than the other speed. It was observed that the lens diameter was reduced only at that case from 200 μm PR cylinder to 165 μm due to over evaporation of the PR in melting process as shown in Figure 55. From this observation, the reduced focal length could be explained. Since the amount of evaporated PR can be controlled or varied by melting temperature and duration time, it is important to keep them constant for each fabrication batch to get consistent results.

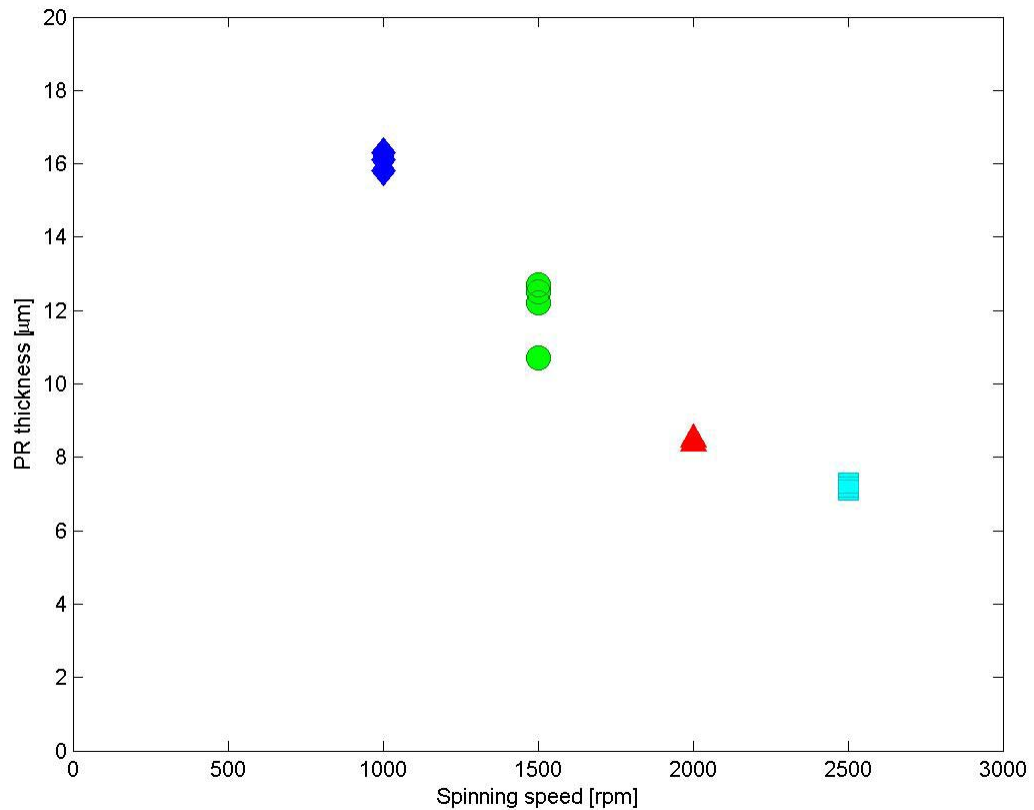


Figure 53. PR thickness vs. PR spinning speed of the fabricated lenses

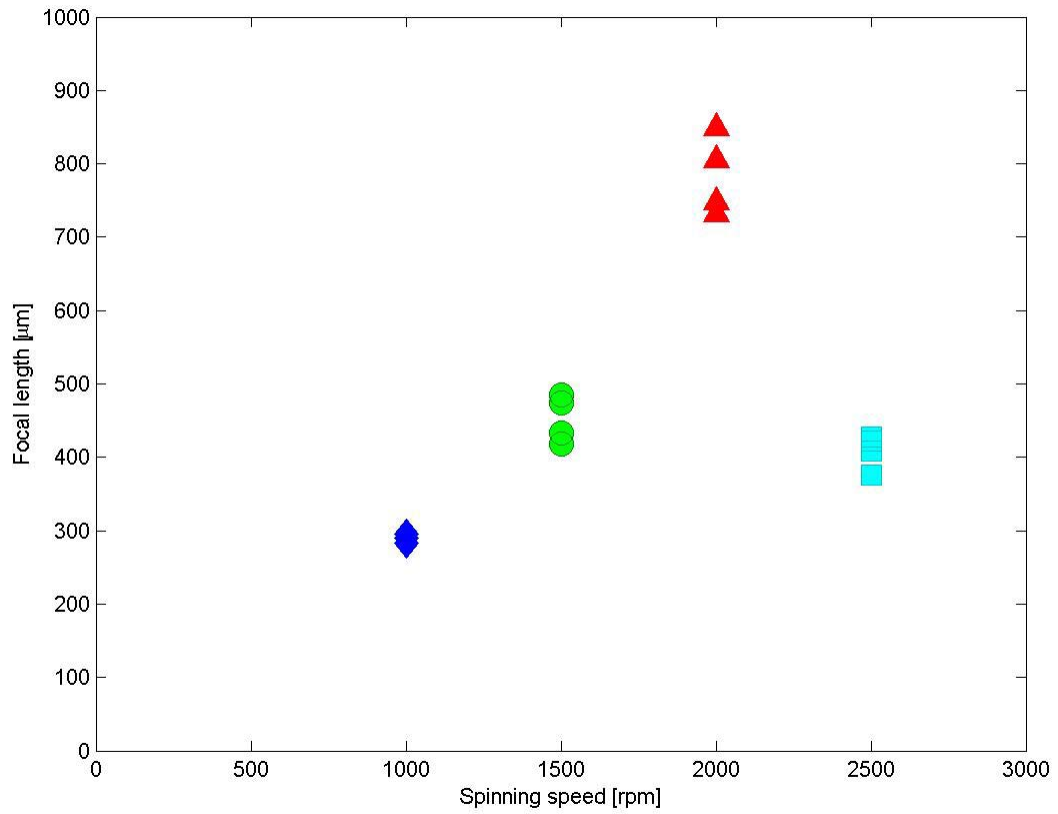


Figure 54. Focal length vs. PR spinning speed of the fabricated lenses

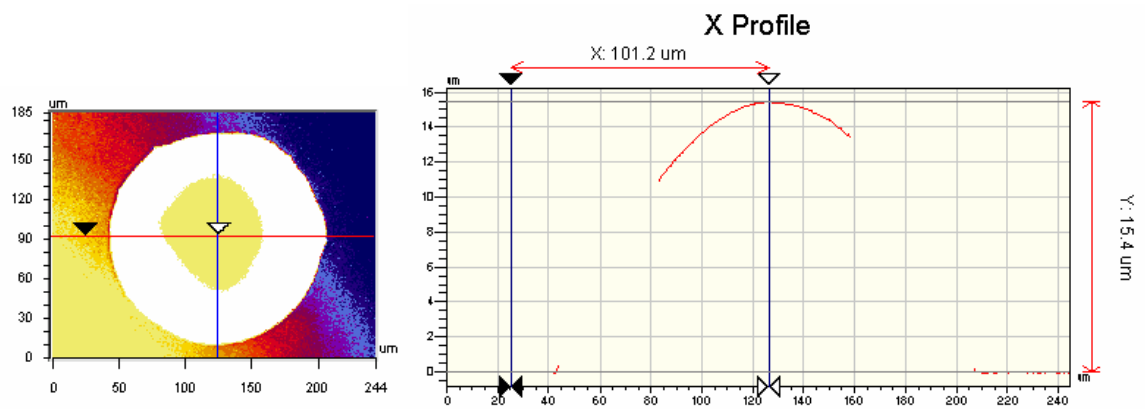


Figure 55. Profile of the fabricated lens that is spun at 2500 rpm

It is also important to adjust a spinning speed of AZ P4620 for the lens fabrication. Depending on the substrate materials, the wetting angle of the melting PR is limited. For example, 200 μm diameter lens with focal length of 1mm can be fabricated on the bare quartz substrate by spinning 2000 rpm for 30 seconds, but this recipe does not work on aluminum aperture. To fabricate 200 μm diameter lens on aluminum or chrome aperture, AZ P4620 needs to be spun at 1000 rpm. Since a spinning speed mainly decides a focal length of the lens, this limited speed gives a focal length of 300 μm for the 200 μm diameter lens on the aluminum aperture. Figure 56 shows focal lengths of the fabricated microlenses at two different PR spinning speeds on aluminum aperture.

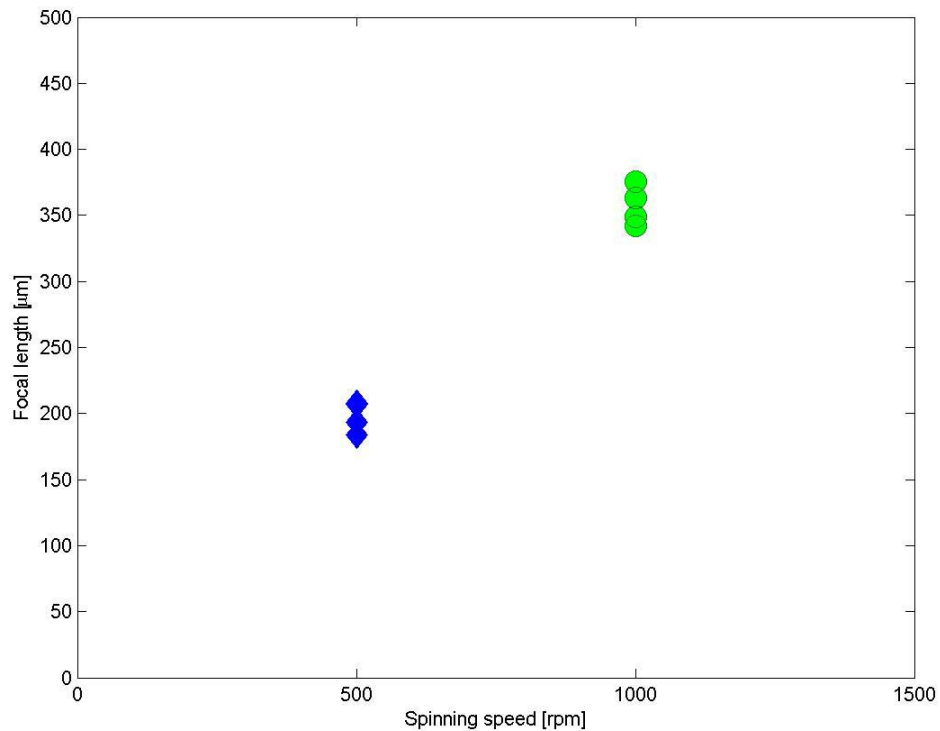


Figure 56. Focal length vs. PR spinning speed of the fabricated lenses on the aperture

4.1.2 CHARACTERIZATION

Figure 57 shows SEM image of the fabricated microlenses. The fabricated microlens have a radius of curvature of $612\ \mu\text{m}$, focal length of $991\ \mu\text{m}$ in paraxial assumption. It has a 0.8% maximum deviation from a sphere. A 30% power loss was observed when HeNe laser beam was passed through the microlens and quartz wafer. It is important that the surface profile of the microlens is close to a sphere. A white light interferometer has been used to measure a surface profile of the fabricated microlens. Since the 3-D measured data can be exported from the white light interferometer [98], it is possible to compare them with a sphere using data fitting software. MetroloGT V1.4 has been used to fit the measured data to closest sphere geometry. MetroloGT V1.4 was developed at Precision Machining Research Consortium (PMRC) group and has been used to fit metrology data to CAD data [99]. Figure 58 shows an example of a measured surface profile of the fabricated microlens and Figure 59 shows its deviation from a fitted sphere of $612\ \mu\text{m}$ diameter using MetroloGT V1.4.

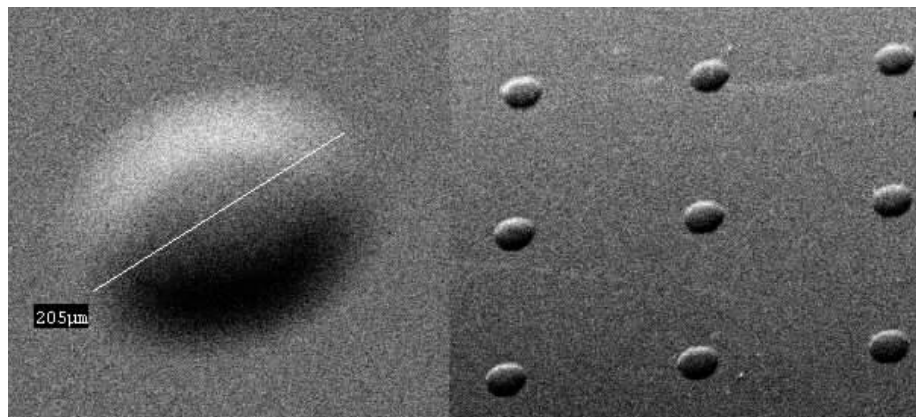


Figure 57. SEM image of the fabricated micro lenses

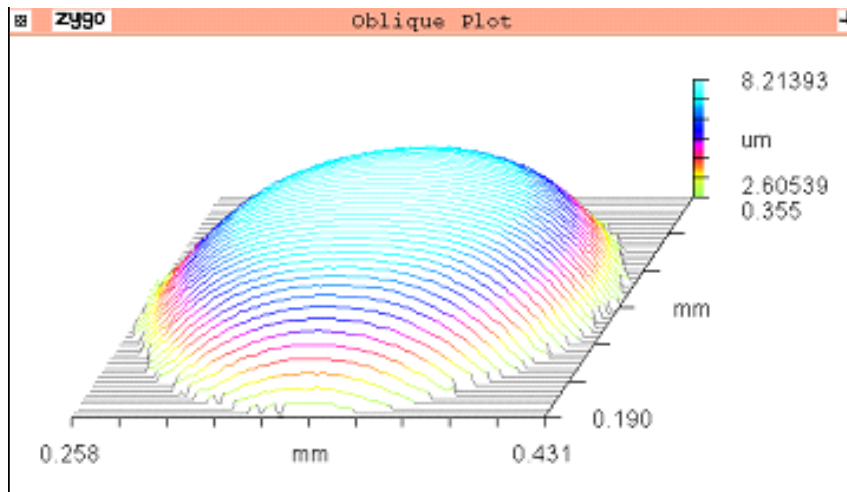


Figure 58. Surface profile of the fabricated microlens

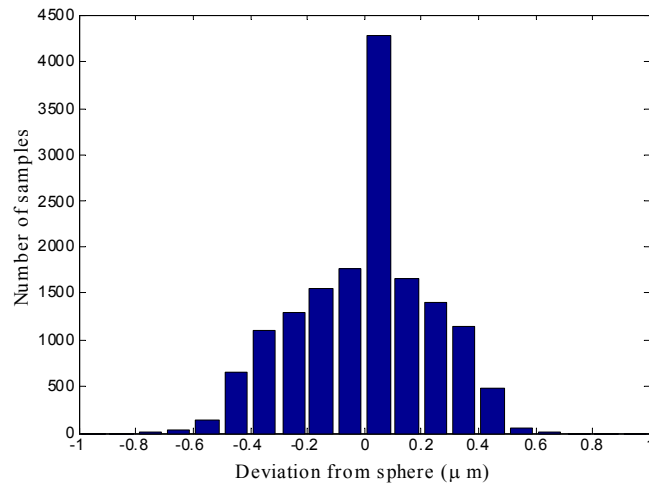


Figure 59. Histogram of deviation of the measured microlens surface profile from a fitted sphere of 612 μm diameter

To demonstrate focusing performance of the fabricated lens, a set-up in Figure 60 was used to get images at the focal plane of the microlens and at the other planes. The fabricated lens has a diameter of 150 μm and the aperture has a diameter of 200 μm. All

images of the lenses in this section are taken by a 20x objective and a CCD camera. Considering the fact that the CCD array is 648x484 and the size of each pixel is a 9 μm square, each image shows $\{[648, 484] \cdot 9 / 20 = 291.6 \mu\text{m}, 217.8 \mu\text{m}\}$ area at the focal plane of microscope objective. Images are sorted from very close to the microlens (scale 0) to far distance (scale 12) in Figure 61. The closest distance is about 0.2 mm and the farthest distance is about 4 mm from the lens surface. It is clear that the lens focuses the incident beam at the scale 8 plane. By setting the scale 0 plane as reference, the other plane's distances are shown in Table 4.

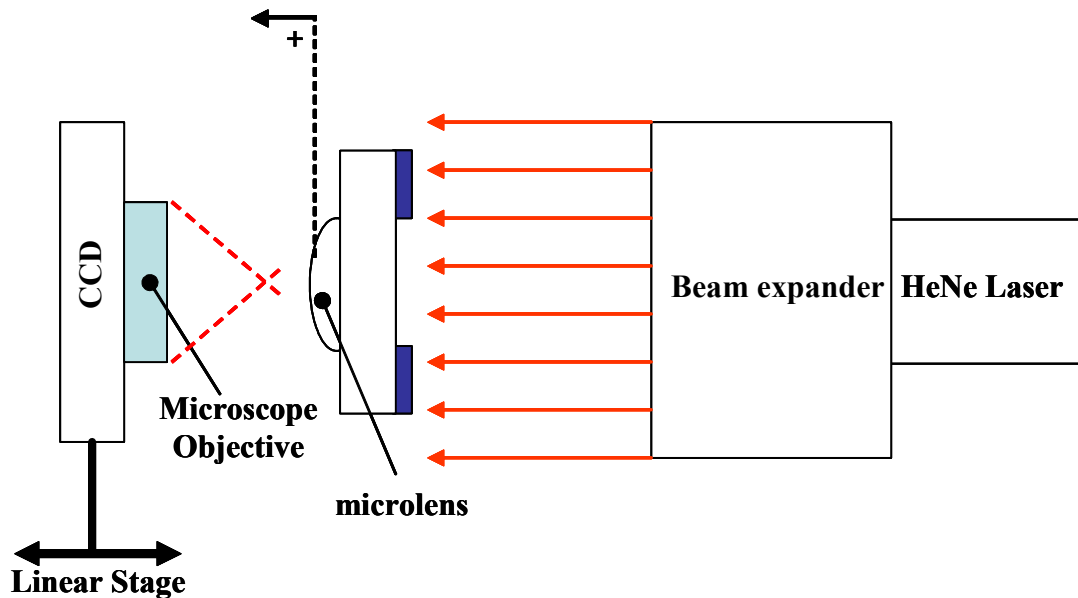


Figure 60. Set-up to measure focusing performance of the microlens

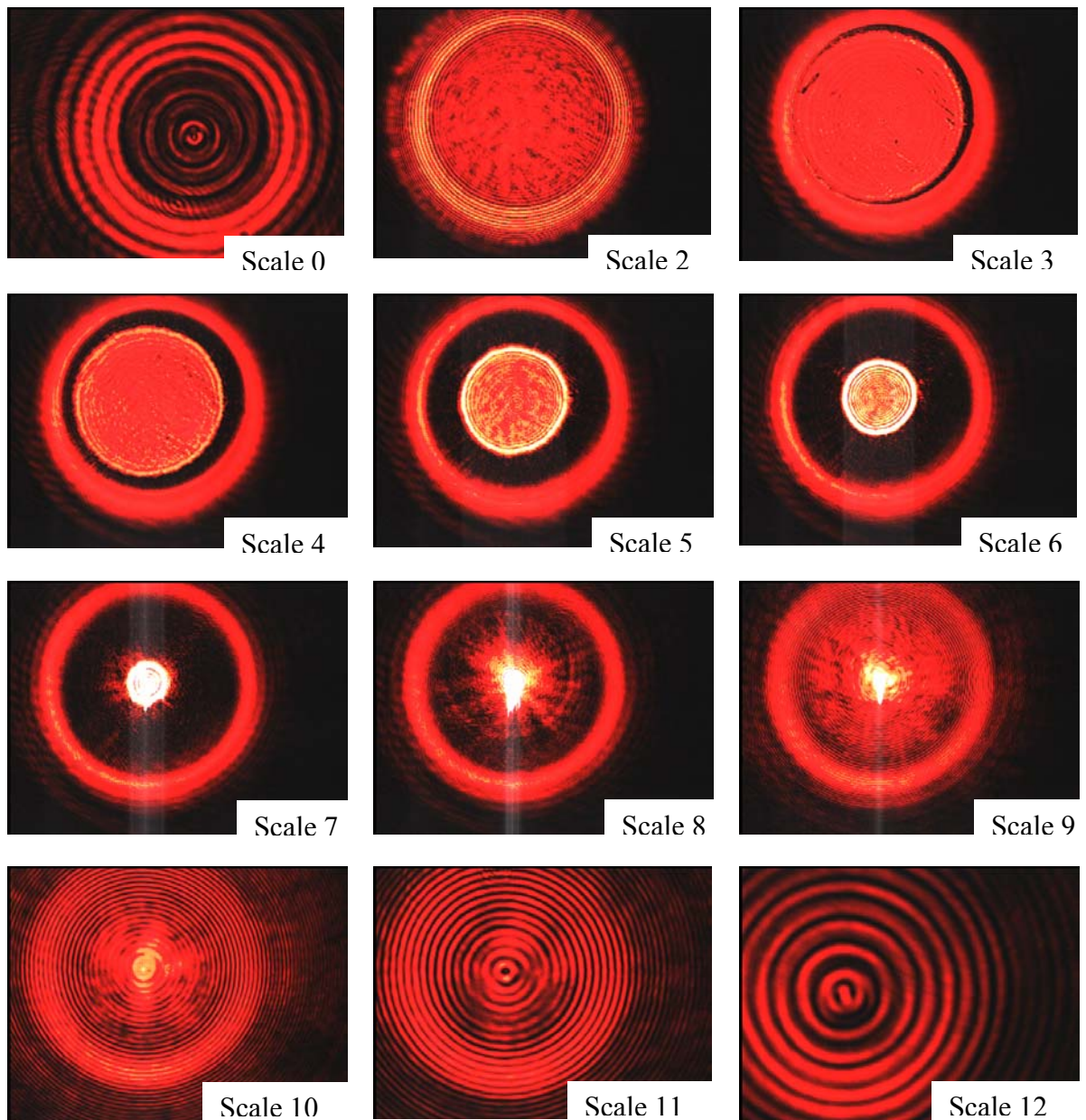


Figure 61. Measured images that come from the microlens and aperture

Table 4. Distances at each plane from the scale 0 plane

Scale	0	2	3	4	5	6	7	8	9	10	11	12
Distance(mm)	0	0.004	0.007	0.014	0.029	0.059	0.118	0.237	0.475	0.95	1.9	3.8

To measure the size of the focused beam, the following experiments are performed. In this experiment a microlens and an aperture were fabricated on the same sides of a quartz wafer. The aperture diameter is 100 μm and the lens diameter is 200 μm . The focal length of the lens is estimated around 330 μm by measuring surface profile of the microlens and using paraxial approximation. Next the CCD is moved away from the lens until the smallest spot size is reached at 270 μm in Figure 62. Hence, the measured focal length is around 270 μm . Since a 100x objective is used in this experiment, Figure 62 shows $\{[648, 484]*9/100 = 58.3 \mu\text{m}, 43.6 \mu\text{m}\}$ area at the focal plane of microscope objective. Furthermore, the spot size at focus is a bit more than 2 μm as full width half maximum (FWHM) as seen in Figure 63. The microlens is further characterized using a step-scan in the next chapter.

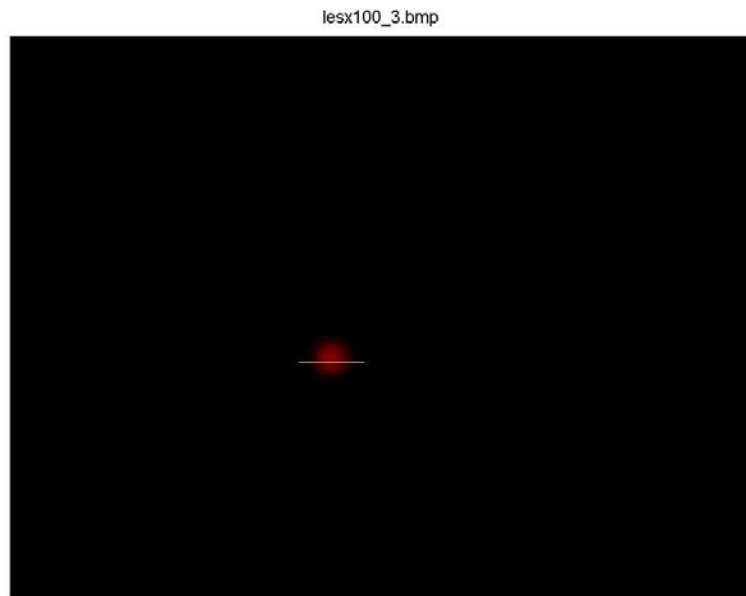


Figure 62. An image at focal plane

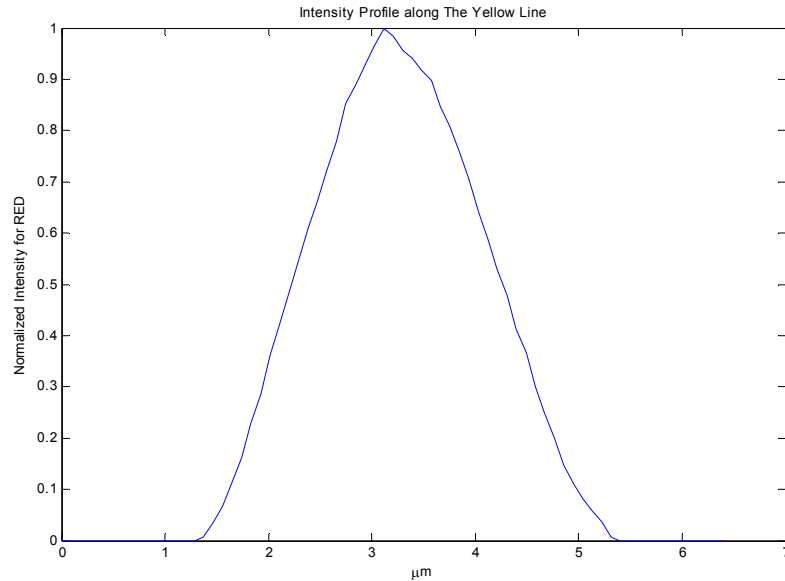


Figure 63. Measured intensity profile at focus

4.2 DEFORMABLE GRATING

4.2.1 PROCESS DEVELOPMENT

The μSI needs a deformable grating to optimize its operation as described in Section 3.3. Aluminum thin film is chosen as the grating material since it has a good mechanical modulus of 40GPa [100] and a good reflectivity of 87% for the visible light [101]. Though its fatigue strength could be a problem for high speed applications such as RF switches, it is appropriate for low speed operation such as required for this application. The fabrication process begins with a bare quartz wafer. The wafer is polished on both

sides by the wafer vendor [102]. To help the adhesion of aluminum to the quartz wafer, 500 Å of Chrome layer was deposited by an electron beam evaporator, then the aluminum bottom electrode shown in Figure 64 is deposited to ~1500 Å thickness and patterned by a lift-off process. A circular aperture of 100 μm diameter is also defined at the center of the rectangular electrode to allow the light source to pass through. A 2400 Å thick PECVD silicon dioxide insulator layer is deposited on the back electrode and patterned by RIE to prevent contact between the bottom electrode and the grating during actuation. Since the quartz wafer is also silicon dioxide, the RIE process also attacks the quartz substrate after etching the top PECVD oxide layer. The PECVD oxide layer was etched with a rate of 98 Å/min and the quartz wafer was etched with a rate of 110 Å/min. To avoid a severe etching of the quartz substrate, RIE process time need to be controlled to etch only the 2400 Å thickness of PECVD oxide. But, it is unavoidable to etch the quartz substrate somewhat without an etch stop layer.

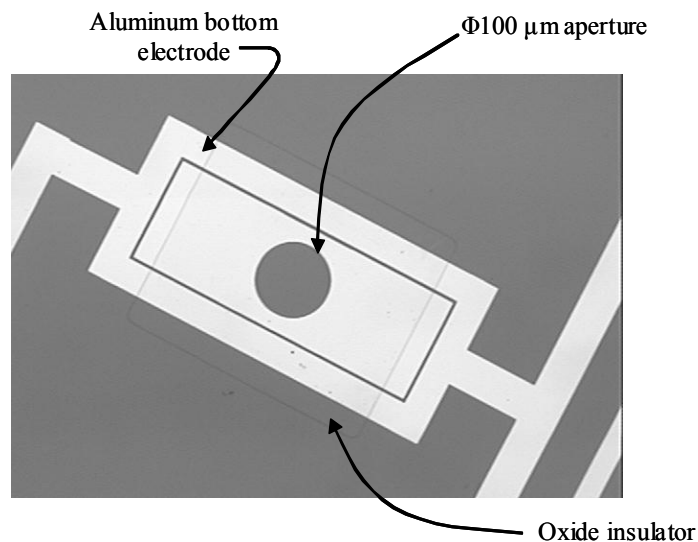


Figure 64. Deposited aluminum electrode and PECVD oxide on the electrode

To create a gap between the two conductors, the bottom electrode and the grating, a 2 μm thick SC 1827 PR is patterned on top of the oxide insulator as a sacrificial layer which is shown in Figure 65. The deposited PR also protects the bottom electrode patterns from on going RIE process to etch the aluminum grating membrane. Since the sacrificial layer should keep its shape during the following processes, a hard bake after developing the PR is required to evaporate remained solvent in PR completely. The developed PR is baked for 25min at 130°C in the oven.

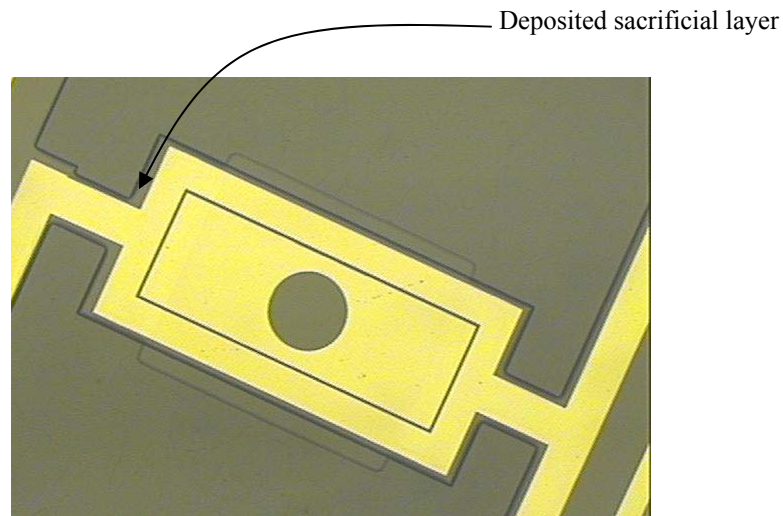


Figure 65. Patterned PR sacrificial layer

On top of the sacrificial layer, a 1.8 μm thickness layer of aluminum is sputtered to create the membrane for the grating shown in Figure 66. Since the bare quartz substrate which is outside of the electrode and the insulator is also etched by RIE, the sputtered layer on that region reveals a rougher surface than the surface on the patterns.

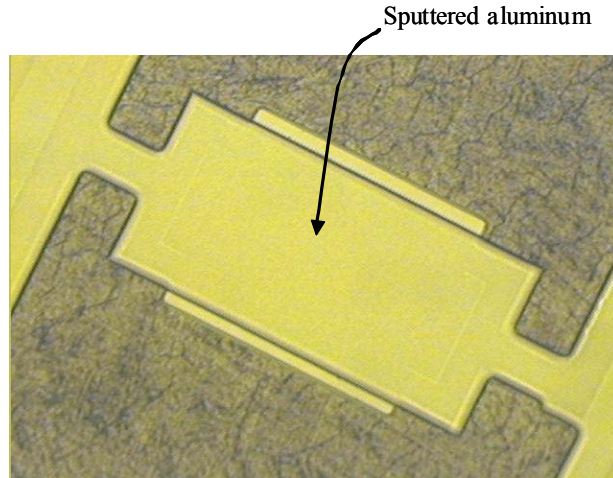


Figure 66. Sputtered aluminum layer on the sacrificial PR

As noted in Section 3.3, the center portion of the grating needs to be stiff for flatness. Therefore, $1\mu\text{m}$ of the aluminum layer except the center region is etched by RIE process as seen in Figure 67. Thus, the PR mask to protect the center region needs to be patterned on the aluminum layer. Since the selectivity of the 1827 PR to the sputtered aluminum in standard aluminum etching RIE process is almost the same, $0.14\mu\text{m}/\text{min}$, a $2.5\mu\text{m}$ thick PR was patterned for $1\mu\text{m}$ aluminum etching. To increase adhesion of PR to the aluminum layer, a Hexamethyldisilazane (HMDS), adhesive promoter was spun first. One thing to point out is that even though the sacrificial PR layer was hard baked, bubbles were formed in the sacrificial layer which was covered with aluminum layer during any process with the temperature exceeding 85°C . Thus, the temperature of any process after aluminum sputtering on the sacrificial layer should be limited to below 85°C . Since the soft baking of the PR needs to be under 85°C , the baking time was elongated to 30min to evaporate the solvent. Also, the hard baking after the developing of the PR is performed at 85°C . Standard aluminum RIE recipe is used with $\text{BCl}_3:40\text{sccm}$, $\text{Cl}_2:10\text{sccm}$,

and CHCl_3 :3sccm at pressure of 30mTorr with a power of 125W for 6min 30sec. An SEM of an etched area indicates about 1 μm isotropic etched shape as shown in Figure 68. Since the RIE equipment in MIRC cleanroom at Georgia Tech showed an inconsistent etching rate and non-uniformity, the etch rate was different on different region even on the same wafer.

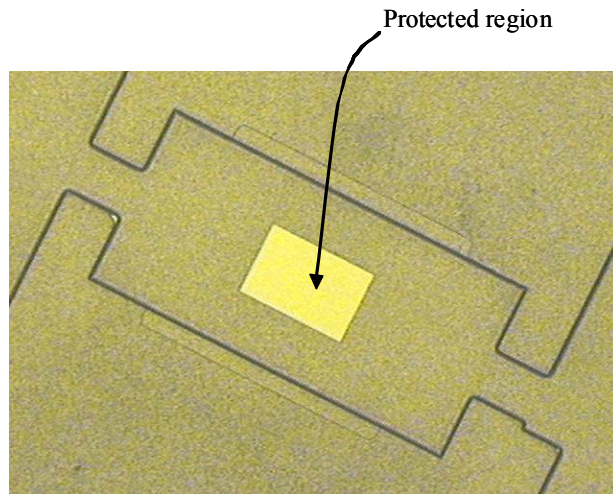
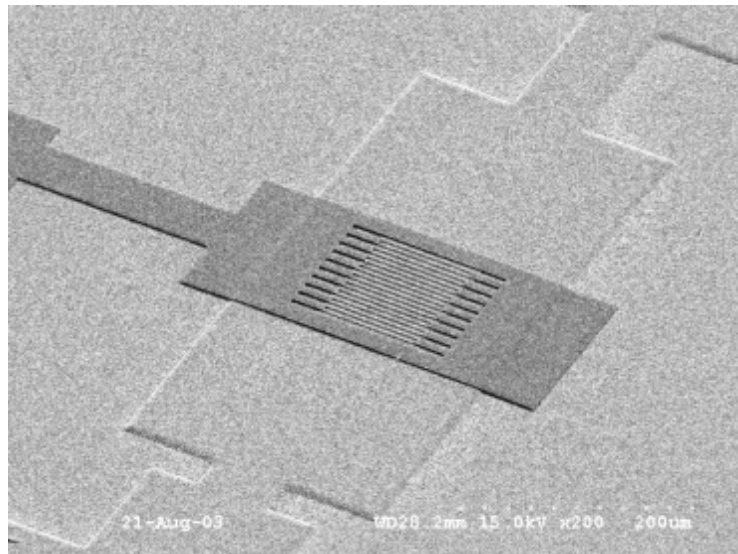


Figure 67. Defined center region by RIE process

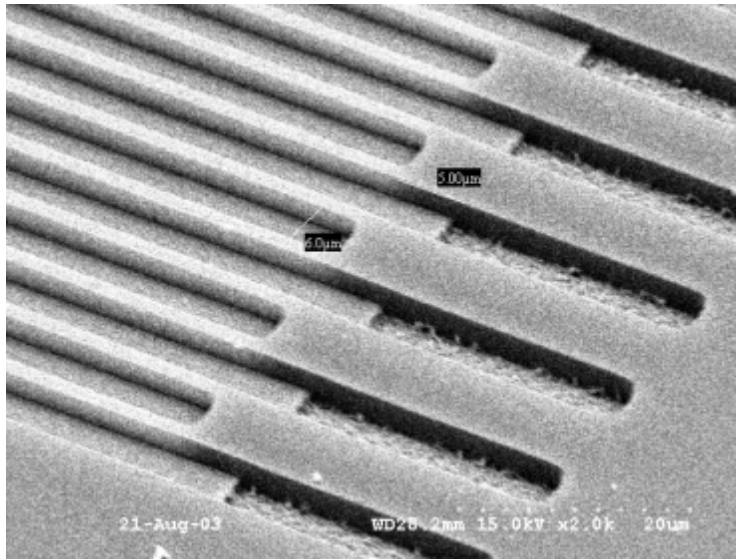


Figure 68. SEM picture showing etched shape by standard aluminum RIE process

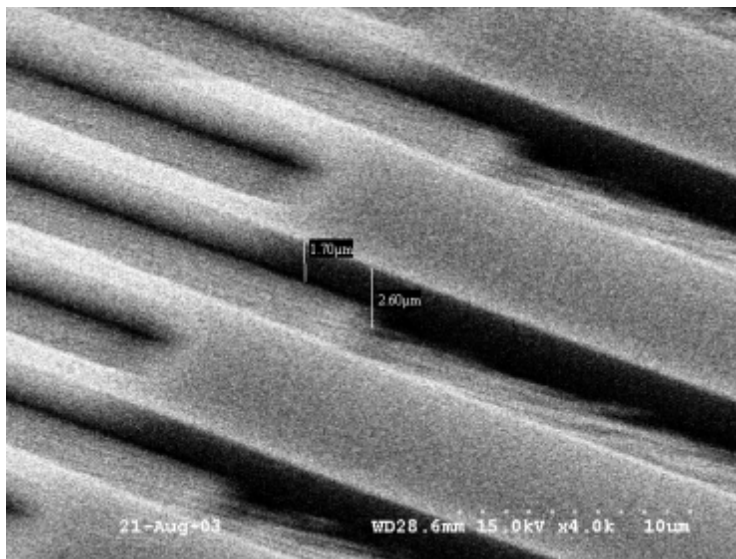
The grating pattern is defined by another RIE process. The grating patterns are very fine. The finest one has a $1.5\ \mu\text{m}$ width and a $100\ \mu\text{m}$ length. Figure 69 (a) and (b) show SEM pictures of the 1827 PR pattern for the grating with $2\ \mu\text{m}$ width of grating and $4\ \mu\text{m}$ width of hole. The RIE etched regions shows a relatively rough surface. It is also seen that PR thickness changes on the thick center edge region in Figure 69 (c). The optimization of lithography parameters is required to define the fine grating pattern. It is important to point out that developing time should be minimized since the MF-319 developer has Tetramethylammonium Hydroxide (TMAH) which can etch the aluminum membrane. Figure 69 (d) shows an aluminum membrane where a developed PR pattern on top of the membrane is removed by acetone. It is clear that the unprotected aluminum membrane is etched during the developing process for the grating PR patterning.



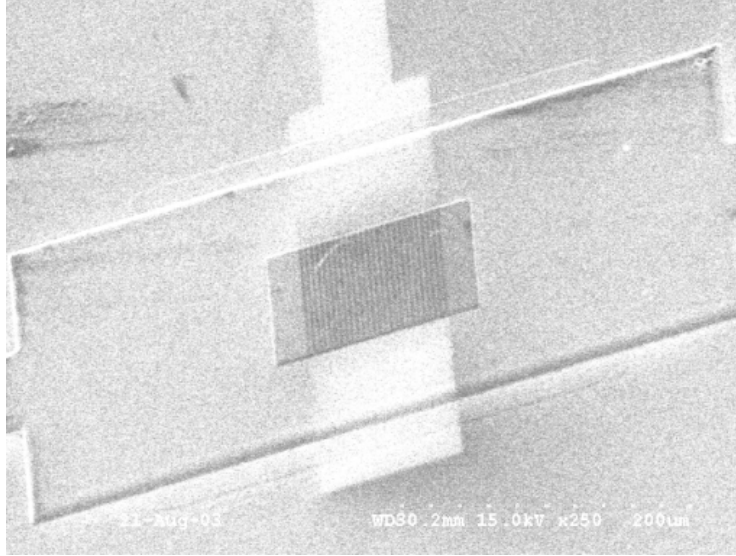
(a) Grating PR pattern on top of thick aluminum membrane



(b) Grating PR pattern showing 6 μm period of grating



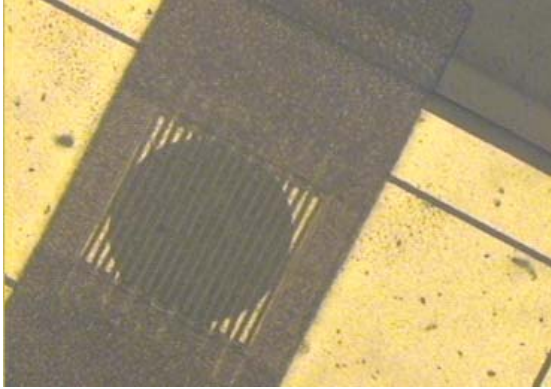
(c) PR pattern showing different PR thickness at the edge of thick region



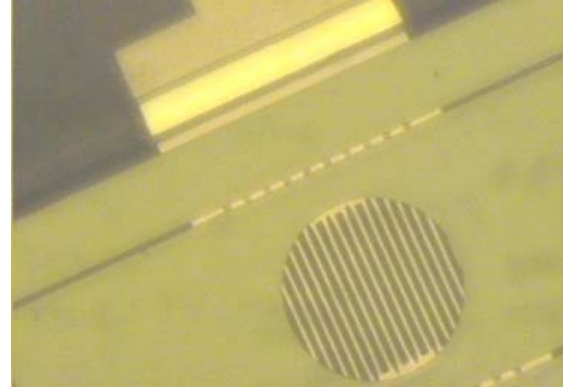
(d) Etched aluminum membrane by TMAH in the MF-319 developer

Figure 69. SEM pictures of grating PR pattern

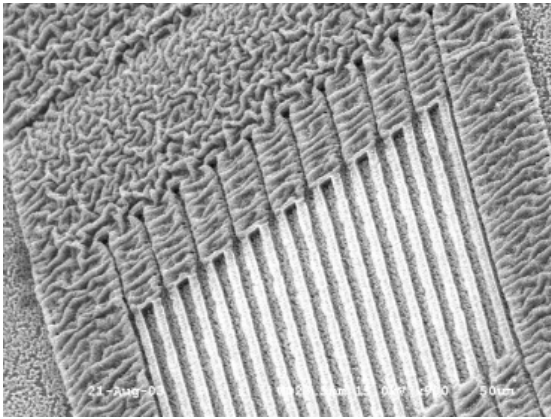
Since the RIE equipment in MIRC cleanroom showed an inconsistent etch rate and non-uniformity, the grating PR patterned wafer was diced to 9 pieces to be etched in different time. This increases process yield. The patterned PR was etched in the RIE chamber for 4 minutes 30 seconds at 10mTorr pressure and 300W power. The gases and their flow rates in the chamber were BCl_3 at 40sccm, Cl_2 at 10sccm, CHCl_3 at 3sccm. Anisotropic etching of the fine grating on the stepped membrane is a challenge. Acceptable anisotropic etching was performed at a pressure of 10mTorr and a high power of 300W during the RIE process. The pressure lower than 10 mTorr gave a nonuniform etch as well as inconsistent etch rate. Figure 70 (a) and (b) show top and bottom view of etched membrane. The bottom aperture and grating beams are clearly seen. Figure 70 shows that the ions attacked the PR mask and produced grooved surfaces on it.



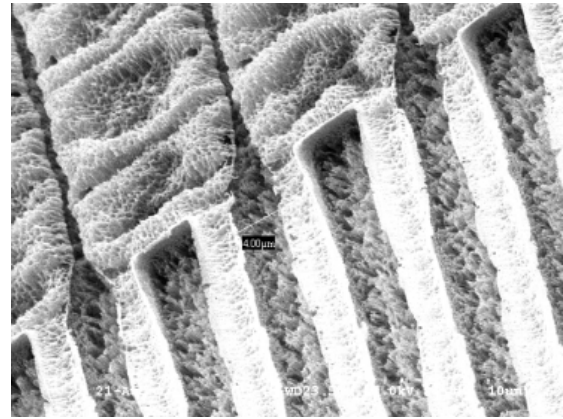
(a) Top view



(b) Bottom view



(c) Attacked PR mask



(d) Attacked PR mask-close-up

Figure 70. Etched grating

To remove the sacrificial layer, the wafer was left in the Shipley Microposit 1165A PR remover at 70 °C for five days. The soaked wafer was evaporated at a super critical dryer to avoid stiction between the grating and the insulator during the release process. Figure 71 shows a SEM of the fabricated deformable grating. The soaking temperature and RIE process temperature might cause the membrane to bow after release. Figure 72 shows the deformation of one released device. Since the fabricated membrane

sagged down after the release, the gap was $0.54\ \mu\text{m}$ which is less than the designed gap of $1.8\ \mu\text{m}$. However, the fabricated grating still has an adequate working range for this application as discussed in the next section. The deformable grating processes are summarized in Figure 73.

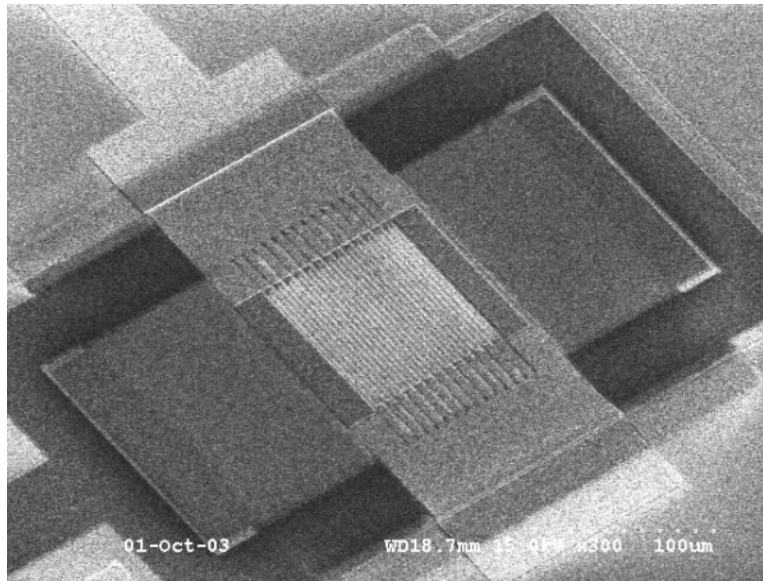


Figure 71. Released grating pattern

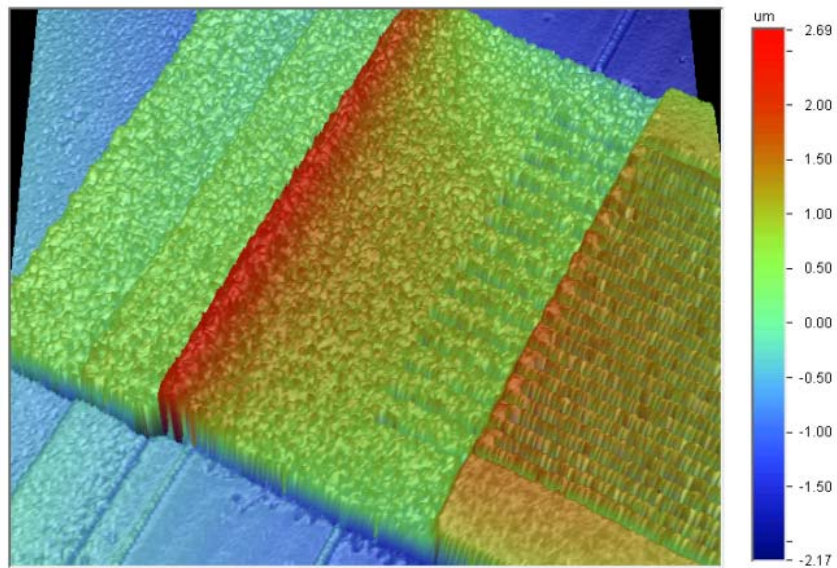
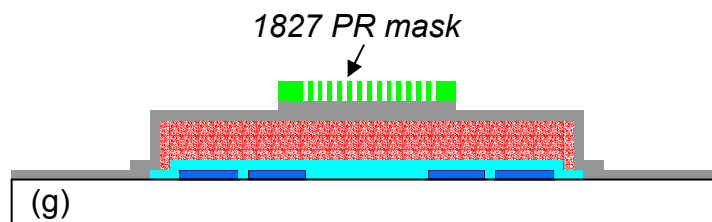
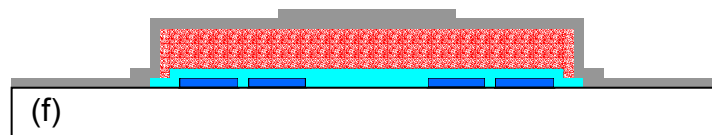
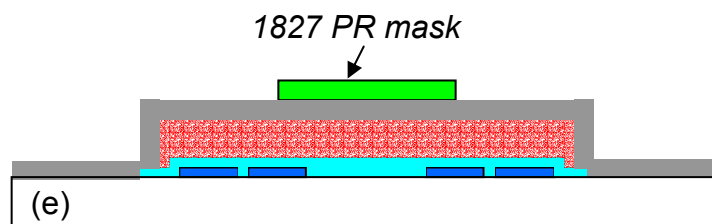
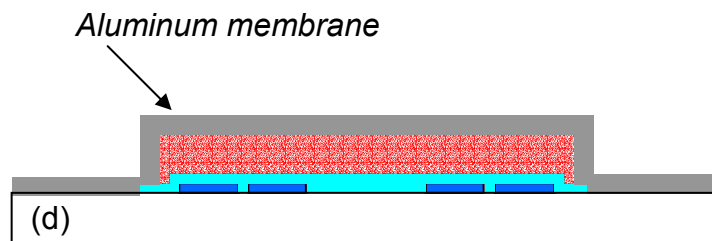
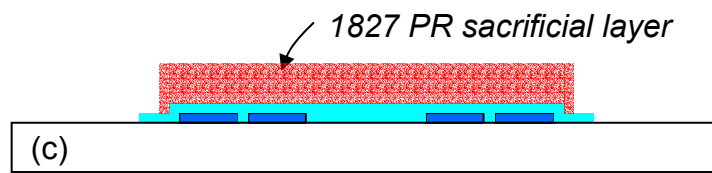
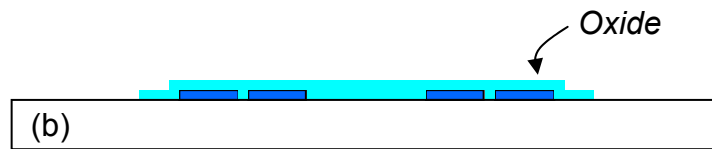
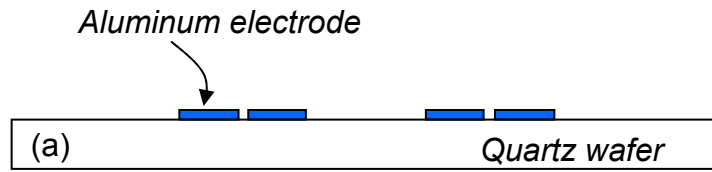


Figure 72. Measure profile of the released grating membrane



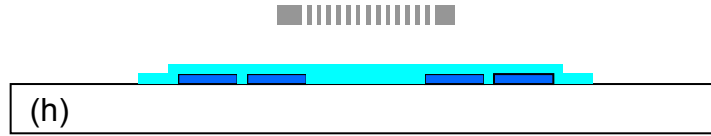


Figure 73. Deformable grating fabrication processes

4.2.2 CHARACTERIZATION

Figure 74 shows profiles of the top of the grating at 0V and 27V DC bias. The membrane at the center was pulled down 0.35 μm from at 27V bias as shown in Figure 74 (e) and (f) and 0.6 μm at pull-in voltage, 31V. The parallel profiles show that grating maintains a level of the surface flatness even at 27V. The transverse profiles show that each grating has the same gap distance in these bias levels. Figure 75 shows measured gap between the bottom oxide layer and the grating at different bias level by optical profilometer. Since the gap is measured from the very fine grating surface, there is a fluctuation in the measurement. Therefore, at certain bias, the gap looks increased even though the bias increases. Though the gap can not be measured directly by the optical profilometer from the top, it can be estimated from the difference in height between the grating at each bias level and at completely pull-in bias of 31V. An equation is fit to the data to convert the DC bias (Volt) to the gap distance (μm). This conversion is necessary to observe the interference signal from the PD as the gap changes. The equation is

$$Gap = -10^{-5}(2Bias^3 - 15Bias^2 + 26Bias - 54486) \quad (15)$$

The fitting curve shows that the gap is decreased rapidly as the bias increases as expected in Figure 49.

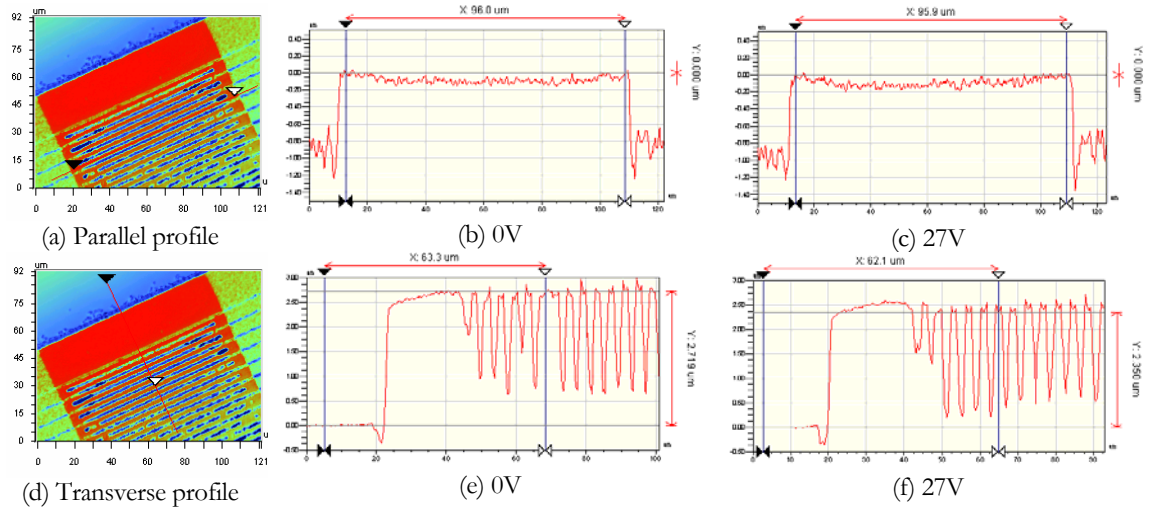


Figure 74. Grating surface profile at 0V and 27V DC bias by optical profilometer

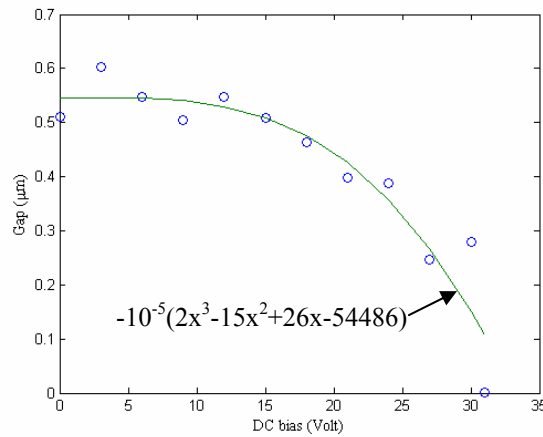


Figure 75. Gap measurement at different DC bias levels

Before the integration of the deformable grating with electronics, the actuation performance of the fabricated deformable grating was measured using the set-up in Figure 76. By measuring the intensity of the first diffraction order while the grating was

under actuation, the vibration amplitude can be inferred. This intensity was plotted in Figure 77 at $16\text{V (DC)} \pm 10\text{V (AC)}$ of a 1 kHz triangular wave. Figure 78 shows the intensity vs. gap distance using the curve fit from Figure 75. Since this experiment data was collected with HeNe laser ($\lambda=633\text{ nm}$), a little less than a half wave length is expected with a gap change of $0.25\text{ }\mu\text{m}$. At around $0.34\text{ }\mu\text{m}$ (25V bias) or $0.44\text{ }\mu\text{m}$ (21V bias) of gap distance, the intensity has the most sensitive response. These points signify the region where the displacement is maintained by the controller to optimize the measurement. More details are discussed in Section 5.6. Figure 79 shows AC ($\pm 0.5\text{V}$) response at certain DC bias at Figure 77. They clearly show that the most sensitive points such as 21V and 25V give the highest magnitude in AC response. This is why the lock-in at these points is necessary during a scanning of the MEMS. Note that the signals at 21V and 25V are 180° out of phase since the slope in DC sweep is negative at 21V and positive at 25V. Figure 80 shows the measured frequency response of the deformable grating in the air using AC sweeping. The actuation band width of the grating is 20 kHz. This value is less than expected bandwidth of 140 kHz in analysis. It is thought that the damping effect in the air and membrane stiffness change in fabrication attribute the decrease of the bandwidth. This kind of air damping effect on the bandwidth is discussed by Yang *et al.* [103].

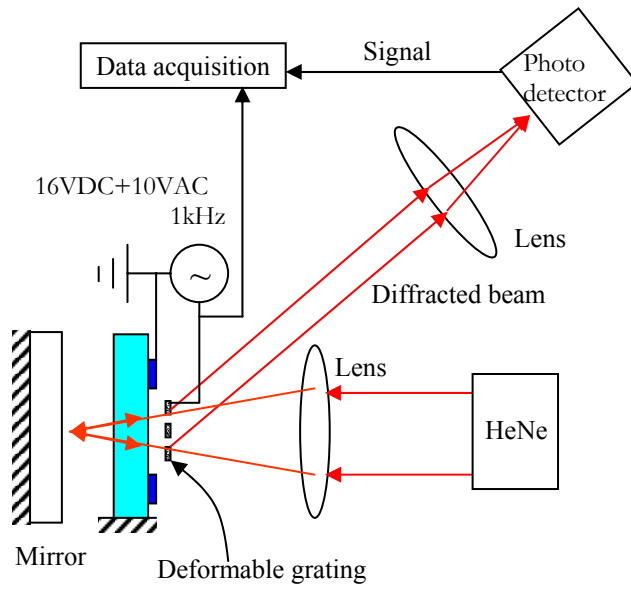


Figure 76. Set-up for deformable grating test

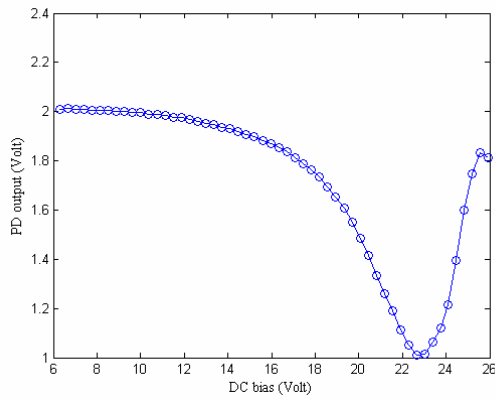


Figure 77. Measured PD output as a function of DC bias

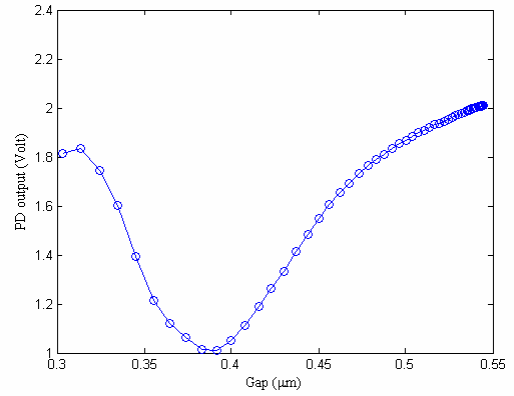


Figure 78. Measured PD output as a function of gap

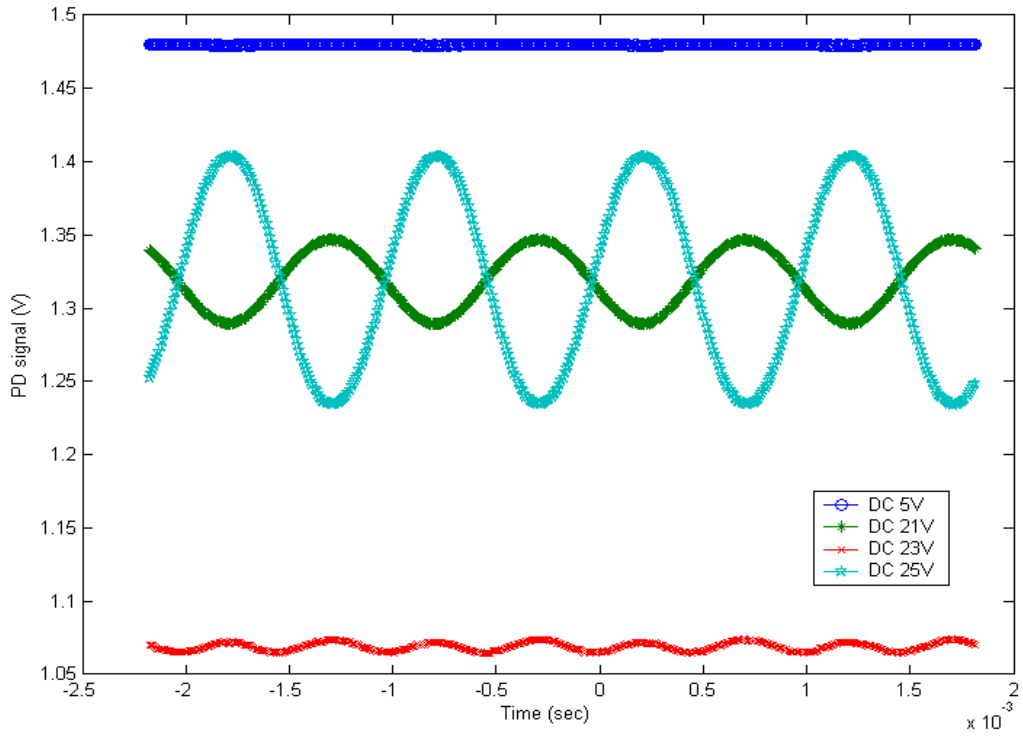
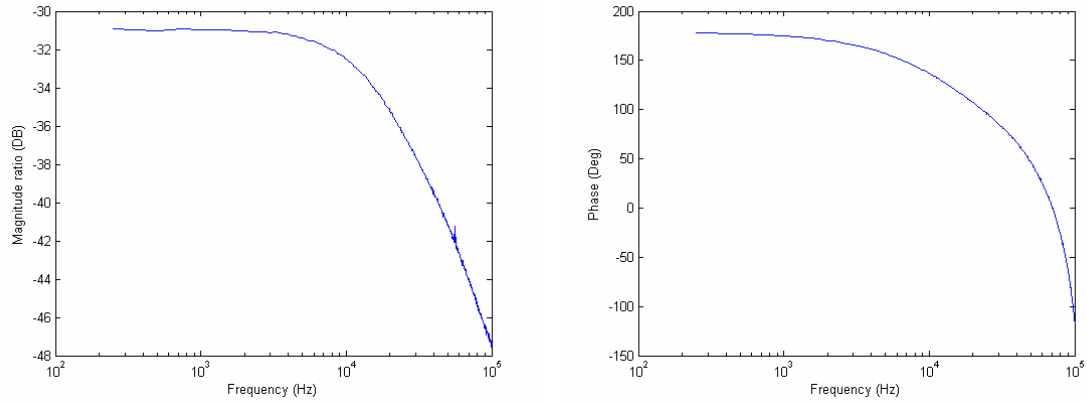


Figure 79. AC ($\pm 0.5V$) response at certain DC bias at Figure 77



(a) Magnitude

(b) Phase

Figure 80. Measured frequency response of the deformable grating

4.3 INTEGRATED SYSTEM

4.3.1 MICROLENS AND DEFORMABLE GRATING INTEGRATION

In first approach, the microlens was fabricated on a wafer which already has a fabricated deformable grating at the other side. But the reflow technique involving high temperature of 180 °C caused thermal plastic (permanent) deformation of the grating and the metal electrode was peeled off due to thermal stress. Consequently, the gratings were not functional. A few survived devices showed only limited deformation by electrostatic force. As a solution to this problem, the microlens has been fabricated on different quartz wafer and bonded with a wafer having a deformable grating. A UV cured epoxy (reflective index of 1.5) has been used to bond the two wafers after alignment. Figure 81 illustrates that the wafer having a lens is bonded with the wafer having a grating.

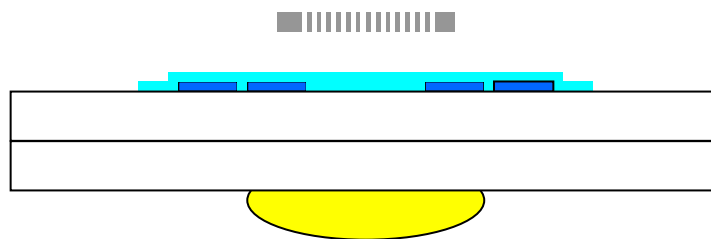


Figure 81. The deformable grating and lens in integration

4.3.2 INTEGRATED OPTOELECTRONICS

The integrated microlens and deformable grating need a photo diode at backside to monitor a diffraction order reflected from the beam from the target. Since the μ SI is designed as an array such as 3x3, 5x2, and 8x2, it is important to avoid optical crosstalk between neighboring elements meanwhile increasing fill-factor-a number of measuring devices per unit area. Figure 82 shows the fabricated array of 3x3 detectors. It has a hole of 200 μ m diameter at each cell to allow light illumination from backside of the wafer. The photo diodes are designed to measure the reflected 1st diffraction order of the beam. Detector array is angled to reduce the optical crosstalk. The silicon photo diode was designed by Lee *et al.* [97] and fabricated at CMOS group of Georgia Tech [104]. It is designed and fabricated with a standard N-well CMOS technology. Two different PN type PD structures are designed to detect light emitted from a laser diode wavelength of 600-900nm; N-well/P-substrate and a vertical combination of P+-source (drain)/N-well and N-well/P-substrate. To provide the optical interconnection between the laser and the membrane, through-wafer holes are etched in the silicon substrate as a post-CMOS process. Since D_{PD} , distance from the hole center to the diode center is fixed to 325 μ m, D_{G-PD} , distance can be calculated by Equation (16) with given wavelength, λ and the grating period, Λ to measure 1st diffraction order as shown in Figure 83. For example, $\lambda = 0.633\mu\text{m}$, $\Lambda = 6\mu\text{m}$ gives D_{G-PD} about 3.1mm.

$$D_{G-PD} = \frac{D_{PD}}{\tan \theta}, \text{ where } \theta = \sin^{-1} \left(\frac{\lambda}{\Lambda} \right) \quad (16)$$

Figure 84 shows a diced 3x3 detectors.

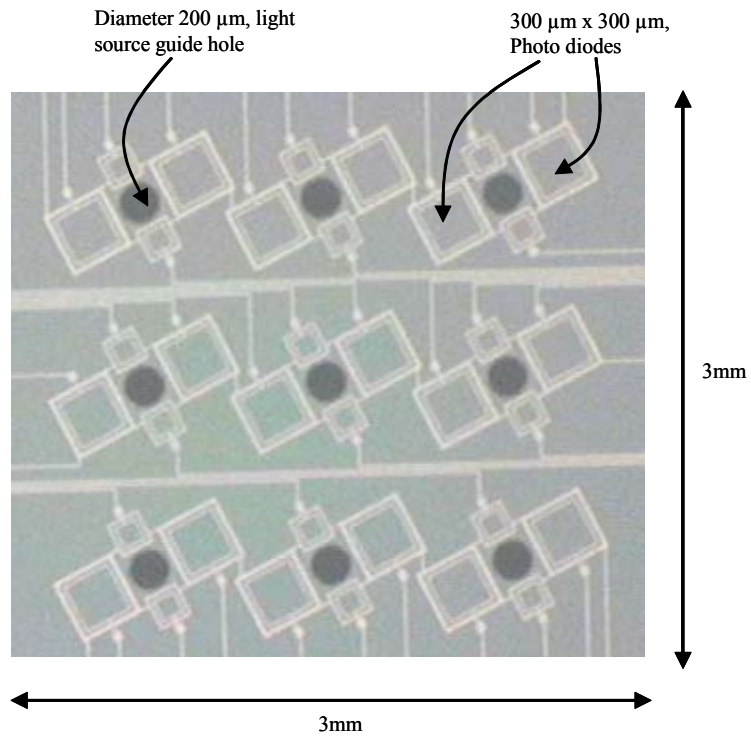


Figure 82. A fabricated array of 3x3 detectors

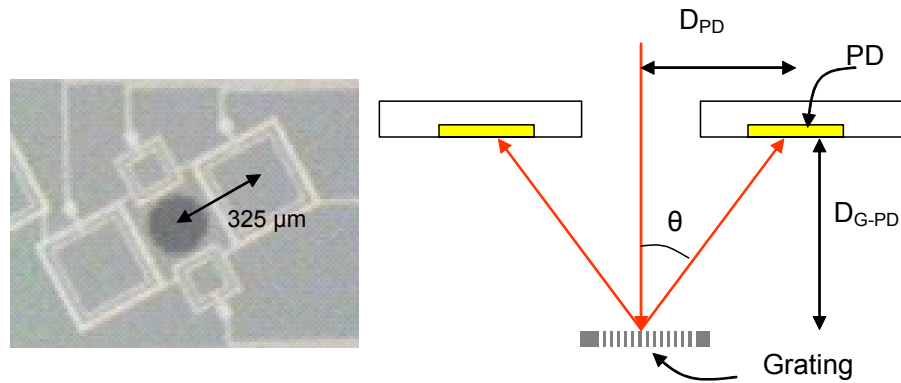


Figure 83. Grating and PD location

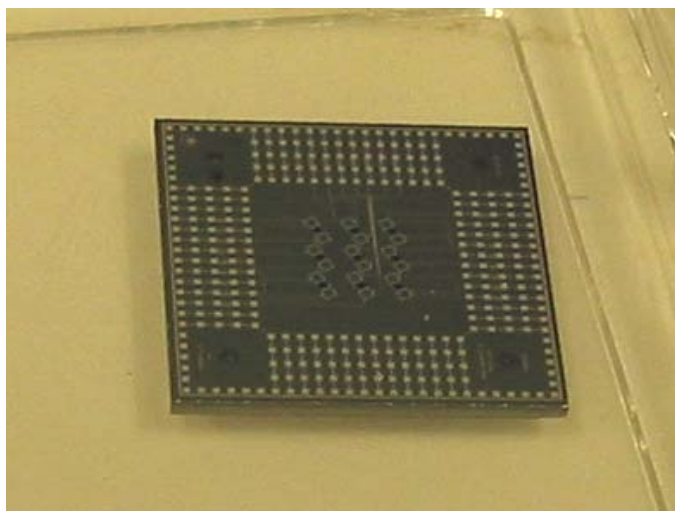


Figure 84. Diced 3x3 detectors for ready to mount on PCB

Figure 85 shows a diffracted intensity by 3 μm period of the grating on the photo diode which is placed at 1000 μm behind the grating. It demonstrated that the intensity at 5th order is negligible. Since the 3rd order is located at 500~1000 μm distance from the PD hole center in this case or at 1000~1500 μm distance if the D_{G-PD} increases to 1500 μm , the crosstalk between neighboring elements is not expected. To decrease the size of the array with a certain physical size of PD at both side of the hole, the number of grating needs to be decreased to reduce the size of the grating membrane. Present design has 16 gratings for a 6 μm period and 25 gratings for a 4 μm period. It requires more analysis to reduce the number of the grating in this purpose since reduced number of the grating can cause reduced the intensity at the diffraction order. More dramatic reduction of the size of the array can be achieved if one of PD is removed. But again, there is a limit due to the crosstalk by the 3rd diffraction from the neighborhood. Since the higher diffraction orders more than 3rd order are negligible, the particular design of the grating to eliminate them is not considered.

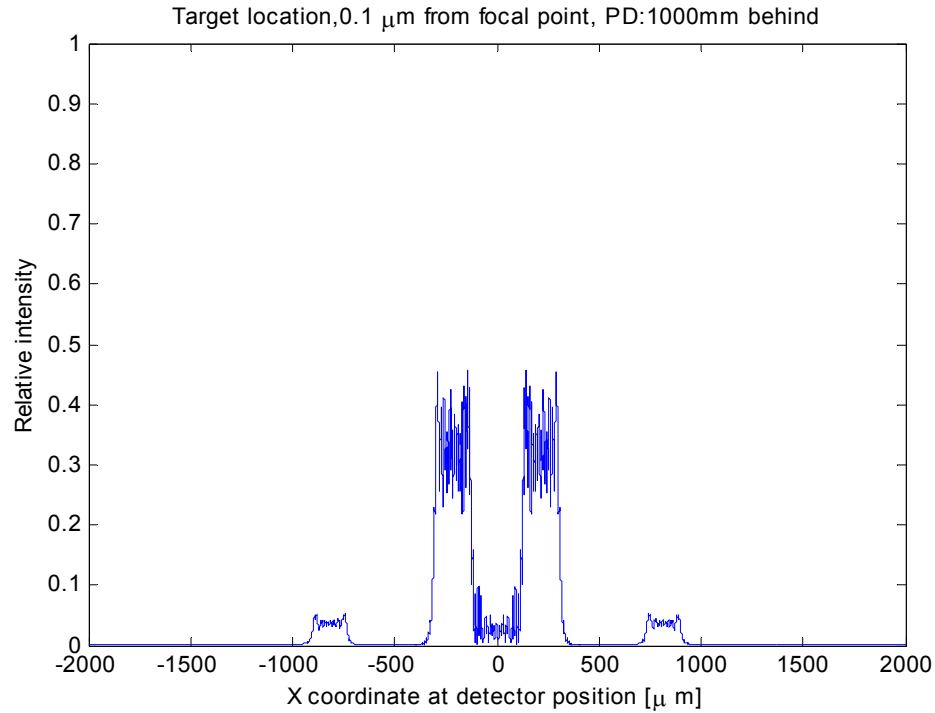


Figure 85. Intensity at photo diode plane showing 3rd diffraction order

4.3.3 PACKAGING

Figure 86 shows the schematics of the package for one cell. At first, a diced photo diode array is mounted on the PCB. Gold wire connects photo diode bond pads to the solder pads on the PCB for signal out and power input. A spacer is mounted on top of the diced photo diode chip. The thickness of the spacer is decided by period of the grating that is mounted on the spacer if the light source is fixed as explained last section. The spacer has been fabricated by a viper machine at Rapid Prototype Manufacturing Institute (RPMI) in Georgia Tech using a laser stereo lithography technique. It is convenient to change dimensions and shapes of the spacers in this technique. Figure 87 shows a wire

bonded photo diode chip and a spacer on PCB. On the spacer, a diced micromachined deformable grating chip is aligned and mounted using a chip mount machine at Package Research Center (PRC) in Georgia Tech. Since the deformable grating chip needs to be connected by gold wires for the actuation of the grating, the wire bonding must be done before assembly with the detector chip. Figure 88 shows an assembled deformable grating chip on the detector chip. Figure 89 shows an assembled microlens chip on the package which is ready for the scanning test. 3x3 shiny dots in the center are the fabricated microlenses.

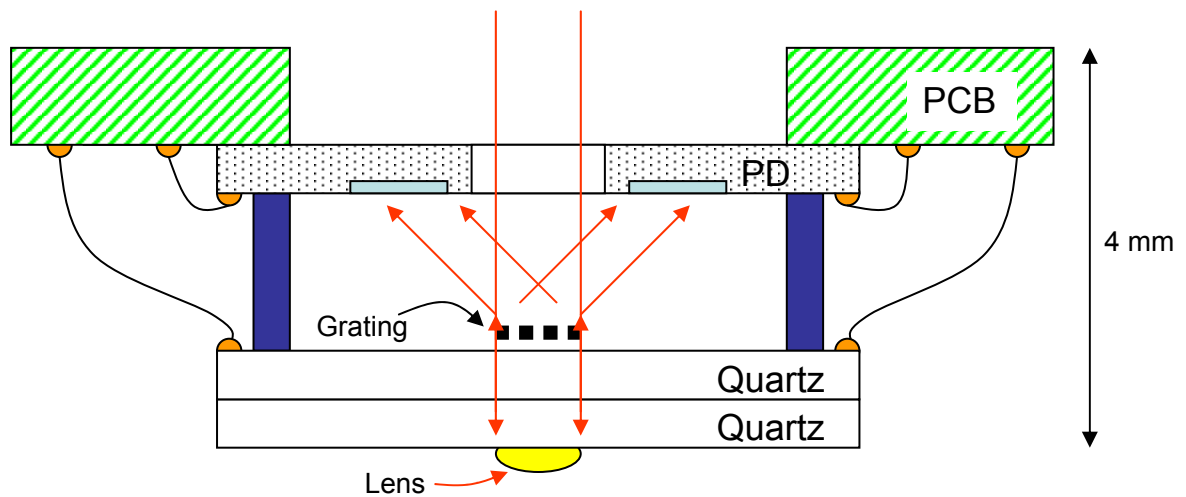


Figure 86. Schematics of the package

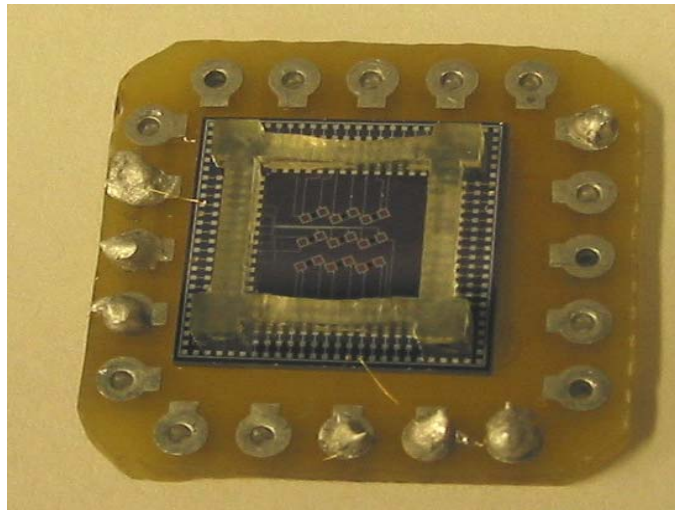


Figure 87. A wire bonded photo diode chip and a spacer

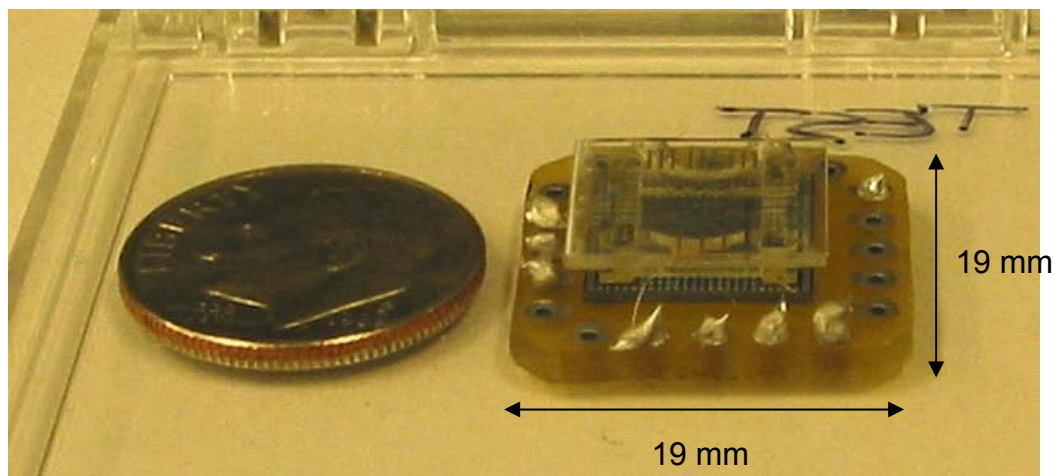


Figure 88. An assembled deformable grating chip on a detector chip

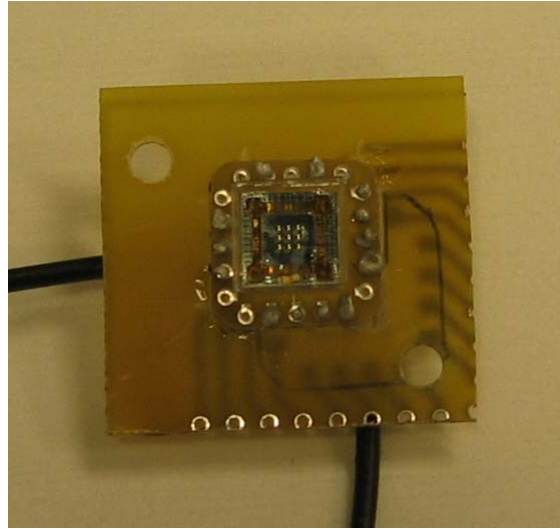


Figure 89.An assembled microlens chip on the top of the package

4.4 SUMMARY

The microlens was fabricated on quartz substrate with and without aperture. Diameter of 200 μm having 1mm focal length could be fabricated by 2000 rpm spinning of AZ P4620 PR and reflow technique on bare quartz wafer. But, the same lens was not fabricated on aluminum or chromium aperture. The deformable grating was fabricated through many of tuning of the process to get robust results. The most critical process was RIE to etch the aluminum to form a fine grating. The integration of the PD, grating and lens is another tedious process due to alignment requirements. The solder rework station in PRC is used to implement this step.

CHAPTER 5

EXPERIMENTS

5.1 SINGLE POINT MEASUREMENT

For proof of concept experiments, vibration of the micro fabricated microphone having 160 μm diameter membrane was investigated using a fixed grating interferometer with a microlens. Figure 90 (a) shows SEM image of a micro fabricated microphone. The material of the membrane surface is a sputtered aluminum. This microphone was fabricated by Hall *et al.* [46]. The microphone membrane is actuated by electrostatic force between aluminum membrane and electrode under the membrane as shown in Figure 90 (b). For the vibration mode measurements, 5, 10, 15 bursts signals at 720 kHz were applied in addition to 100V DC bias. Diffracted intensity was recorded at outside photo detector in experiment set-up as seen in Figure 91. The signal shows 720 kHz ≈ 10 cycles/ 1.39×10^{-5} sec and ringing (few cycles more than the excitation cycles), which is due to under damped behavior of the mechanical structure, after each burst in the recorded signal in Figure 92. These signals demonstrate the grating interferometer's capability of measuring the vibration of the MEMS microphone. In this case, the

vibration displacement was less than a quarter of the wavelength ($633\text{nm}/4=158\text{ nm}$) within a peak to peak interference curve.

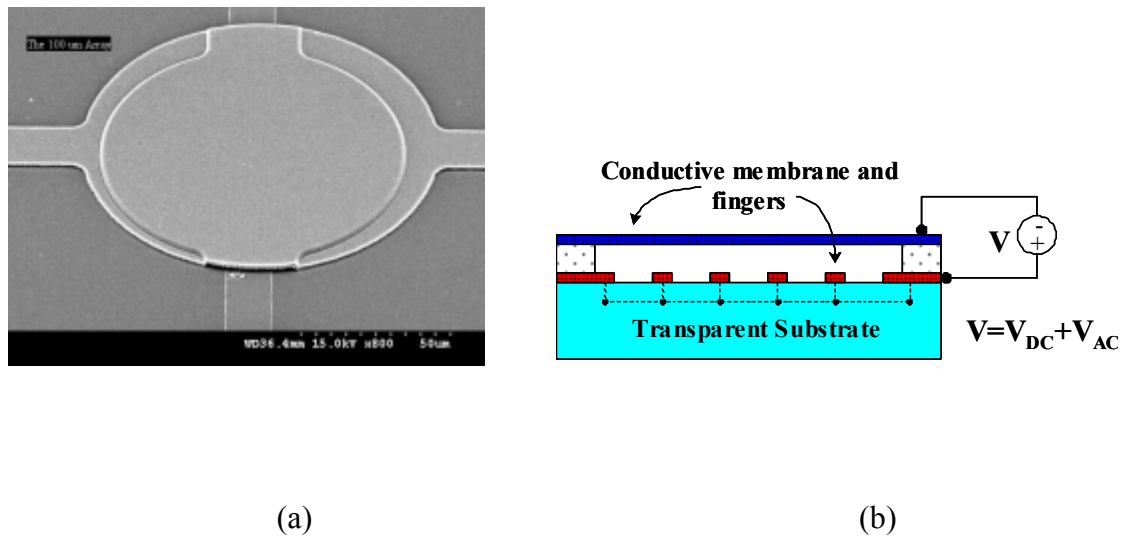


Figure 90. Micromachined microphone (a) SEM picture (b) electrostatic actuation by bottom electrodes

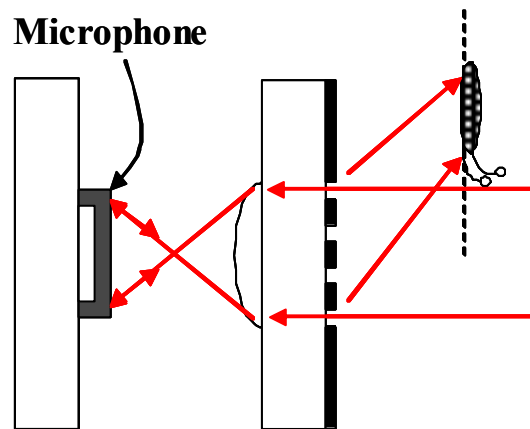


Figure 91. Experimental set-up

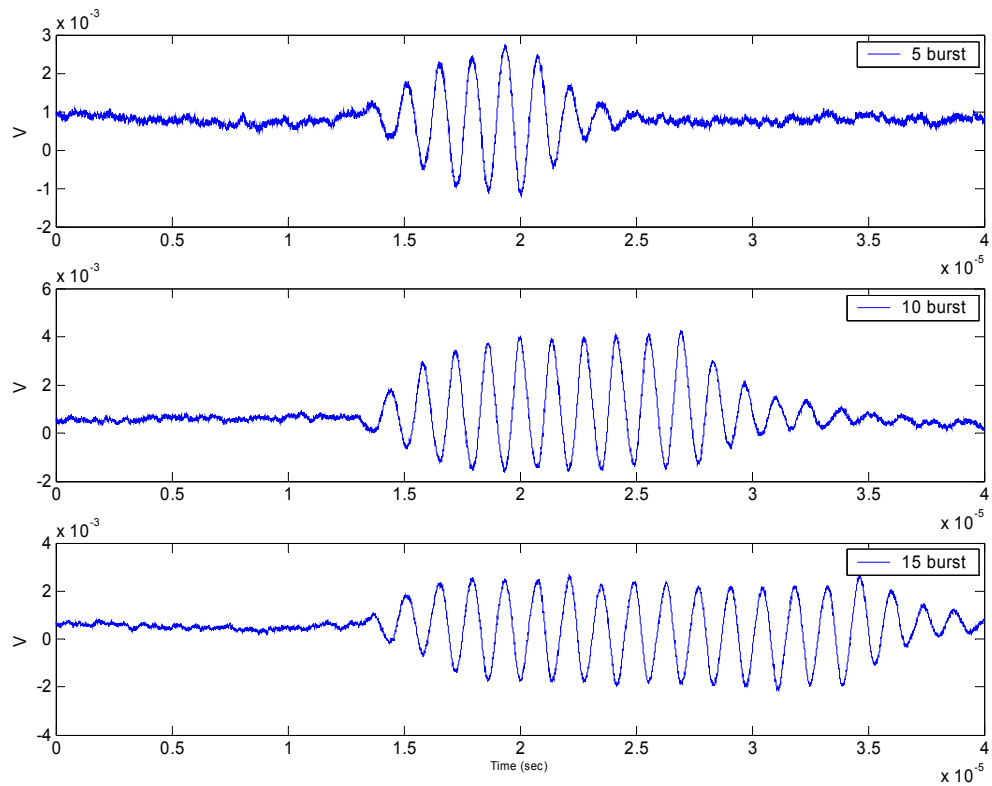


Figure 92. Detector signal for 5, 10, 15 burst

Another experiment was performed to measure vibration magnitude of the MEMS under test. The membrane was actuated by a sinusoidal burst (40V DC offset plus 15 sinusoidal bursts with 10V AC at 726 kHz and 5 msec repetition) while the whole unit was moving away from the μ SI (z axis in Figure 93) at an average speed of 50 μ m/sec. Figure 94 shows that the detector output is a sinusoidal function of displacement with a period of half wavelength ($633\text{nm}/2$) as demonstrated in the analysis and feasibility test at CHAPTER 3. This signal also shows the burst excitation of the microphone membrane. These bursts are enlarged in Figure 95. As can be seen, the detector output shows ringing again. Since the burst is on certain slope of the interference curve, the vibration

magnitude can be calculated by the detector output (mV) divided by the slope [mV/{sec*50($\mu\text{m}/\text{sec}$)}]. For example, the slope at burst #1 is 75mV/ms=1.5mV/nm. Thus peak to peak amplitude of burst #1 is about 10nm. Since root mean square error (RMSE) of the signal is 0.0019 and RMSE of the noise is 7.5390×10^{-5} in Figure 92, signal to noise ration (SNR) is $20 \log \left(\frac{\text{RMSE of signal}}{\text{RMSE of noise}} \right) = 64.5 \text{dB}$.

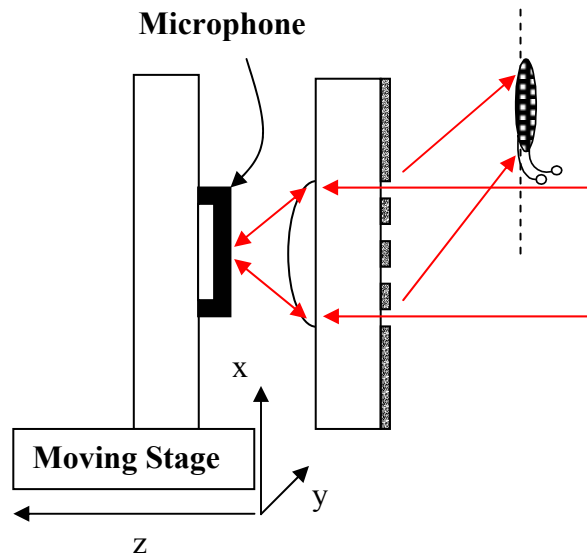


Figure 93. Experiment set-up

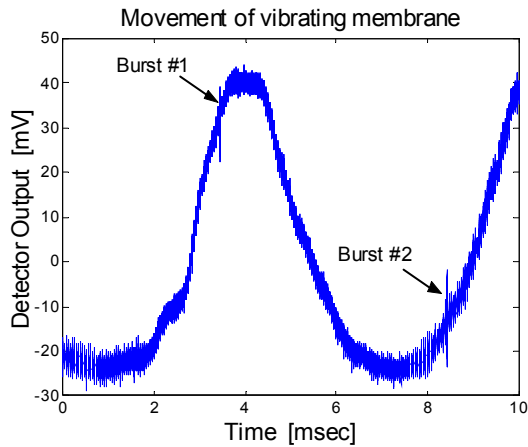


Figure 94. Detector signal showing an interference curve

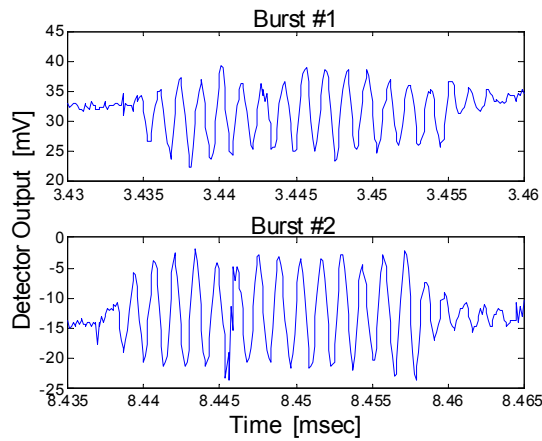


Figure 95. Magnification of data presented in Figure 94

5.2 PHASE SENSITIVE DETECTION

To reduce the vibration noise during the scanning, the experimental set-up has been modified to include a phase sensitive detector (lock-in amplifier). Similar MEMS microphone membranes have been used as the device under test. The membrane that was

used in this experiment has a diameter of 150 μm , a thickness of 1 μm and a 2.5 μm gap between its electrodes. In this particular case, the microlens has 200 μm diameter and 0.3mm focal length. It is fabricated on the 150 μm diameter aperture. The diffraction grating in the μSI with 33% fill factor, 6 μm periodicity was used. The light source was HeNe laser. The schematic of the μSI scanning system set-up is depicted in Figure 96. For the scanning purposes, x-y plane actuator was implemented to scan the MEMS microphone and the z direction actuator was used to adjust the distance from μSI to the target surface to the focal length of the lens on the μSI . Figure 97 shows its physical set-up. The lens in the set-up was used as a condenser of the reflected beam to the detector. The membrane was actuated electrostatically using a 40V DC bias and 10V sinusoidal burst at 726kHz. For the phase sensitive detection the lock-in amplifier was locked to the AC actuation signal while the photo detector output was used as the input signal. The low pass filter removed high frequency components of the mixed signal and then only DC out which is proportional to the cosine of the phase difference between the input and the reference remained. With this configuration, the amplitude and phase of the input signal can be determined. During the experiments, the amplitude and the phase of the output from lock-in amplifier were recorded by data acquisition system at a sampling rate of 10 MHz followed by 10 averaging while the membrane was scanned in the x-y plane using a 5 μm by 5 μm grid size. Figure 98 shows mapping of $A(x,y)*\cos(\theta)$, where $A(x,y)$ is the amplitude, and θ , is the phase of the vibration at point (x,y) . The resulting image shows a significant reduction in the noise outside of the vibrating membrane. Nevertheless there are still some artifacts such as the slanted fringes superimposed on the measured vibration profile. These problems can be solved by using an active control scheme to

keep the sample/diffraction grating distance at the maximum sensitivity level, i.e. the maximum slope of the fringe pattern [55].

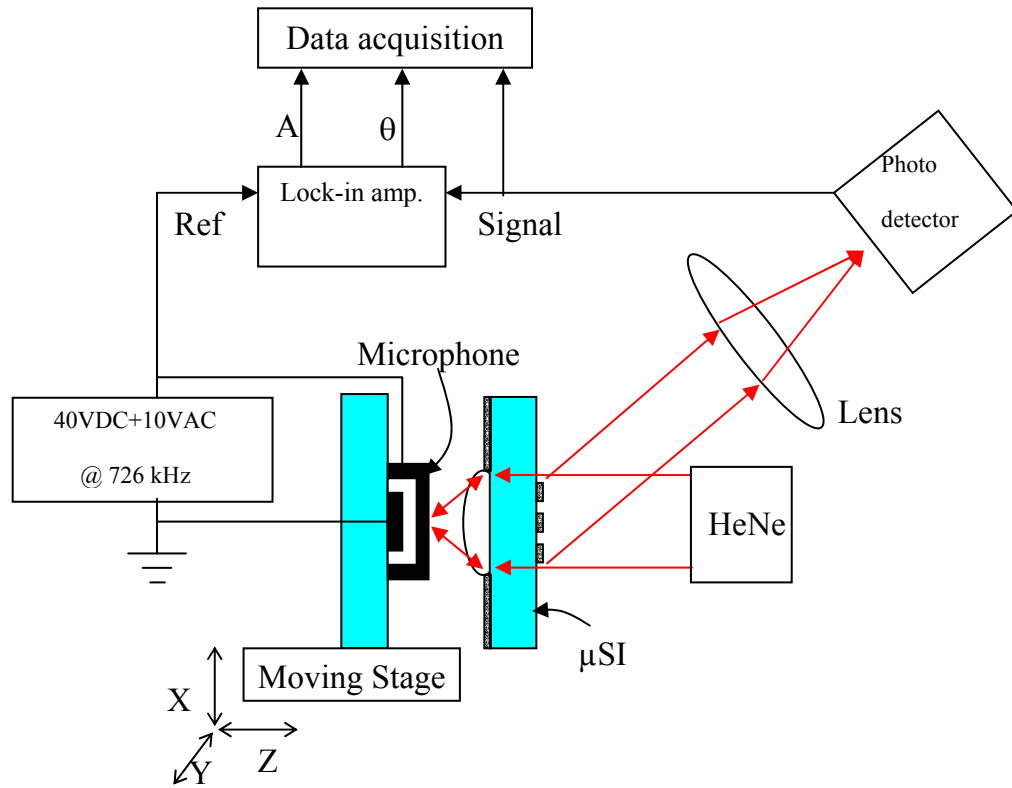


Figure 96. Schematics of μ SI scanning system with lock-in amp

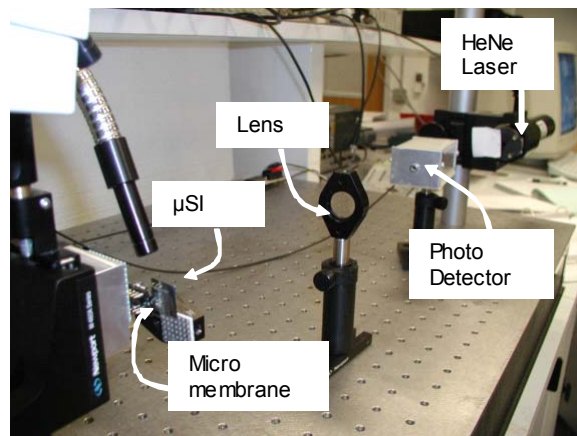


Figure 97. Physical experiment set-up

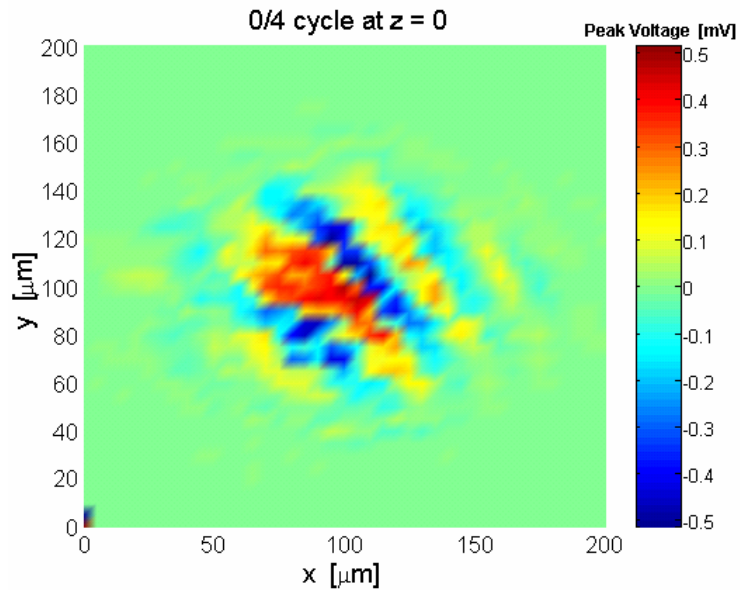


Figure 98. Scanning results using phase sensitive detector

5.3 LATERAL IMAGING PERFORMANCE

The lateral imaging capability of the μ SI is tested by scanning a $0.2\mu\text{m}$ thick, $20\mu\text{m}$ wide aluminum line on quartz wafer. A micrograph of the cMUT in this experiment is shown in Figure 99. As shown in the figure, the width of this trace is $20\mu\text{m}$ and the black background is a quartz substrate. The experimental set-up for this scanning is the same as in Figure 93. Since the lateral resolution is determined by the focusing microlens, the cMUT must be located on the focal plane of the lens. Figure 101 shows the scanned image of the trace. It is scanned in the x-y plane using a $0.25\mu\text{m}$ by $0.25\mu\text{m}$ grid size. The data is sampled at 10 MHz followed by 5 averaging. The averaged values were

recorded using a data acquisition system. Figure 101 illustrates that the lateral resolution of the μ SI is approximately $3.6\mu\text{m}$. These results show the microlens' capability of focusing which improves lateral resolution of the scanning.

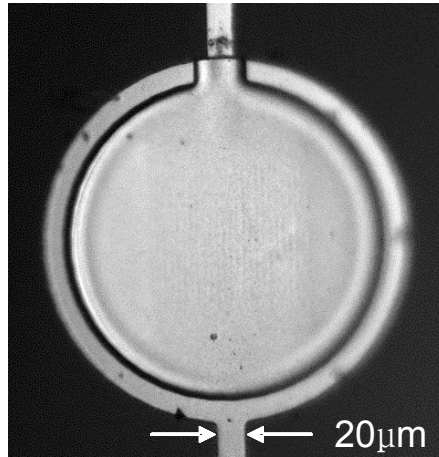


Figure 99. A trace in the cMUT that is used in the lateral scanning

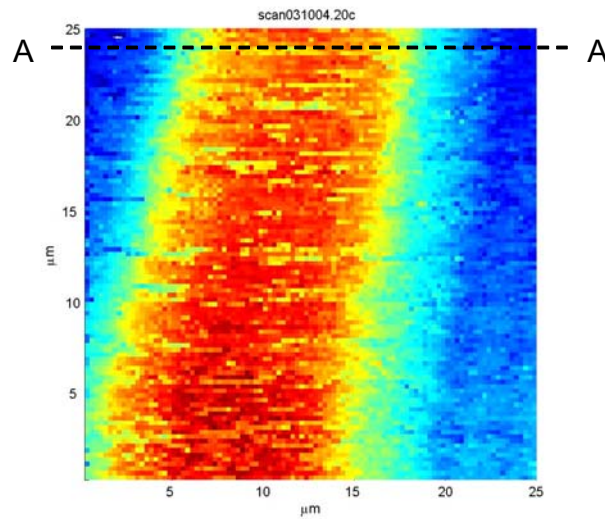


Figure 100. Fine scan on the trace

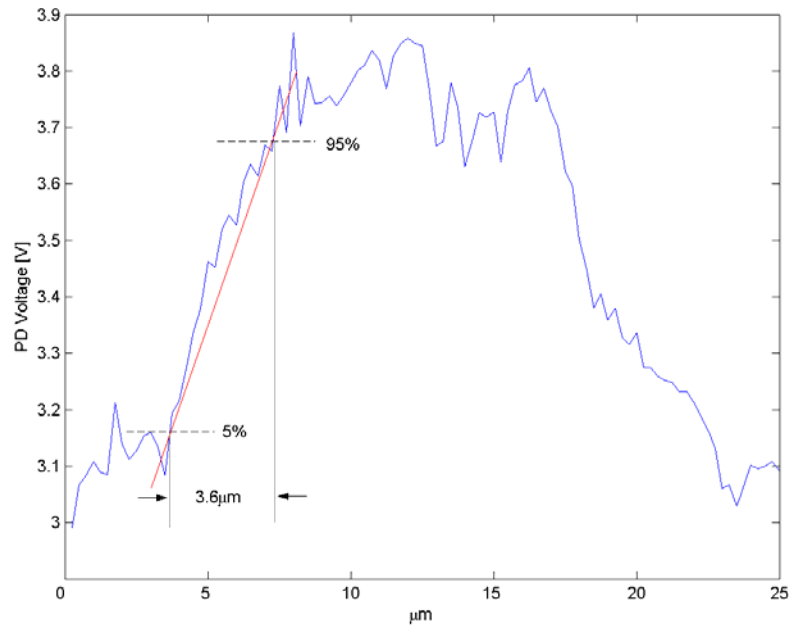


Figure 101. Results on the cross-section of A in Figure 100

5.4 DC METROLOGY PERFORMANCE

5.4.1 EXPERIMENT WITH A NON-INTEGRATED μ SI

The schematic of the experimental set-up to measure DC metrology of cMUT is depicted in Figure 102. A HeNe laser is used as the interferometer light source, which is incident upon the aperture and grating of the μ SI through a focusing lens that is intended to reduce the beam size. A portion of the laser light passes through the grating, and a portion is reflected off the grating surface. The light that passes through the grating is

reflected from the microphone membrane surface, and passes back through the grating. This reflected light interferes with the light reflected off the grating, creating diffraction orders. The first diffraction order passes through a collimating lens and is detected by a photodiode and amplifier. The micro positioning stages then move the sample a small amount and another measurement is taken. In this fashion, a raster scan of the surface is constructed. An image map of these measurements is then created with each point in the raster scan represented by one pixel. In this setup, a photodiodes with a bandwidth of DC-600kHz is used.

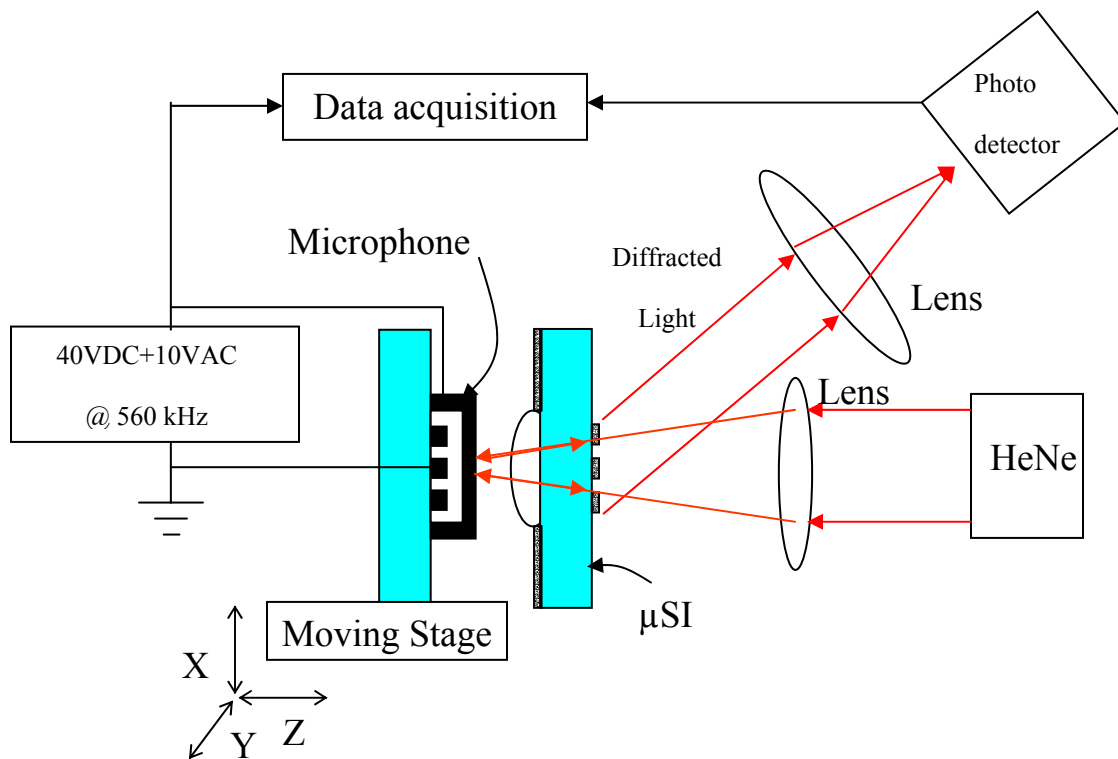


Figure 102. Schematics of experiment set-up

The optical imaging and vibration profiling capability of the μ SI is tested using a circular membrane of a cMUT as the sample. A micrograph of the cMUT in this experiment is shown in Figure 103, along with a zoomed in version of the center portion which shows the impression of the backside electrode on the membrane. The 3-D static profile of the cMUT membrane has also been measured using a white light interferometer. As shown in Figure 104, the membrane has a curvature deviating by as much as $1\mu\text{m}$ from an ideally flat membrane, increasing the gap thickness to around $3.5\mu\text{m}$ around the center. This non ideal shape is due to internal stress that develops during fabrication process.

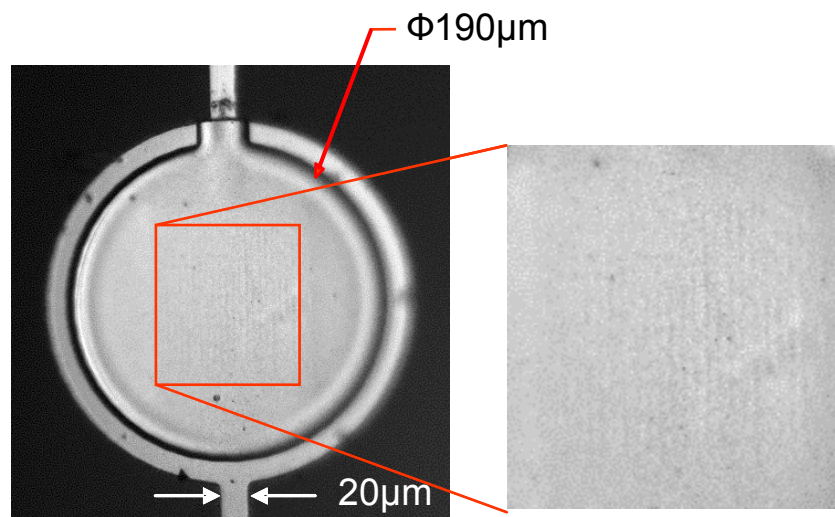


Figure 103. Optical microscopy image of a cMUT showing membrane diameter and trace width

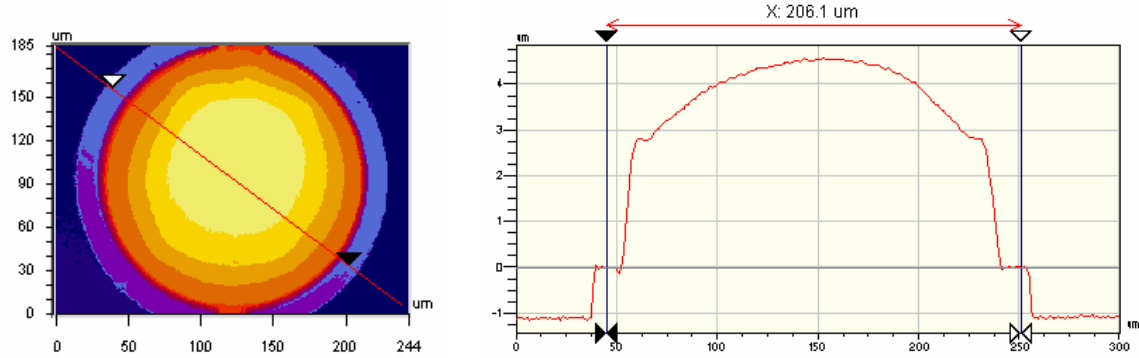


Figure 104. Static profile of a cMUT using a Veeco white light interferometer

For optical measurements the μ SI is positioned at the focal distance from the cMUT membrane. The reflectivity map and the vibration profile of the first resonant mode of the cMUT membrane are measured simultaneously. The cMUT is actuated with a 40V DC and 10V AC sine wave at its first resonant frequency of 560 kHz. Figure 105 shows the average DC values measured by the μ SI over the surface of the cMUT, which is a static measurement. Since the out of plane deflection is greater than $\lambda/2$, the signal wraps around the optical intensity curve shown in Figure 22. This creates a vertical striped pattern across the face of the average reflectivity measurement. Yet, the trace connecting the cMUT to a bond pad is clearly visible at the bottom of the image. In addition to the wide dark stripes due to the bow of the membrane, a somewhat periodic pattern is also observed in the average DC measurement. This artifact is due to mechanical vibrations coupled to the system, which randomly changes the sample-grating distance. Figure 106 is a plot of the cross section A-A in Figure 105. The plot shows the reflectivity and the surface profile with this artifact. Thus, this DC metrology shows reflectivity as well as surface profiles in the presence of the noises. Instead of this bulky

actuation scheme, a micromachined, electrostatically actuated deformable grating can be fabricated and integrated with the μ SI. This approach also enables implementation of μ SI arrays, where each element of the array is individually controlled.

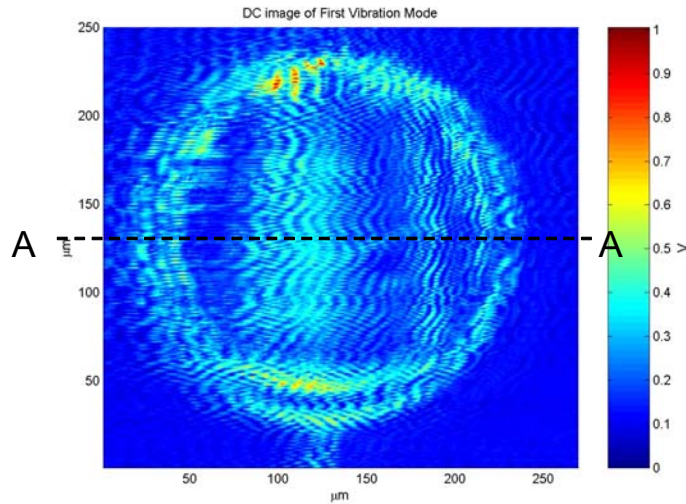


Figure 105. Average DC image of a cMUT

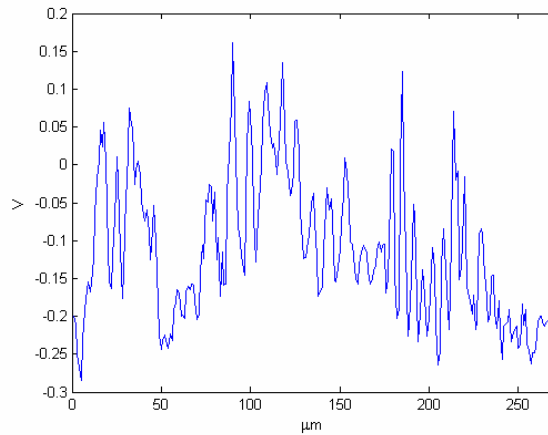


Figure 106. Values of the cross section A-A in Figure 105

5.4.2 EXPERIMENT WITH AN INTEGRATED μ SI

The physical scanning set-up with an integrated μ SI is shown in Figure 107 and its schematics are in Figure 108. The set-up used a low noise current amp to convert photo current of the PD to voltage. The set-up was implemented on optical table with vibration isolator which removed well high frequency vibration noises from the floor. Also, the integrated PD and grating can avoid a mechanical noise which comes from relative distance change between the two. This system can record surface vibrations upwards of 2MHz which is a bandwidth of the fabricated photo detector and low noise photodiode amplifier. Figure 109 shows diffracted beam pattern on an image plane of MEMS under test side. Since the diffracted order 0 passed through a microlens, the image of the 0 order shows an image of the backside grating. In the scanning, the MEMS under test is placed at focus of the lens. Figure 110 shows one of the cMUTs that have been used in this experiment. The cMUT is actuated with a 30V DC and 10V AC sine wave at its first resonant frequency of 900 kHz. Figure 111 shows the cMUT surface profile at 30V DC which is measured the Veeco white light interferometer. Figure 112 shows the average reflectivity and the surface profile measured by the μ SI over the surface of the cMUT, which is a static measurement. Figure 113 (a) shows again the lateral resolution of the measurement on a trace. The trace in the center has a 60 μ m width and a 1.7 μ m height from 20 μ m width aluminum wedges at both sides. Since the cMUT membrane plane is vertically inclined greater than $\lambda/2$, it creates a horizontal striped pattern across the face of the average reflectivity measurement. Interference curve in Figure 113 (b) shows this inclination and flat surface of the cMUT with noise at 80-190 μ m regions.

Figure 113 (c) shows the values at section C-C which is well demonstrating the surface profile at 50-210 μm region.

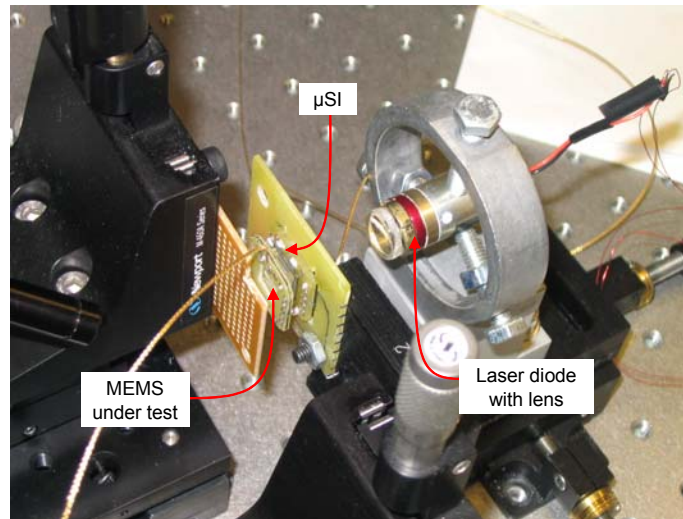


Figure 107. Picture of the experiment set-up

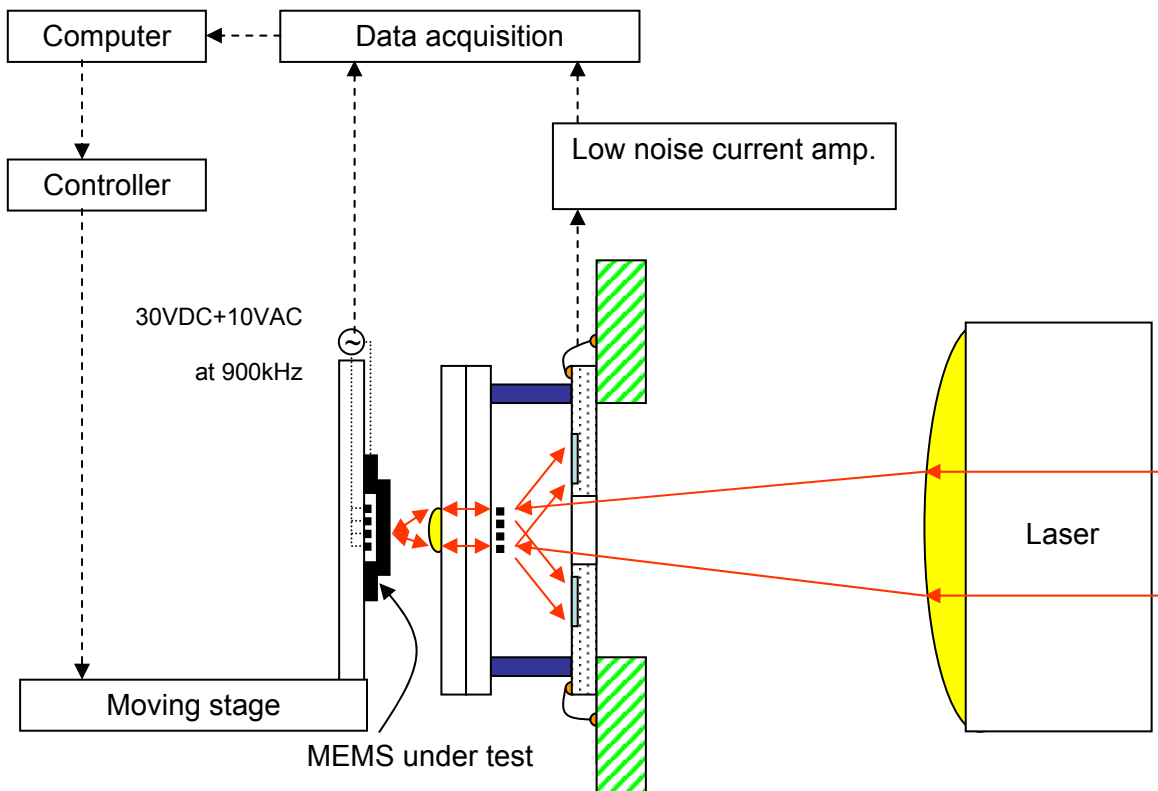


Figure 108. Scanning set-up for integrated μSI

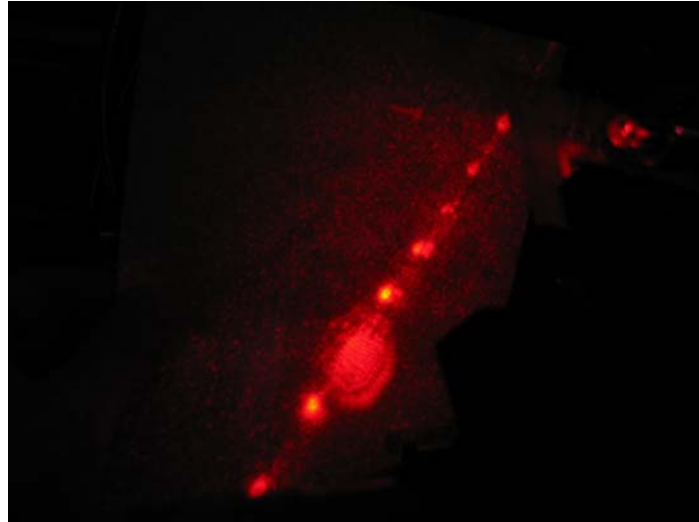


Figure 109. Diffracted beam pattern after μ SI

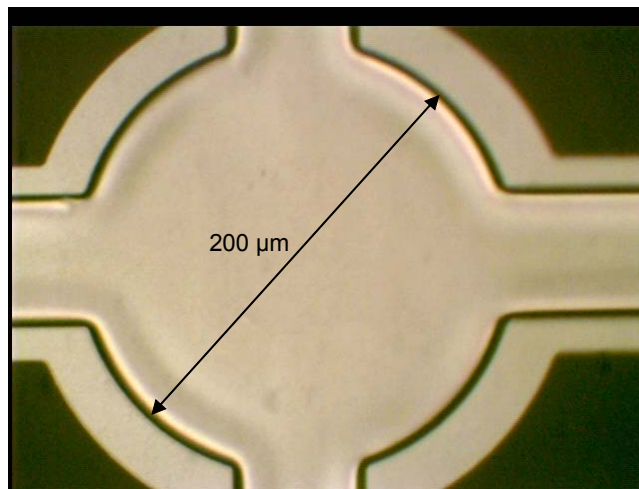


Figure 110. Microscope picture of one of the scanned cMUT

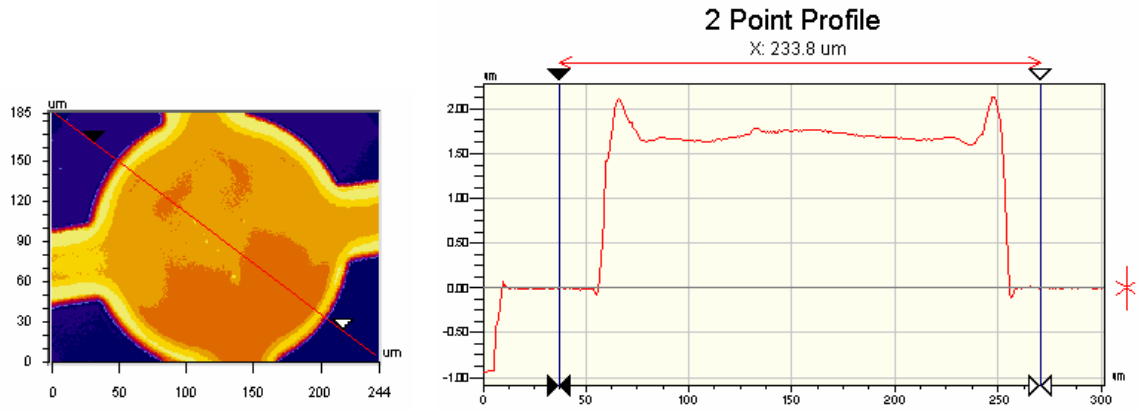


Figure 111. The cMUT surface profile at 30V

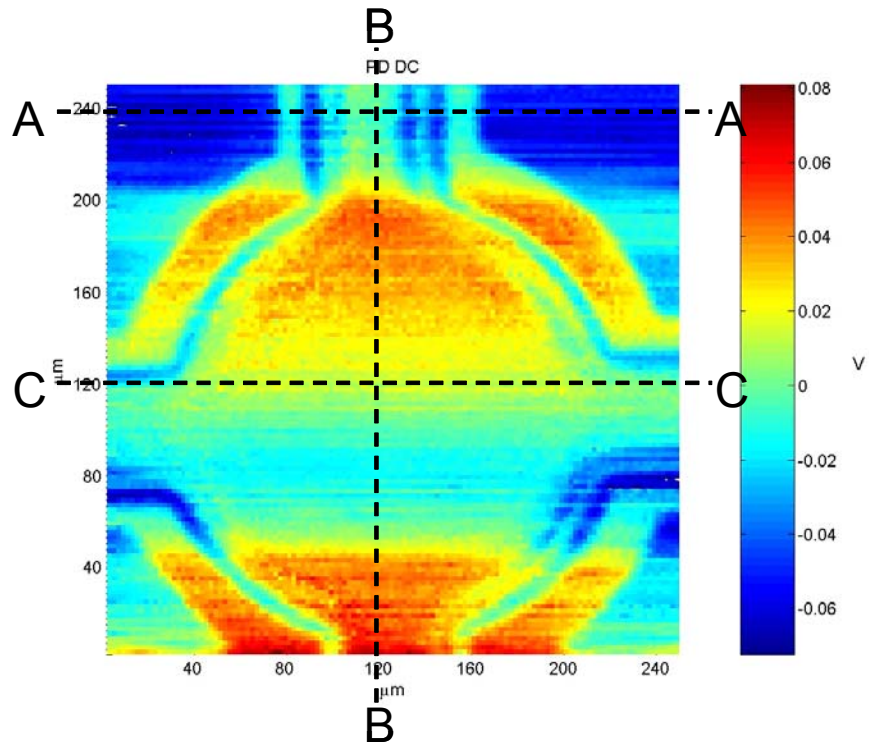
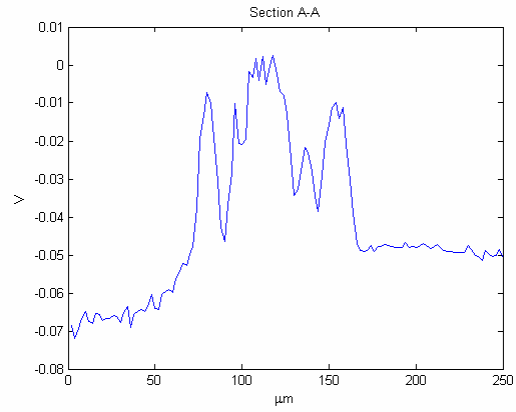
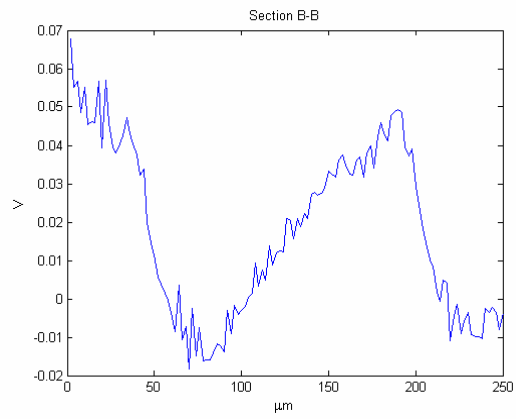


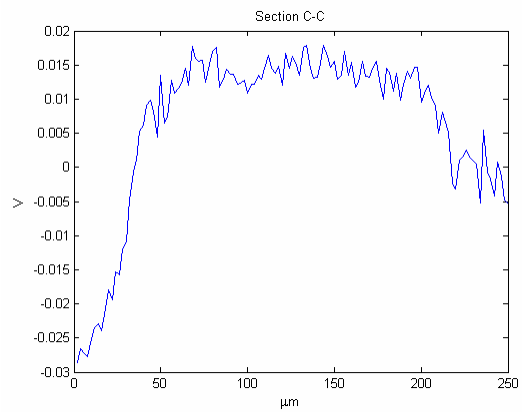
Figure 112. Average DC image of a cMUT



(a)



(b)



(c)

Figure 113. Cross-section (a) A-A (b)B-B (c)C-C in Figure 112

5.5 VIBRATION AND MODE SHAPE MEASUREMENT

5.5.1 EXPERIMENT WITH A NON-INTEGRATED μ SI

The same experimental set-up in Figure 102 is used to measure vibration modes of cMUT. The amplitude of this motion is found by digitizing the photodiode output at 10MHz, then digitally notch-filtering this signal around the known actuation frequency, and taking the peak to peak signal amplitude. In this setup, two different photodiodes were used, one with a bandwidth of DC-600kHz for the first mode at 560kHz and the other with a bandwidth of 1kHz - 6MHz for the second mode at 1.25MHz.

Simultaneously with static measurements, the μ SI can be used for dynamic measurements. Figure 114 shows the first vibration mode and the second vibration mode of the circular membrane. The theoretical first vibration mode for a 1 μ m thick circular aluminum membrane of 190 μ m diameter is 560kHz. At this actuation frequency, there exists one circular node at the edge of the membrane. The dynamic surface map for the first vibration mode measured by the μ SI is shown in Figure 115 (a). The shape of this profile closely matches the FEM simulation of the membrane vibration profile using natural frequency solver in ANSYS shown in Figure 115 (b). The maximum measured vibration amplitude is 22.3nm, which is within 13% of a simple analytic model of a parallel plate electrostatic transducer [2]. Figure 115 (c) and (d) show values of the cross section A-A and B-B. It is clear that the plots show the first mode shape even though noises exist.

The second vibration mode for this circular membrane occurs at 1.25MHz and contains two circular nodes, one at the edge and one at approximately half of the radius of the circle. Figure 116 (a) shows the measured profile of the membrane actuated at this frequency. The shape of this profile correlates well with the theoretical mode shape shown in Figure 116 (b), as the second node is clearly visible approximately 50 μ m from the edge of the membrane. Figure 116 (c) and (d) show values of the cross section A-A and B-B. Figure 116 (d) clearly shows the second node and mode shape even though noises exist.

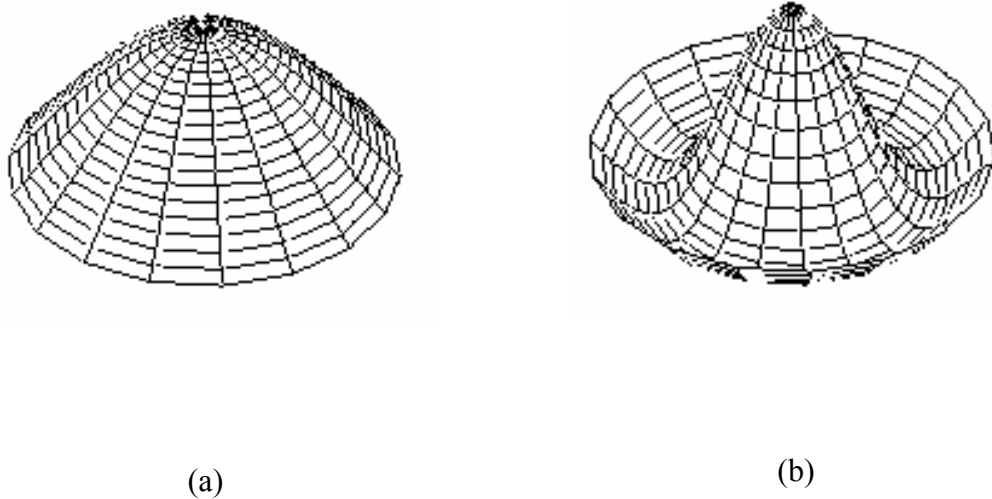
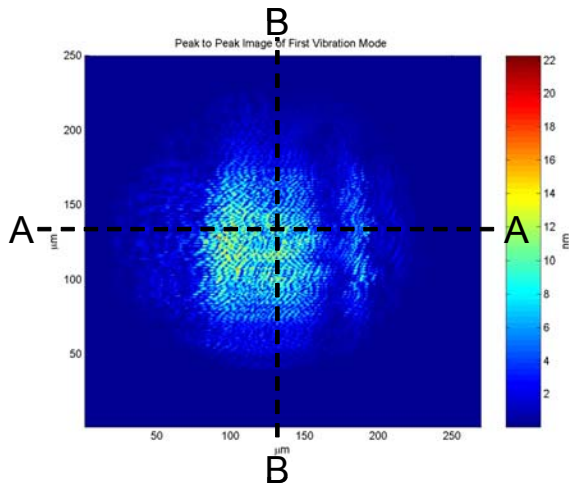
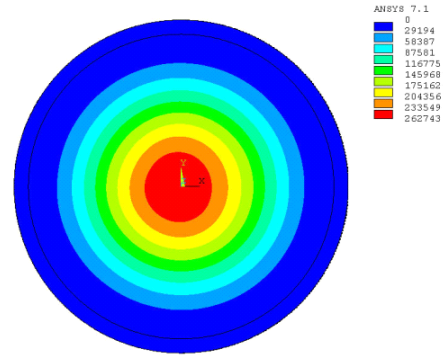


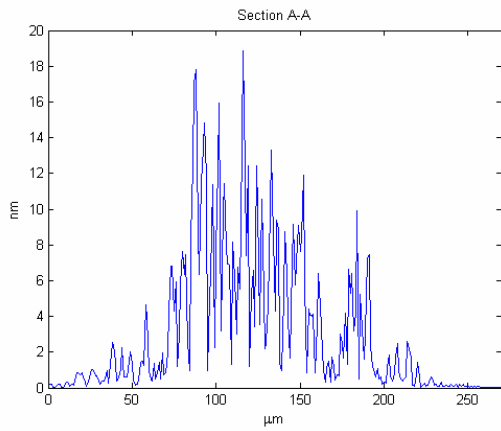
Figure 114. (a) First vibration mode shape (b) Second vibration mode shape



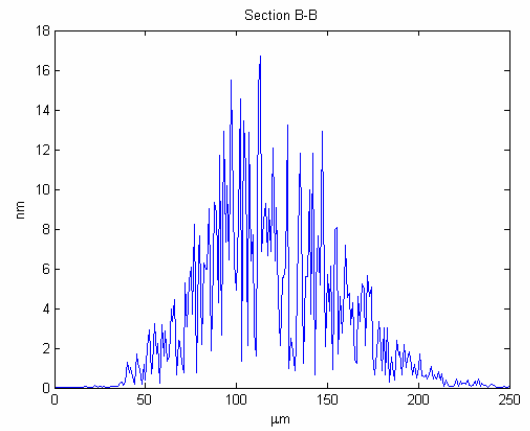
(a)



(b)



(c)



(d)

Figure 115. (a) Measured amplitude of the first vibration mode (b) Numerical model of the first vibration mode (c)Cross-section A-A (d)Cross-section B-B

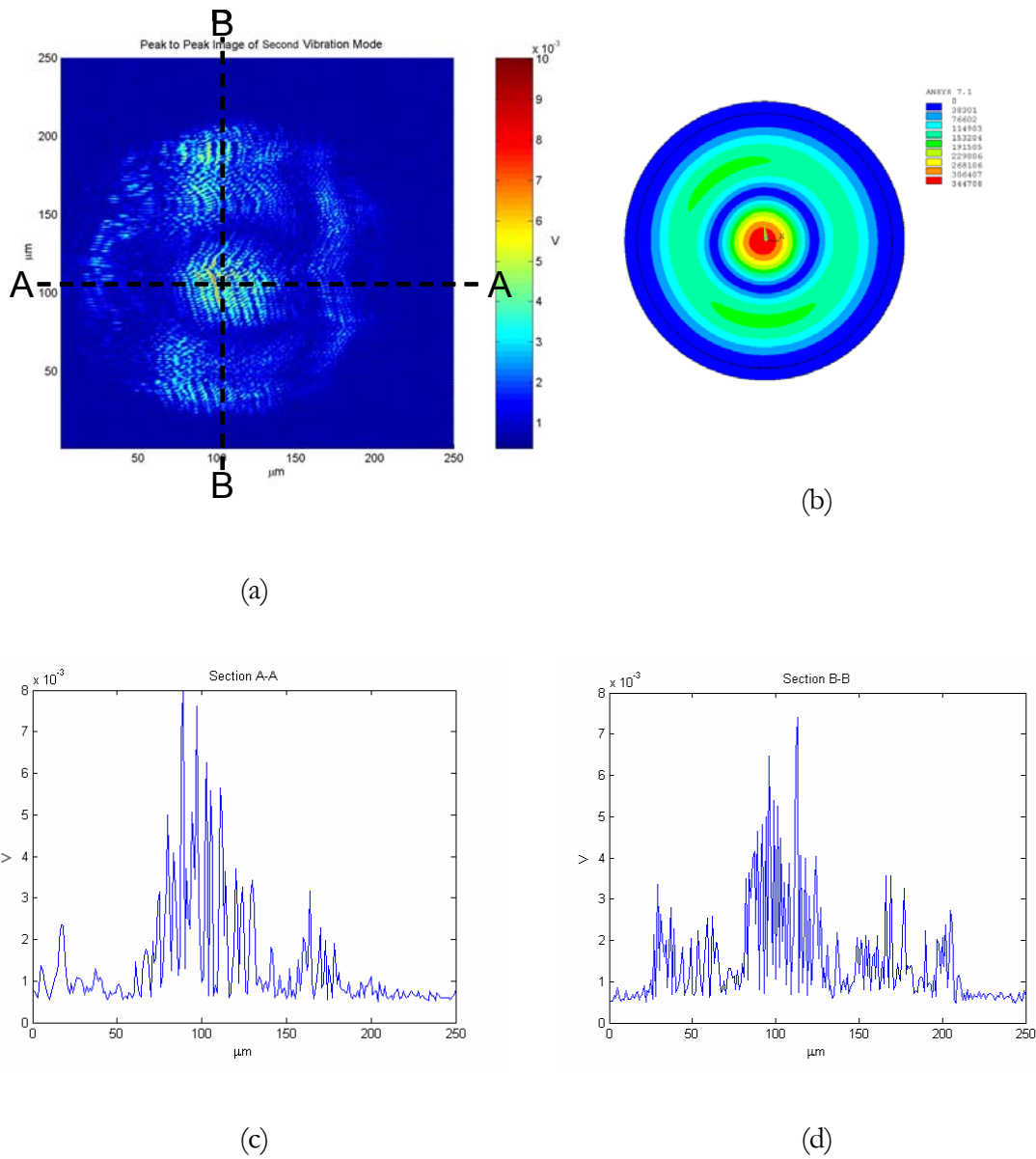


Figure 116. (a) Measured amplitude of the second vibration mode (b) Numerical model of the second vibration mode (c)Cross-section A-A (d)Cross-section B-B

Note that the same parallel dark stripes due to membrane curvature and a possible tilt are present in the measured vibration profiles as well as the average reflectivity image. However, the high spatial frequency fringes, which show up prominently in the average reflectivity image in Figure 105, do not show up in the same pattern in either of the vibration mode images suggesting that these are the result of low frequency mechanical vibrations coming from the environment. A method of reducing the impact of both the vibrations and the misalignment errors is to actively control the relative distance between the MEMS device and the μ SI. This can be achieved by either moving the sample with a piezoelectric actuator as it is used to measure the displacement profile of a rectangular thin-film resonator [57].

5.5.2 EXPERIMENT WITH AN INTEGRATED μ SI

The scanning set-up shown in Figure 108 and the same cMUT in Figure 110 are used in this experiment. a low noise current amp to convert current change in CMOS detector to voltage. In the scanning, the MEMS under test is placed at focus of the lens. The cMUT is actuated with a 30V DC and 10V AC sine wave at its first resonant frequency of 900 kHz.

The amplitude of this motion shown in Figure 117 is found by digitizing the photodiode output at 10MHz, then digitally notch-filtering this signal around the known actuation frequency of 900kHz, and taking the peak to peak signal amplitude. The measured amplitude of vibration is not uniformly varied due to vibration noises. Figure

118 (a) shows values of cross section A-A in Figure 10. It shows the vibration profile of the cMUT. To find out a vertical resolution of the measurement, a curve is fitted to the data at 50-194 μm regions in the cross section and root mean square error (RMSE) on this fitted curve is calculated. Figure 118 (b) shows this curve which is

$$V = -10^7(7.8x^2 - 1940.9x + 70132.2) \quad (17)$$

Here, x is x coordinate and V is y value. RMSE is 0.0014 V.

The vibration noises changes the distance between cMUT and μSI . This changed distance shifts a measurement point on the interference curve. These alignment and noises problems can be reduced using proportional-integral-differential (PID) control of the grating.

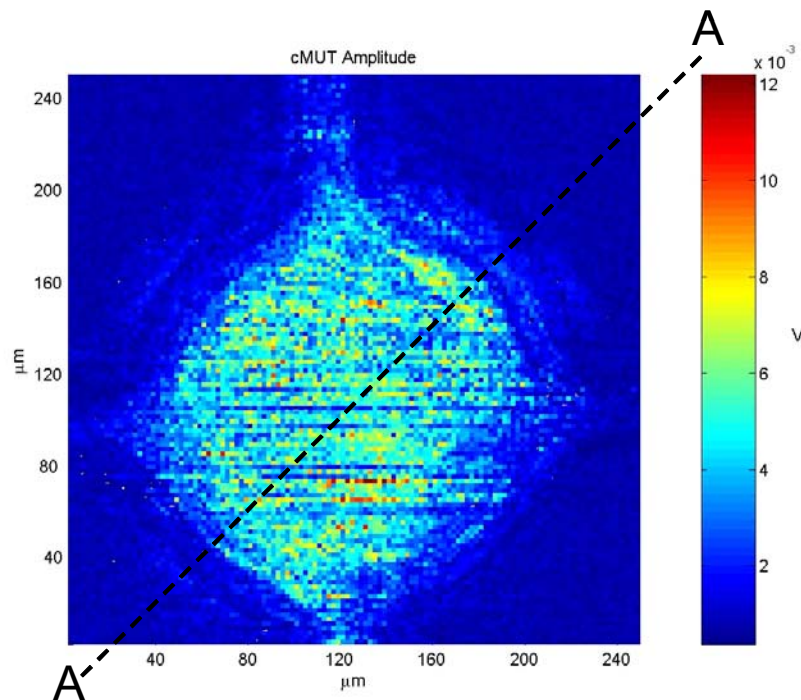
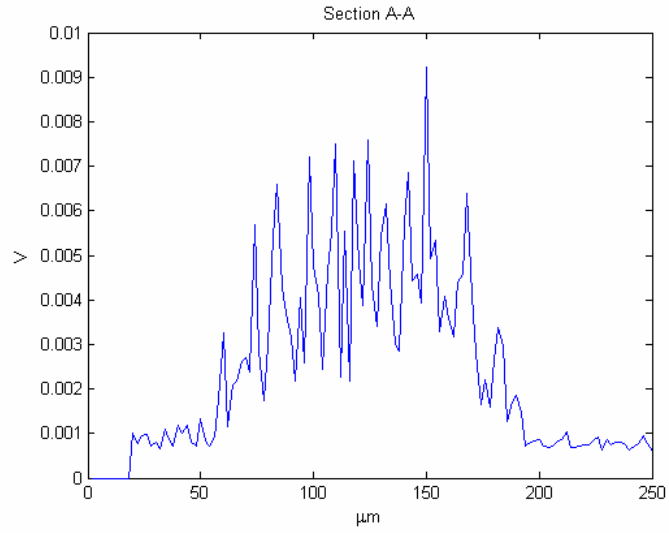
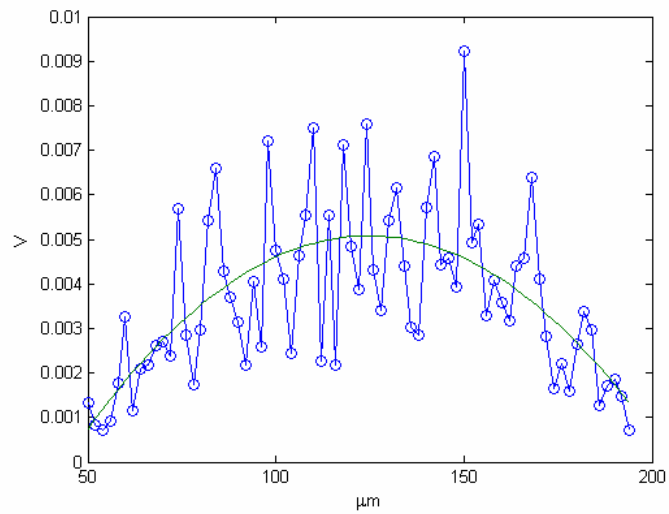


Figure 117. Measured amplitude of the first vibration mode



(a)



(b)

Figure 118. (a)Cross section A-A in Figure 117 (b)Curve fitting to A)

5.6 NOISE

The main sources of noise in the μ SI system are shot noise of the photo diode, thermal mechanical noise of the grating, laser noise, electronic noise of the circuit and mechanical vibration of the system which is similar to the case of an interdigital cantilever [92]. Figure 119 shows the equivalent noise circuit. The signal is denoted by current source, i_s , which is a function of the light intensity incident on the photo diode. From the circuit shown in Figure 119, the SNR is found as shown in Equation (18)

$$SNR = \frac{\left(\frac{di_s}{dd}\right)^2}{\langle i_{sh}^2 \rangle + \langle i_m^2 \rangle + \langle i_{ms}^2 \rangle + \langle i_l^2 \rangle + \langle i_e^2 \rangle} \quad (18)$$

Here, d : distance from the grating to the target, i_{sh} : shot noise of the photo diode, i_m : thermal mechanical noise of the grating, i_{ms} : mechanical vibration of the system, i_l : laser noise, and i_e : electronic noise of the circuit (amp) [92]. As described in Section 3.1.2, a simple analysis of the reflected field shows that the diffraction order intensities, I_0 and $I_{\pm 1}$ can be expressed as a function of d , as in Equation (19), where I_{in} is the incident laser intensity.

$$I_0 = I_{in} \cos^2\left(\frac{2\pi d}{\lambda}\right), \quad I_{\pm 1} = \frac{4I_{in}}{\pi^2} \sin^2\left(\frac{2\pi d}{\lambda}\right) \quad (19)$$

The highest displacement sensitivity and linearity for any diffraction order occurs when the second derivative of the expressions in Equation (19) with respect to d vanishes, which requires that d should be an odd multiple of $\lambda/8$. Therefore the output current, i_s ,

for a small displacement Δx around this optimum d , can be obtained by taking the derivative of these orders as,

$$di_s = R \left| \frac{\partial I_0}{\partial d} \right| dx \text{ or } di_s = R \left| \frac{\partial I_{\pm 1}}{\partial d} \right| dx, \text{ thus } di_s \propto RI_{in} \frac{dx}{\lambda} \quad (20)$$

In this equation, R is the PD responsivity. Since the zero diffraction order is complementary to the first diffraction orders, deriving the output signal with the difference of these orders increases the signal level, and uses the incident laser power efficiently as,

$$\Delta i_s = R \left| \frac{\partial (I_0 - \alpha I_1)}{\partial d} \right| \Delta x = RI_{in} \frac{4\pi}{\lambda} \Delta x \quad (21)$$

The odd diffraction order outputs are scaled by a factor α to equalize the signal levels to the zero order. Deriving the output signal with this differencing scheme also reduces the laser intensity noise, i_l . Shot noise of the photo diode, i_{sh} is given as $i_{sh} = \sqrt{2qI_{PD}}$ (A/ $\sqrt{\text{Hz}}$) where $q = 1.6 \times 10^{-19}$ C. Electronic noise of the circuit i_e can be small by increasing resistance R_1 in amp shown in Figure 119 since $i_e \propto 1/R_1$. Thus, mechanical vibration noise of the system, i_{ms} becomes a dominant noise. Therefore, a PID control scheme is required to minimize this mechanical noise and increase the minimum detectable distance (MDD). It is discussed in the next section.

For a given SNR, MDD of the system is calculated as,

$$MDD = \frac{1}{\sqrt{SNR}} \quad (22)$$

The interdigital cantilever in [92] shows a MDD of 0.0078\AA and minimum mechanical equivalent noise of $10^{-4} \text{\AA}/\text{Hz}^{1/2}$ in the noise analysis at 1 kHz bandwidth. Since their detection scheme is the same type, using diffracted interference signal to monitor AFM tip displacement, the noise level of the μSI is also expected to be approximated by this number.

Lee *et al.* [106] measured the total current noise density at 20 kHz as a function of the DC photocurrent generated by the PD which is the same one in the μSI as shown in Figure 120 with only the PD and HeNe laser. The measured noise floor of the signal analyzer and the amp combined is $0.41\text{pA}/\sqrt{\text{Hz}}$ at 20 kHz. Their measurement at 20 kHz showed that the relative intensity noise (RIN) of the light source, HeNe laser was negligible, so the optical detection could be shot-noise limited. By combining the PD with cMUT as shown in Figure 121, MDD was estimated as $2.08 \times 10^{-4} \text{\AA}/\sqrt{\text{Hz}}$ and $1.35 \times 10^{-4} \text{\AA}/\sqrt{\text{Hz}}$ at 20 kHz and 100 kHz, respectively as shown in Figure 122. It was noted that the mechanical vibration noise was represented at 20 kHz. Again, cMUT is a similar mechanical structure as the μSI , the overall number of the noise level of the μSI is expected to be approximated by this number. These MDD are still good by considering for example, 10^{-2}\AA at 10 kHz bandwidth and 1\AA at 1MHz bandwidth.

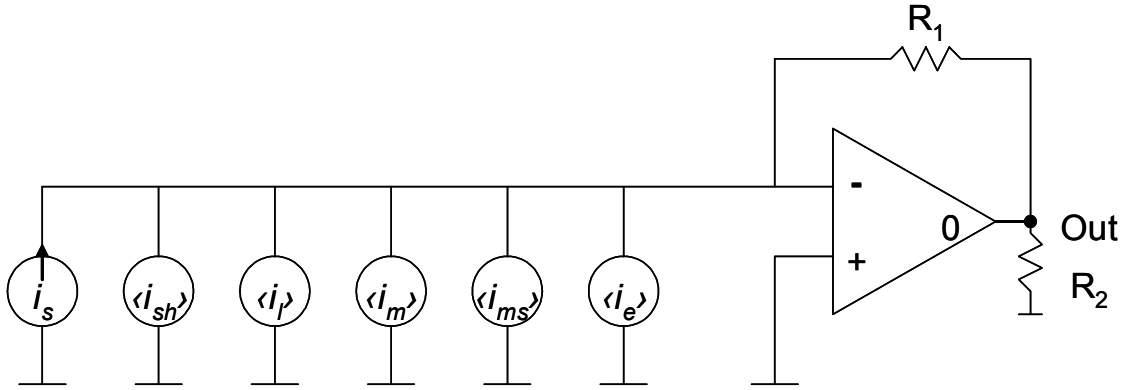


Figure 119. Electrical equivalent noise circuit

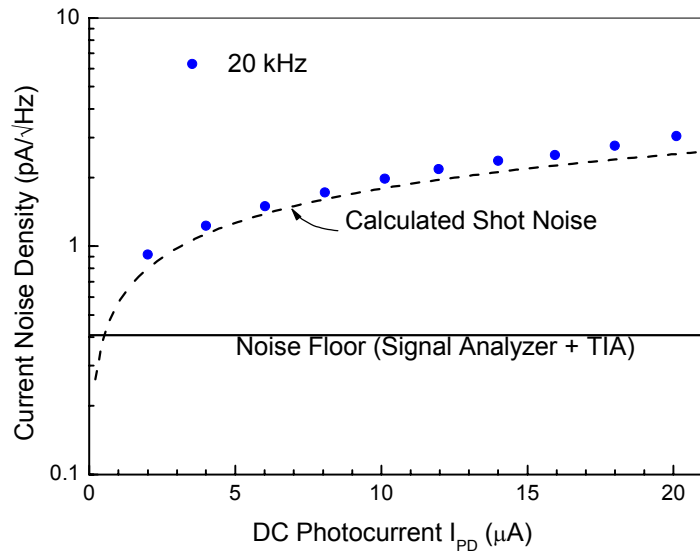


Figure 120. Noise density as a function of DC photocurrent measured at 20kHz [106]

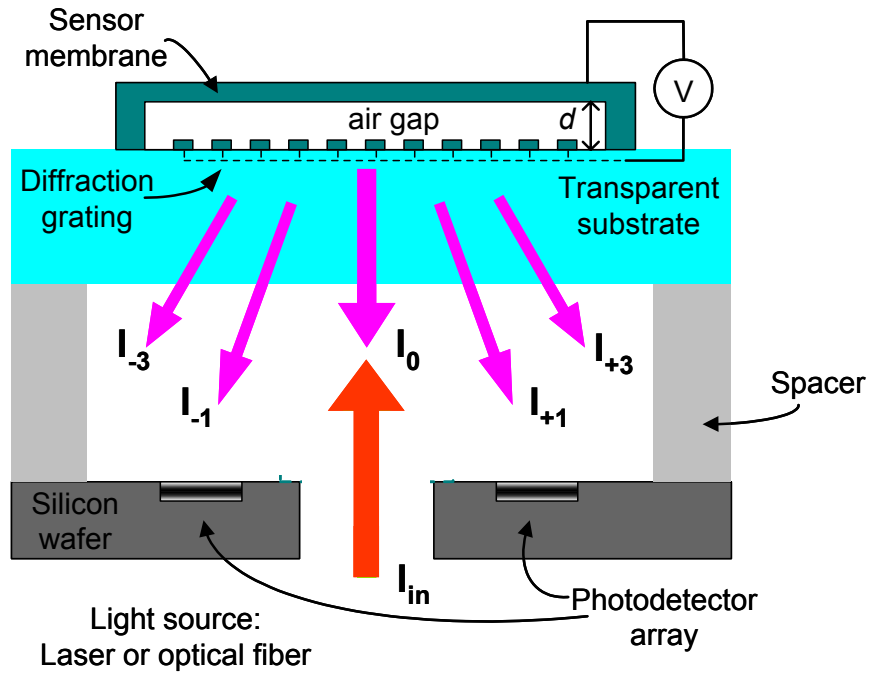


Figure 121. cMUT integrated with PD[106]

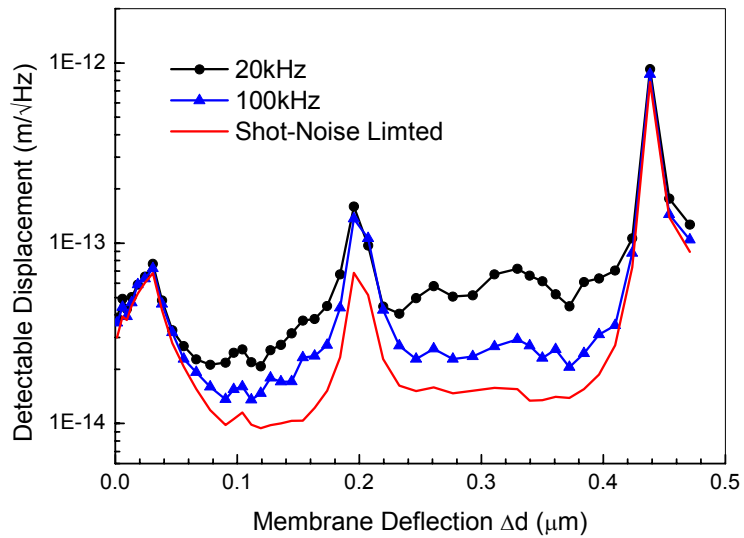


Figure 122. Measured minimum detectable displacement in the integrated acoustic sensor obtained at 20kHz and 100kHz. Also shown is the shot-noise limited detectable displacement for comparison [106]

5.7 EFFECT OF CONTROL

A proposed solution to vibration noises and misalignment is to actively control the distance from the measured surface to the grating in μSI . Typically, the intensity of the light at the first interference order is a function of the path difference between the grating and the target surface, as shown in a Figure 123. The fringes in Figure 105 and Figure 112 occur when the path difference between surface points passes over a peak of the curve, such as the one that occurs at $\lambda/4$. The point of highest sensitivity of the interferometer occurs within the most linear region of the optical intensity curve. If the path distance is controlled, all measurements can be taken at this point of highest sensitivity. Since the optical intensity curve is sinusoidal, the first derivative and second derivative are 90° and 180° , respectively, out of phase from the optical intensity curve. Thus, at the point of highest sensitivity, the second derivative of the optical intensity curve is zero. Therefore, the process variable for the control system must minimize the second derivative signal and use this as the set point for control [55]. This allows the system to lock onto a particular fringe of the optical curve and track with it as vibrations effect the system.

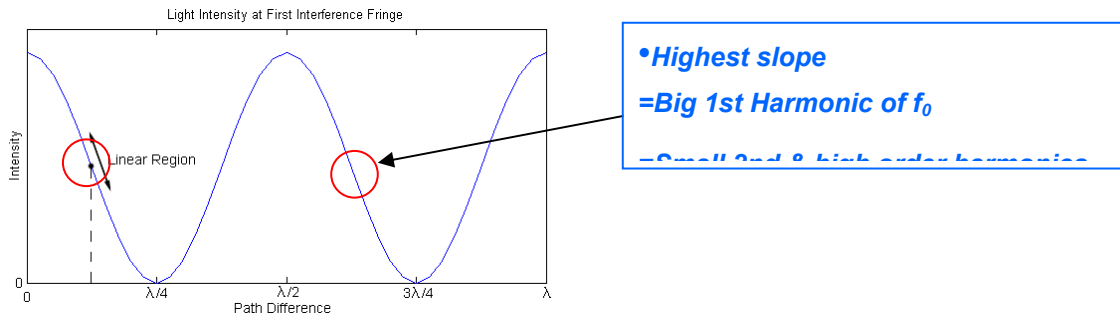


Figure 123. Typical optical intensity curve as a function of path difference

A block diagram of the control system is shown in Figure 124. A piezo actuator moves MEMS by control input to maintain the highest sensitivity of the measurement. This piezo actuator is replaced with deformable grating in integrated μ SI. The magnitude of the second harmonic, which is proportional to the second derivative of the optical intensity curve, is calculated through purely analog means via a phase sensitive detection (PSD). The piezo actuator is excited with a sinusoidal signal at frequency $f_0 = 10$ kHz, and the output from the photodetector contains f_0 , $2f_0$, and other harmonics. Also, noise is present at all frequencies. Multiplying the photo diode signal by a sinusoidal signal at $2f_0$, displaces the magnitude of the second harmonic in the signal to the DC level. The resultant signal is then low-pass filtered at 300 Hz, below which most mechanical vibrations occur. The DC level and low-frequency vibration signals are used for the error signal of the control system. A proportional-integral-differential (PID) controller is created on a field programmable gate array (FPGA) device to perform the control.

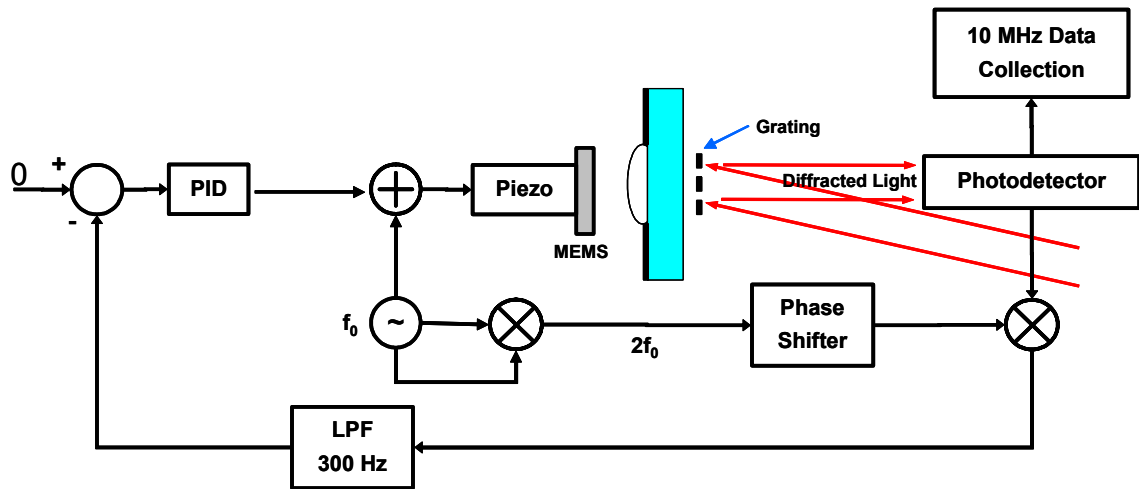


Figure 124. Control system block diagram

Testing of the control scheme is performed to validate its feasibility. The piezo actuator is excited with a fundamental frequency of $f_0 = 10$ kHz while the DC level was slowly ramped in a triangle wave from 0 to 4V. The amplitude of the optical intensity, the first harmonic, and the second harmonic, plotted in Figure 125 (a), (b), and (c), respectively, are detected using the PSD method described above. The first harmonic is 90° out of phase of the optical intensity, and the second harmonic is 180° out of phase, which shows good correlation with theory. If the set-point of the control system is placed at the midpoint of the second harmonic amplitude, then the actuator will keep the system within the linear region of the optical intensity curve as indicated by the vertical dashed line. Therefore, the PSD control scheme is suitable to maintain the interferometer at the point of maximum sensitivity.

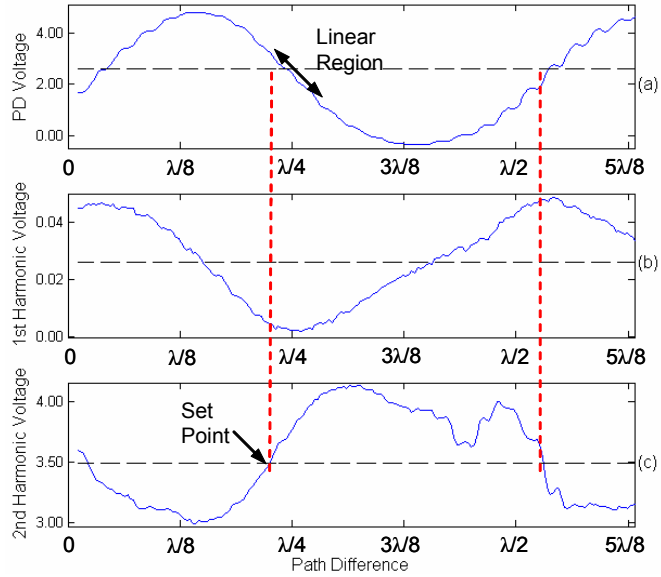


Figure 125. Measured optical intensity, first harmonic, and second harmonic curves as a function of path difference

The initial results from the use of the control system indicate that the magnitude of second harmonic signal at the output is reduced by nearly 70% while maintaining the same intensity at $f_0 = 11$ kHz, as shown in Figure 126. Yet, the power present in the other frequencies rose other indicating that the controller is introducing broad-band noise into the system, as shown in Figure 127. This can be corrected with better tuning and analog filtering.

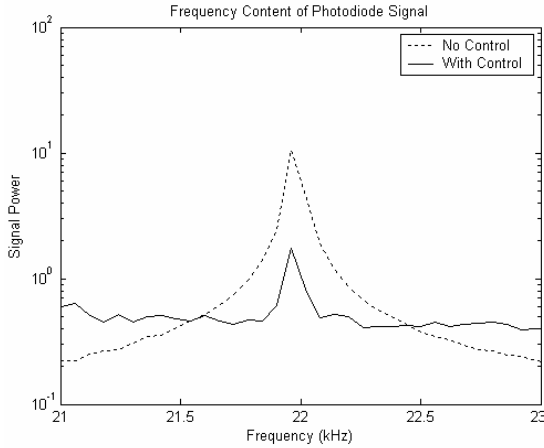


Figure 126. Power in the second harmonic

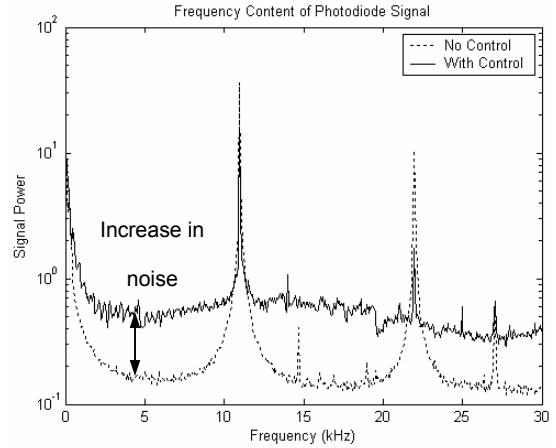
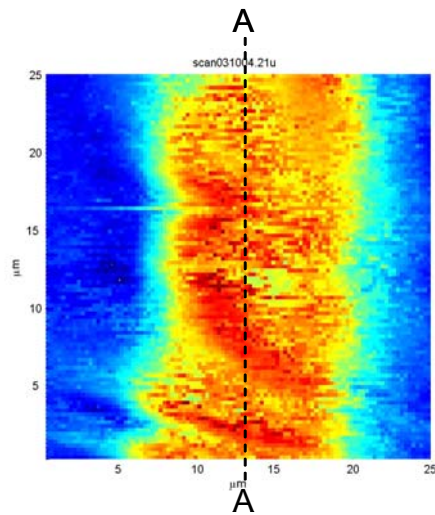
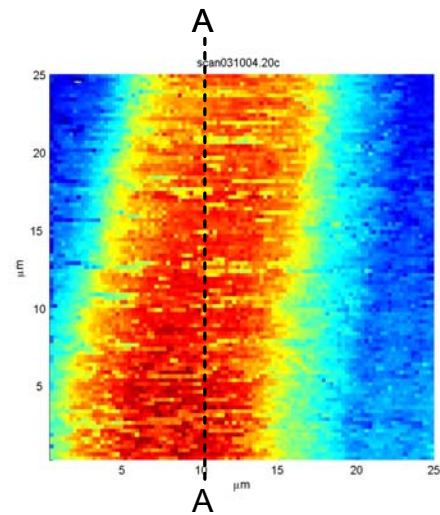


Figure 127. Power spectrum of the photodetector signal

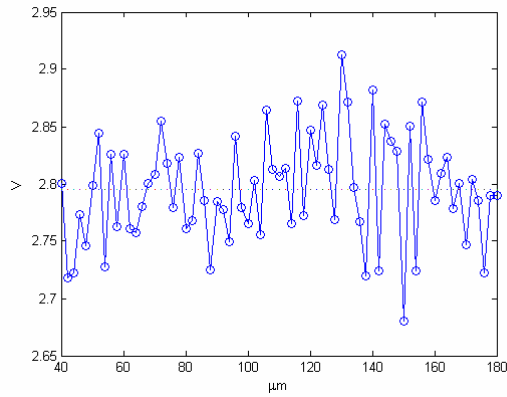
Figure 128 shows scanned results for the 20 μm wide aluminum line (a) with and (b) without the control. (c) and (d) show cross-section of each cases. RMSE is 0.0473V for uncontrolled case and 0.0349V for controlled case. Controlled results show the better image by less noise.



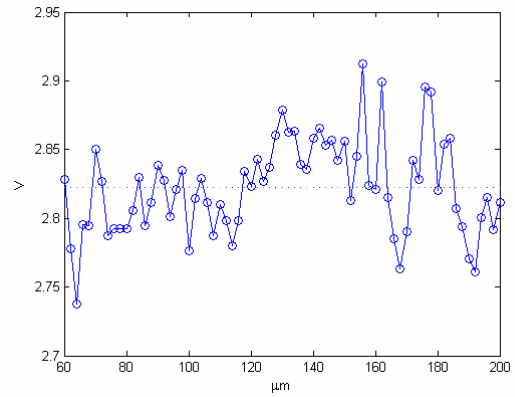
(a)



(b)



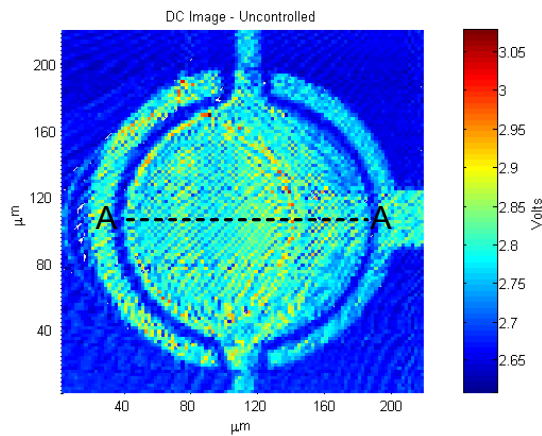
(c)



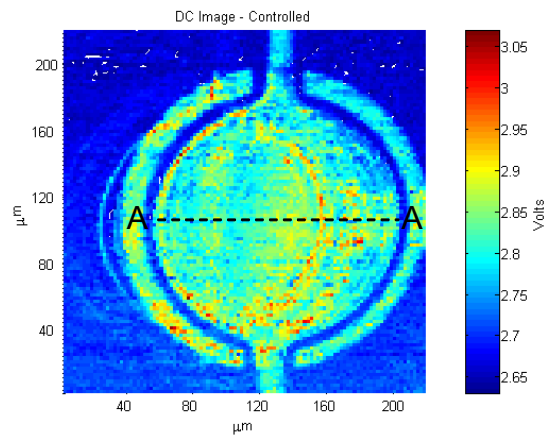
(d)

Figure 128. (a) A scanned trace without control (b) A scanned trace with control (c) Cross-section A-A in (a) (d) Cross-section A-A in (b)

Figure 129 shows scanned results for the static cMUT (a) with and (b) without the control. (c) and (d) show cross-section of each cases. RMSE is 0.0924V for uncontrolled case and 0.0840V for controlled case. Controlled results show the better image by less noise again.



(a)



(b)

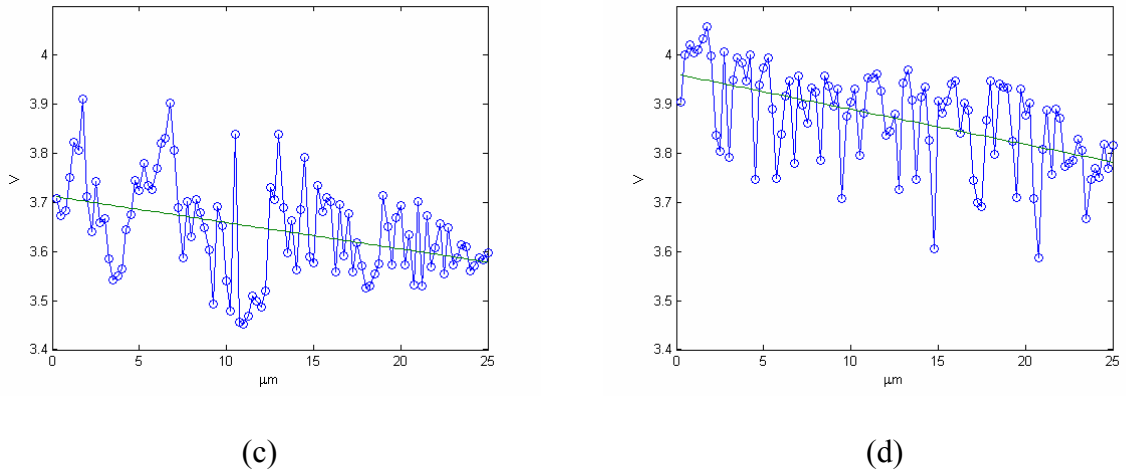


Figure 129. (a) A scanned cMUT without control (b) A scanned cMUT with control (c) Cross-section A-A in (a) (d) Cross-section A-A in (b)

A block diagram of the control system for the deformable grating is shown in Figure 130. The displacement of the grating is proportional to the square of the voltage applied due to capacitive forces. Therefore, an additional square-root function must be applied to the control output prior to being sent to the deformable grating.

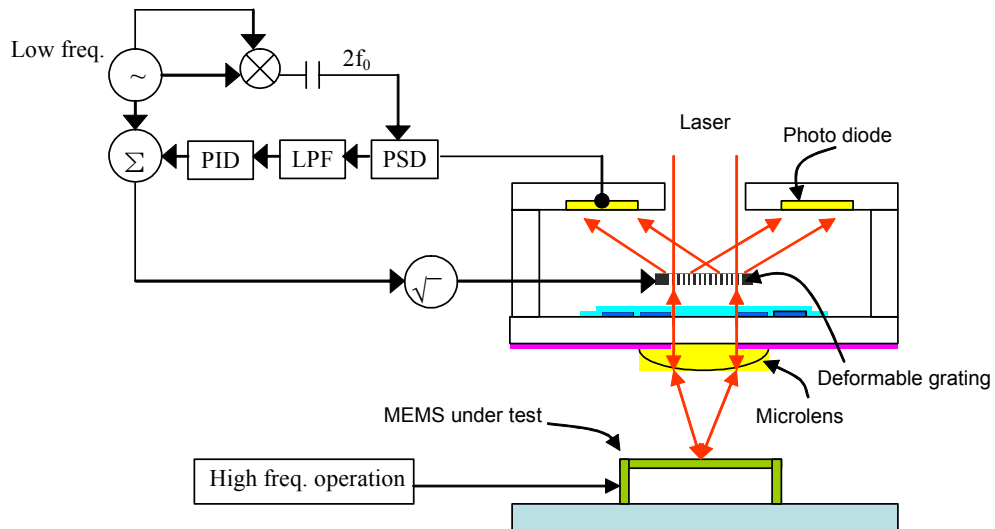


Figure 130. Control system block diagram

5.8 INTEGRATED SYSTEM

The assembled package was tested to see its operation while measuring vibration of a micromachined microphone having a diameter of 160 μ m. While the microphone is vibrating at 10 kHz by a 35 \pm 6V sine wave input, the deformable grating is actuated by a 16.5 \pm 10V, 40Hz triangular ramp input. Due to the interference between the reflected beam from the microphone and the grating while the grating is actuating, 10 kHz microphone signal is modulated on the 40Hz grating signal. The experiment set-up is the same as in Figure 107 and Figure 108. The measured signal in Figure 131 and the magnified signal in Figure 132 clearly show that 10 kHz signal is amplitude modulated. Since 40Hz ramp of the grating passes the different slope of the interference curve, this amplitude modulation of 10 kHz is shown. In this experiment, 40Hz ramp of the grating passes the highest slope of the interference curve in the middle of 0.125-0.13 sec and 0.14-0.145 in Figure 132. These results indicate that the grating actuation can tune the measurement of MEMS vibration at the highest slope, in other words, the maximum sensitive point. Figure 133 shows a grating signal and a cMUT signal from the same set-up but different vibration frequency. While the microphone is vibrating at 900 kHz by a 30 \pm 15V sine wave input, the deformable grating is actuated by a \pm 12.5V, 40Hz triangular ramp input. After decomposing the grating signal and cMUT signal from PD signal, cMUT signal shows high sensitivity at the high slope of the grating signal. 9V differences from A to B is equivalent to a quarter of the wavelength and the slope at C is $0.2(\text{V})/\{1.5\text{V}*(633\text{nm}/4/9\text{V})\}=0.00758$ (V/nm). Since the cMUT amplitude at C is 0.038V, the cMUT amplitude at C is calculated as $0.038/0.00758\approx 5\text{nm}$.

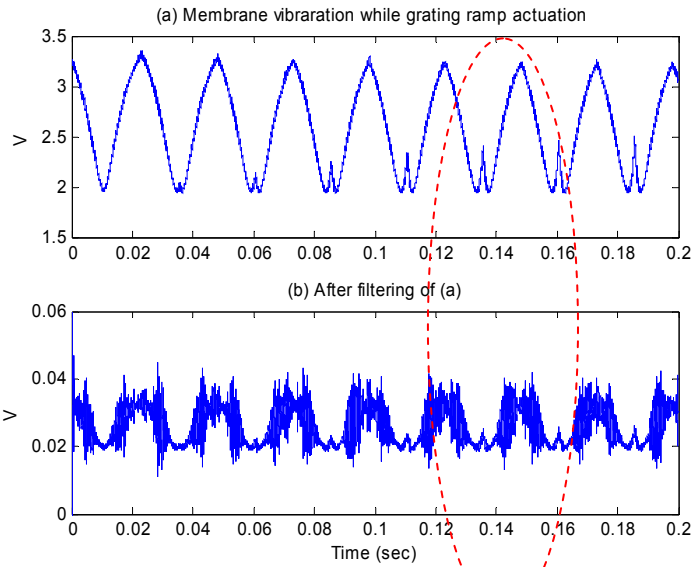


Figure 131. PD signal showing (a) 10kHz vibration on 40Hz ramp (b) after band pass filtering around 10kHz

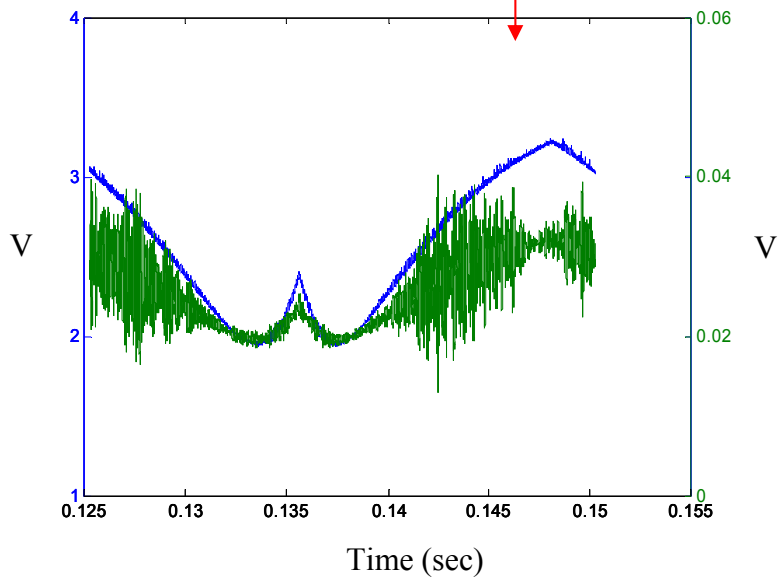


Figure 132. Magnified signals in 0.125-0.15 sec showing magnitude envelop that depends on measurement sensitivity

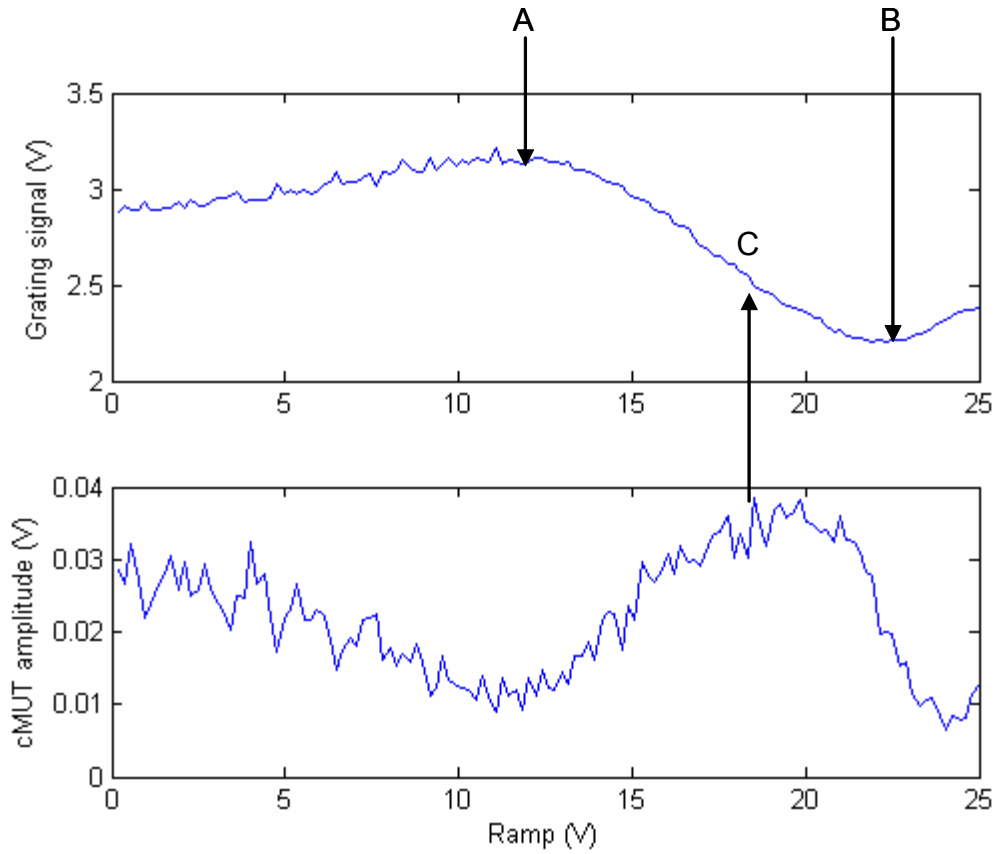


Figure 133. Decomposed grating and cMUT signal from PD signal at 900kHz vibration of cMUT

5.9 SUMMARY

The scanning results using a fixed grating μ SI demonstrated that it could measure vibration profile as well as static lateral. Due to the vibration noise and misalignment between MEMS under test and μ SI, the scanned results showed fringes and non-uniform profiles. These problems can be addressed by PID control of the distance from the grating

to the measurement surface to maintain the most sensitive measurement point. The integrated μ SI was successfully tested. This μ SI which is integrated with photo diodes demonstrated its operation by scanning a cMUT without control of the grating. The PID control scheme was presented and demonstrated its feasibility.

CHAPTER 6

DISCUSSION AND CONCLUSION

6.1 SUMMARY

The operating principle of the μ SI was simulated using angular spectrum theory and verified in a macro scale set-up experiment as well as in the micromachined interferometer. It is clear that these experimental results follow closely predicted simulation results in terms of diffraction and interference for distance monitoring.

Design parameters for the microlens and deformable grating were decided based on their adequate operation within certain limitations. A recipe for the designed microlens was developed and spherical microlenses were fabricated.

The designed and fabricated deformable grating satisfied following design constraints.

- The voltage for the electrostatic static force was within 50V.
- The working range of grating was larger than a half wavelength.
- The stiffness of the grating membrane gave an enough band width more than 10 kHz.
- The bottom electrode did not block the light source.

- The flat zone at illumination was sufficient to increase diffraction efficiency.

Since RIE equipment for aluminum etching in Microelectronics Research Center (MIRC) at Georgia Tech has been inconsistent in terms of etching rate and uniformity, it was unavoidable to get a low yield of the fabrication. The fabricated grating membrane was deformed due to thermal stress in the process. Mismatch of thermal expansion between the quartz wafer and the aluminum pattern caused this stress. Instead of a quartz wafer, a Pyrex glass could reduce the thermal stress since its thermal expansion coefficient is closer to the aluminum's. The integration of the PD, grating and lens is another hard process to get a good alignment. The alignment machine in PRC needs to be compensated its mechanical error that was sometimes inconsistent.

The scanning results using a fixed grating μ SI demonstrated that it could measure vibration profile as well as static vertical (less than a half wave length) and lateral dimension of MEMS. The μ SI, which is integrated with photo diodes, demonstrated its operation by scanning a cMUT without control of the grating. The PID control has been tested and resulted in improvement in scanned images. The integrated μ SI demonstrated that the deformable grating could be used to tune the measurement keep the interferometer in quadrature for highest sensitivity.

6.2 CONCLUSION

The fabricated μ SI satisfied design constraints. The operational principle was successfully demonstrated in the test using the fabricated μ SI. The fabricated deformable grating showed its capability for the optimization of the measurement. The scanning results demonstrate that this sensor is capable of providing feedback on a number of static dimensions of the MEMS device on the wafer plane as well as measuring out of plane vibration profiles in a broad frequency range exceeding 1MHz. The results show good correlation with CAD and analytic models. A proper control scheme based on a deformable grating interferometer with integrated electronics can be used to solve alignment and noise problems of the sensor and enable array operation. Since an individual μ SI can be packaged into volume of less than 3.5mm^3 and fabricated on a planar substrate, it offers the potential to perform fast, in-line, non-contact and precision static and dynamic measurements of MEMS structures. This is a necessary tool to increase the yield of MEMS manufacturing processes.

6.3 CONTRIBUTION

The μ SI is a novel sensor which can measure vibration profiles of microstructures. Its unique concept and design is already protected in two US patents. Its innovative concept can reduce the physical size of the inspection tool to several mm^2 . Reduced size is competitive in terms of space and cost. Parallel operation is also viable with this size.

Since the working principle only requires a diffracted signal from a detector, inspection speed can be faster than other methods using a CCD camera. The maximum vibration speed of the microstructures which μ SI can measure is limited by electronics rather than device itself.

It is important to monitor lateral dimensions on devices on a wafer in the process line. Since μ SI can provide lateral dimensions based on reflectivity of the surface, it can also be used to see different materials in adjacent patterns. Vertical dimension could be measured within a half wave length. This information is very useful to inspect MEMS during the manufacturing processes.

So far, MEMS quality inspection during the fabrication process has mainly depended on manual inspection by a microscope and final inspection of the end product. Demand for reliable and economic metrology solutions to inspect MEMS in a systematic fashion has increased as the volume of MEMS production increases. μ SI is very attractive in this case because it provides an in-line inspection solution which can measure wafers without removing them from the fabrication line. In-line solutions are also a core part of the integrated metrology strategy for the future mass fabrication of semiconductor and MEMS, as shown in Figure 134. In-line metrology which is combined with in-situ metrology can provide wafer inspection results between the processes. This information can be used by the process controller to compensate variations of the prior processed wafer.

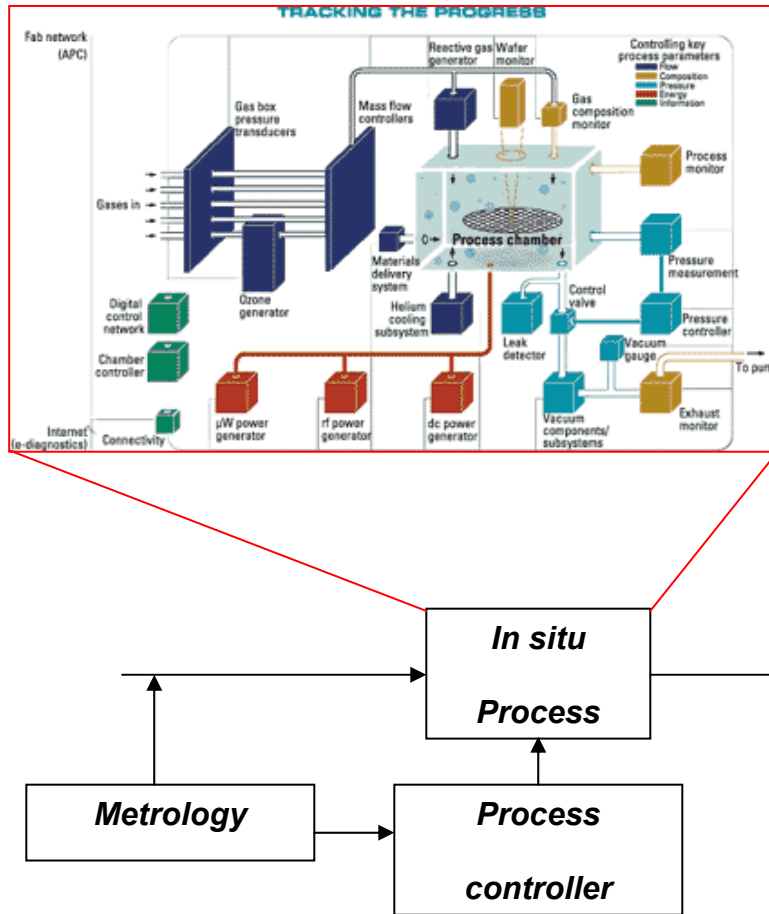


Figure 134. Integrated metrology in advanced process control

The design experience and optimized fabrication recipes for μ SI can be used to develop similar type of MEMS devices such as a polychromatic, a spectroscopy, and an infrared ray (IR) imager. Thus, because miniaturized devices using the same operation principle are required in many different fields, this developed recipe can reduce developing cost and time.

6.4 RECOMMENDATION AND FUTURE WORK

The fabrication of the deformable grating was a challenge due to limited equipment in MIRC. Since the design of the grating is tightly optimized, any variation of the etching process easily damaged the device and its performance. Thus, somewhat robust design would be recommended to allow the variation of the processes by the cost of performance if processes yield is important such as commercial products. For example, increasing grating size would help to increase the yield in RIE process. Illumination to the μ SI was quite difficult since 100 μ m aperture under the grating and 200 μ m hole in the PD only allows a collimated beam in that size as well as very good alignment. Thus, illumination problem needs to be further explored.

A PID controller has been developed to remove noise and correct the misalignment problem. Also, self-adjusting capability of the μ SI, used to adapt itself to different measurement environment such as temperature and pressure, needs this controller. Thus, demonstration of the scanning with the controller needs to be addressed.

Though the controller eliminates most of the noise sources, there is no noise free system. To increase the speed of the measurement, averaging of the measurements, which needs repeated scanning at the same point, is not desirable. Scanned images might be improved by image processing technology.

Array implementation requires combination of scanned data by each element. Since the μ SI measures relative distance by each cell, neighborhood elements need to measure the same spot to link scanned data. Though μ SI is designed to avoid optical cross-talk between neighborhood elements, experimental evaluation may be needed.

The μ SI can be expanded to an absolute distance measurement solution by combining it with confocal microscopy as shown in Figure 135. The focal length of the lens can be used to measure the distance by vertical scanning of μ SI. A piezo actuator and its driver can be used in this purpose.

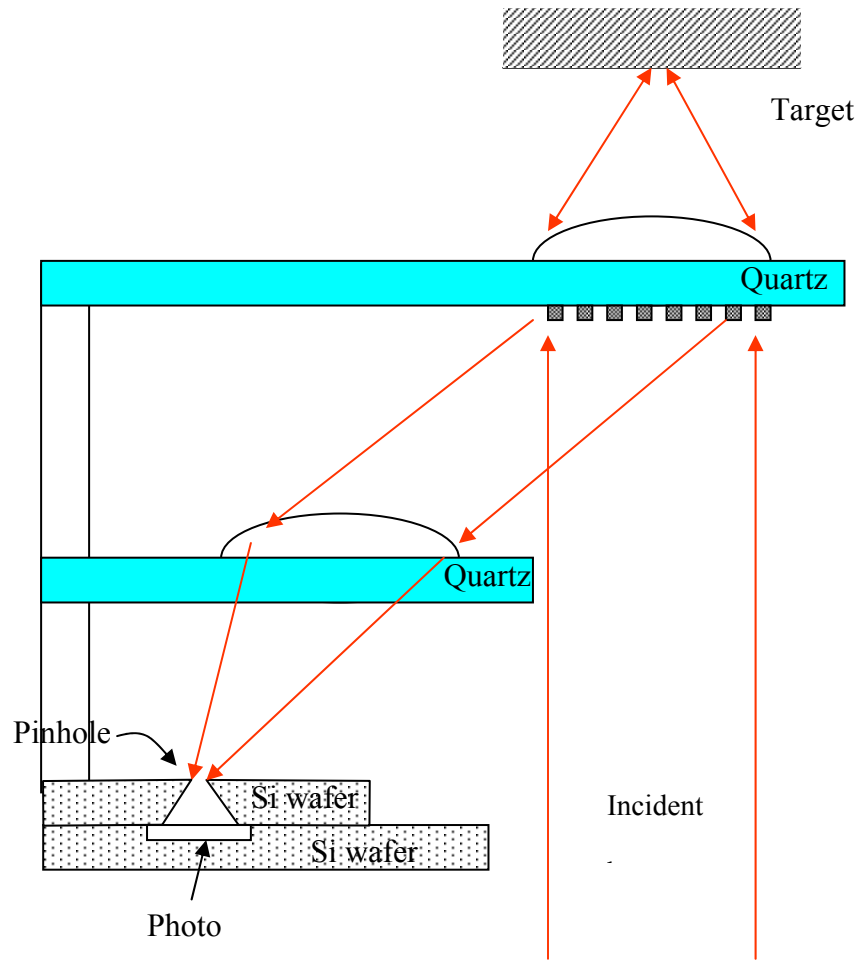


Figure 135. μ SI combined with confocal microscopy

APPENDICES

1. Numerical analysis of the bending equation (10) with constant residual stress, constant EI and constant f

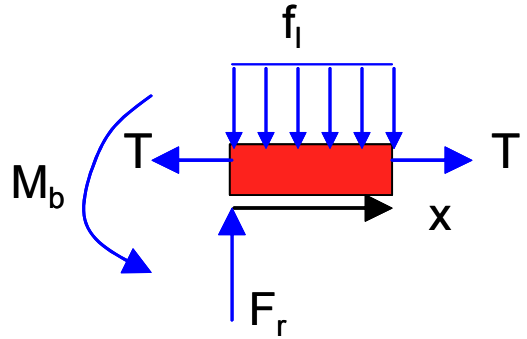
1) $0 < x < L_e$,

$$EI \frac{d^4 y}{dx^4} - T \frac{d^2 y}{dx^2} = f_l$$

$$EI \frac{d^3 y}{dx^3} - T \frac{dy}{dx} = f_l x + C_1$$

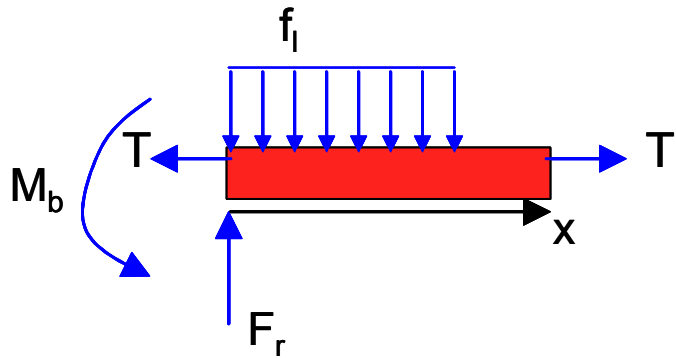
$$EI \frac{d^2 y}{dx^2} - Ty = \frac{1}{2} f_l x^2 + C_1 x + C_2$$

$$\Rightarrow EI \frac{d^2 y}{dx^2} - Ty = \frac{1}{2} f_l x^2 - F_r x + M_b$$



2) $L_e < x < L_m$,

$$\Rightarrow EI \frac{d^2 y}{dx^2} - Ty = -\frac{1}{2} f_l L_e^2 + M_b$$



All except M_b are known. Assume M_b and solve the equation numerically using 4th order Runge-Kutta Method [105] until to meet following boundary condition (5) within error boundary.

$$(1) x = 0, y = 0, (2) x = 0, \frac{dy}{dx} = 0$$

$$(3) y(L_e)|_{1)} = y(L_e)|_{2)}, (4) \frac{dy}{dx}(L_e)|_{1)} = \frac{dy}{dx}(L_e)|_{2)}$$

$$(5) \frac{dy}{dx}(L_m / 2) = 0$$

2. Deformable grating fabrication processes

a. Bottom electrode patterning by the lift-off process

i. PR mask patterning

- 1) Spin 1813 PR at 500rpm with ramp 500rpm/sec for 10sec and then, spin again 3000rpm with ramp 1000rpm/sec for 30sec
- 2) Softbake the spun 1813 PR for 3 min at 115C on the hotplate
- 3) Expose UV into softbaked 1813 PR for 120mJ at MA6 mask aligner with CI2 mode (405nm), vacuum contact, and gap of 20 μ m
- 4) Develop it in 319 developer for 1min

i. E-beam evaporation

- 1) 500 \AA thick Cr and right after 1000 \AA thick Al at 2×10^{-6} mTorr

ii. Lift-off process

- 1) Pour water into the ultra sonic bath up to indicated line
- 2) Put the wafer into a beaker with the pattern faced up and dip the beaker into the bath
- 3) Start the ultra sonic bath to give a vibration and then pour Acetone into the beaker
- 4) Look at the lift-off Al from the wafer. If the lift-off started, take the beaker out from the bath. Leave it until the lift-off is done.

- 5) Pour the Acetone carefully into the waste bottle in the hood.
- 6) To take out the wafer, turn the beaker upside down on the clean cleanroom tissue.
- 7) Clean the wafer with Acetone, methanol, and DI water.
- 8) Make it dry with Nitrogen gas gun.

b. Oxide insulator patterning

i. Oxide deposition by STS PECVD

Recipe; 2% SiH₄ 400 Scm, N₂O 1420 Scm, chamber pressure: 800mTorr, process temperature: 300C, RF power: 20W, process time: 3min 30sec

iii. PR mask patterning

- 1) Spin 1827 PR at 3000rpm with ramp 3000rpm/sec for 60sec
- 2) Softbake the spun 1827 PR for 7min at 115C on the hotplate
- 3) Expose UV into softbaked 1827 PR for 130mJ at MA6 mask aligner with CI2 mode (405nm), hard contact, and gap of 20 μ m
- 4) Develop it in 319 developer for 3min
- 5) Hardbake it for 15min at 120C in the oven

iv. Oxide etch by RIE

- 1) The standard recipe shows a 98 Å/min etch rate
- 2) Etch it for 28min

v. Remove PR

- 1) Soak it in Acetone
- 2) Soak it in 1112A PR remover for 1hr 30 min at 85C

- 3) To decide PR spinning speed for a grating sacrificial layer following estimation made; Required a gap from electrode to grating + etched quartz height if etched + Al height
- c. Aperture patterning at the other side
 - i. Aluminum DC sputter; process time: 400sec, 40% power
 - ii. PR mask patterning
 - 1) Spin 1827 PR at 3500rpm with ramp 3500rpm/sec for 60sec
 - 2) Softbake spun 1827 PR for 10min at 110C on the hotplate
 - 3) Expose UV into softbaked 1827 PR for 170mJ at MA6 mask aligner with CI2 mode (405nm), hard contact, and gap of 20 μ m
 - 4) Develop it in 319 developer for 40sec
 - iii. Al wet etching
 - 1) PAN etching at 50C
 - iv. PR removing by Acetone
 - d. Sacrificial layer patterning
 - i. PR mask patterning
 - 1) Spin 1827 PR at 3500rpm with ramp 3500rpm/sec for 60sec
 - 2) Softbake spun 1827 PR for 10min at 110C on the hotplate
 - 3) Expose UV into softbaked 1827 PR for 170mJ at MA6 mask aligner with CI2 mode (405nm), hard contact, and gap of 20 μ m
 - 4) Develop it in 319 developer for 40sec
 - 5) Hardbake it for 25min at 130C in the oven
 - e. Aluminum DC sputtering
 - i. Process time:3100sec, 40% power for 1.8 μ m deposition

Table 5. DC sputterer process time vs. aluminum deposition thickness

Process time (sec)	Al thickness (μm)
400	0.2
1500	0.8
2200	1.4
2900	1.7
3000-3100	1.7-1.8
3600	2.4

f. Thick center region patterning

i. PR mask patterning

- 1) Spin HMDS at 3000rpm with ramp 1000rpm/sec for 10sec
- 2) Spin 1827 PR at 3500rpm with ramp 2000rpm/sec for 60sec
- 3) Softbake spun 1827 PR for 5min at 85C in the oven
- 4) Expose UV into softbaked 1827 PR for 210mJ at MA6 mask aligner with CI2 mode (405nm), hard contact, and gap of 20 μm
- 5) Develop it 319 developer for 1min 30sec
- 6) Hard bake it for 7min at 85C in the oven

ii. RIE

- 1) Etch with standard Al etching recipe
BCl₃: 40sccm, Cl₂: 10sccm, CHCl₃: 3sccm, pressure: 30mTorr, Power: 125W for 6min 30sec for 0.95 μm etching
- 2) PR removed by Acetone and Methanol, and then rinse with DI water

g. Grating patterning

- i. PR mask
 - 1) Spin HMDS at 3000rpm with ramp 1000rpm/sec for 10sec
 - 2) Spin 1827 PR at 3500rpm with ramp 2000rpm/sec for 60sec
 - 3) Softbake spun 1827 PR for 5min at 85C in the oven
 - 4) Expose UV into softbaked 1827 PR for 210mJ at MA6 mask aligner with CI2 mode (405nm), hard contact, and gap of 20 μ m
 - 5) Develop it 319 developer for 1min 30sec
 - 6) Hard bake it for 7min at 85C in the oven
 - 7) Dice the whole wafer into nine pieces
- ii. RIE
 - 1) Etch each diced piece with anisotropic Al etching recipe
BCl₃: 40sccm, Cl₂: 10sccm, CHCl₃: 3sccm, pressure: 10mTorr, Power: 300W for 4min 30sec
 - 2) Soak in 1165A PR remover 5 days at 70C
- iii. Release at super critical drier

BIBLIOGRAPHY

- [1] K. Panetta, N. Aluru, S. Bart, S. Blanton, K. Böhringer, and R. Brown, "ITC 2000 Panel Discussion: Testing Challenges for MEMS," *Proceedings of ITC International Test Conference*, pp. 1130-1135 October 3-5, 2000.
- [2] S. D. Senturia, "Microsystem Design," Kluwer Academic Publishers, 2002.
- [3] R. Grace, "Commercialization issues of MEMS/MST/Micromachines: An Updated Industry Report Card on the Barriers to Commercialization," *NSF Nanotechnology Manufacturing Workshop*, Birmingham, Alabama, January 5, 2003.
- [4] J. Herrnsdorf, "Cost Controlling, also in MEMS a key to Success," Commercialization of Microsystems, Oxford, UK, September 2-6, 2001.
- [5] D. Nagel and M. Zaghoul, "MEMS: Micro Technology, Mega Impacts," *Circuits and Devices*, March, 2001.
- [6] L. E. St. Clair, A. R. Mirza, and P. Reynolds, "Metrology for MEMS Manufacturing," *Sensors Magazine*, Vol. 17, No. 7, July 2000.
- [7] P. Seitz, "Real-Time Optical Metrology for Microsystem Fabrication," *Proceedings of SPIE*, Vol. 3825, pp. 104-110, June 15-19, 1999.
- [8] A. Holzkecht, "Automated Test Requirement for Optical MEMS," *Proceedings of Sensor's Expo Technical Conference*, Chicago, IL, June 5-7, 2001.
- [9] A. B. Braun, "Integrated Metrology Encounters Grudging Acceptance," *Semiconductor International*, April 2003.
- [10] B. Kim, H. A. Razavi, F. L. Degertekin, and T. R. Kurfess, "Microinterferometer for Noncontact Inspection of MEMS," *The 3rd International Workshop on Microfactories*, pp. 77-80, Minneapolis, Minnesota, September 16-18, 2002.
- [11] J. A. Bosch, "Coordinate Measurement Machines and Systems," Marcel Dekker Inc., New York, NY, 1995.
- [12] G. Peggs, A Lewis, and R. Leach, "Measuring in three dimensions at the mesoscopic level," *ASPE Winter topical meeting*, pp. 53-57, Gainesville, Florida, January 22-23, 2003.

- [13] G. Peggs, A Lewis, and S. Oldfield, "Design for a compact high-accuracy CMM," *CIRP Annals*, 48(1), pp. 417-420, 1999
- [14] Y. Takaya, H. Shimizu, S. Takahashi, and T. Miyoshi, "Fundamental study on the new probe technique for the nano-CMM based on the laser trapping and Mirau interferometer," *Measurement*, Vol. 25, pp.9-18, 1999.
- [15] Y. Takaya, S. Takahashi, T. Miyoshi, and K. Saito, "Development of the nano-CMM probe based on laser trapping technology," *CIRP Annals*, 48(1), pp. 421-424, 1999.
- [16] J. Reilly, "Stylus profiler monitors chemical mechanical planarization performance," *Advanced Semiconductor Manufacturing Conference and Workshop*, pp. 320 -322, November, 14-16, 1994.
- [17] Y. Tai, R. S. Muller, "Measurement of Young's modulus on microfabricated structures using a surface profiler," *Proceedings of Micro Electro Mechanical Systems*, pp. 124-152, February 11-14, 1990.
- [18] E. Lebrasseur, J. Pourciel, T. Bourouina, M. Ozaki, T. Masuzawa, and H. Fujita, "Microsystem for Vertical Profile Measurement of High Aspect-ratio Microstructures," *Transducers*, Munich, Germany, June 10-14, 2001.
- [19] T. Sulchek, R. J. Grow, G. G. Yaralioglu, S. C. Minne, C. F. Quate, S. R. Manalis, A. Kiraz, A. Aydine, and A. Atalar, "Parallel atomic force microscopy with optical interferometric detection," *Applied Physics Letter*, Vol. 78, pp. 1787-1789, 2001.
- [20] S. R. Manalis, S. C. Minne, A. Atalar, and C. F. Quate, "Interdigital cantilevers for atomic force microscopy," *Applied Physics Letter*, Vol. 69, pp. 3944-3946, 1996.
- [21] S. Alexander, L. Hellems, O. Marti, J. Schneir, V. Elings, P. K. Hansma, Matt Longmire, and John Gurley, "An atomic-resolution atomic-force microscope implemented using an optical lever," *Journal of Applied Physics*, Vol. 65, pp. 164-167, 1989.
- [22] T. Bosch and M. Lescure, Eds., "Selected Papers on Laser Distance Measurement," *SPIE Milestone Series*, Vol. MS 115, SPIE Optical Engineering Press, Bellingham, WA, 1995.
- [23] F. Chen, G.M. Brown, and M. Song, "Overview of Three-dimensional Shape Measurement Using Optical Methods," *Optical Engineering*, 39(1), pp. 10-22, January 2000.

- [24] M. Amann, T. Bosch, M. Lescure, R. Myllylä, and M. Rioux, "Laser ranging: a critical review of usual techniques for distance measurement," *Optical Engineering*, 40(1), pp. 10-19, January 2001.
- [25] D.S. Pierce, T.S. Ng, and B.R. Morrison, "A Novel Laser Triangulation Technique for High Precision Distance Measurement," *Industry Application Society Annual Meeting*, Vol. 2, pp.1762-1769, 1992
- [26] T. Oka, H. Nakajima, A. Shiratsuki, M. Tsugai, U. Wallrabe, U. Hollenbach, P. Krippner, and J. Mohr, "Development of a micro-optical distance sensor with electrical I/O interface," *Transducer*, Munich, Germany, June 10-14, 2001.
- [27] K. Engelhardt and G. Häusler, "Acquisition of 3-D data by focus sensing," *Applied optics*, Vol. 27, No. 22, November, 1988.
- [28] R. Day, E. Lacot, F. Stoeckel, and B. Berge, "Three-dimensional sensing based on a dynamically focused laser optical feedback imaging technology," *Applied Optics*, Vol. 40, No. 12, pp.1921-1924, April, 2001.
- [29] S. K. Gordon and R. C. Timothy, "Confocal scanning optical microscopy," *Physics Today*, pp. 55-62, September, 1989.
- [30] J. Migot and C. Gorecki, "Measurent of surface roughness: comparison between a defect-of-focus optical technique and the classical stylus technique," *Wear*, Vol. 87, pp.39-49, 1983.
- [31] G. Udupa, M. Singaperumel, R. S. Sirohl, and M. P. Kothiyal, "Cauterization of surface topography by confocal microscopy: I. Principles and the measurement system," *Measurement Science Technology*, Vol. 11, pp. 305-314, 2000.
- [32] G. Udupa, M. Singaperumel, R. S. Sirohl, and M. P. Kothiyal, "Cauterization of surface topography by confocal microscopy: II. The micro and macro surface irregularities," *Measurement Science Technology*, Vol. 11, pp. 315-329, 2000.
- [33] W. Piyawattanametha, P. R. Patterson, G. D. J. Su, H. Toshiyoshi, and M. C. Wu, "A MEMS Non-interferometric Diffrencial Confocal Scanning Optical Microscope," *Transducer*, Munich, Germany, June 10-14, 2001.
- [34] J. Wyant and K. Prettyjohns, "Three-dimensional surface metrology using a computer controlled non-contact instrument," *SPIE, Optical Testing and Metrology*, Vol. 661, pp. 292-295, 1986

- [35] K. Creath, "Measuring step heights using an optical profiler," *SPIE, Optical Testing and Metrology*, Vol. 661, pp. 296-301, 1986
- [36] D. K. Hamilton and C. J. R. Sheppard, "A confocal interference microscope," *OPTICA ACTA*, Vol.29, No.12, pp. 1573-1577, 1982.
- [37] M. Davison, K. Kaufman, and I. Mazor, "First Results of a Product Using Coherence Probe Imaging for Wafer Inspection," *Proc. Soc. Photo-Opt. Instrum. Eng.*, Vol. 921, pp. 100-114, 1988
- [38] M. Davison, K. Kaufman, I. Mazor, and F. Cohen, "An Application of Interference Microscopy to Integrated Circuit Inspection and Metrology," *Proc. Soc. Photo-Opt. Instrum. Eng.*, Vol. 775, pp. 233-247, 1987
- [39] B. S. Lee, and T. C. Strand, "Profilometry with a coherence scanning microscope," *Applied Optics*, Vol. 29, No. 26, pp. 3784-3788, 1990.
- [40] T. Dresel, G. Häusler, and H. Venzke, "Three-dimensional sensing of rough surface by coherence radar," *Applied Optics*, Vol. 31, No.7, pp. 919-925, 1992.
- [41] J. Yi, S. Kim, and Y. Kwak, "A nanometric displacement measurement method using the detection of fringe peak movement," *Measurement Science Technology*, Vol. 11, pp. 1352-1358, 2000.
- [42] W. Hemmert, M. S. Mermelstein, and D. M. Freeman, "Nanometer resolution of three-dimensional motions using video interference microscopy," *12th IEEE International Conference on MEMS*, pp. 302-308, 1999.
- [43] D. Rugar, H. J. Mamin, and P. Guethner, "Improved fiber-optic interferometer for atomic force microscopy," *Applied Physics Letter*, Vol. 55, pp. 2588-2590, 1989.
- [44] Y. Joulrin, J. Jay, and O. Parriaux, "Compact diffractive interferometric displacement sensor in reflection," *Journal of the International Society for Precision Engineering and Nanotechnology*, Vol. 26, pp. 1-6, 2002.
- [45] F. L. Degertekin, N. A. Hall, and W. Lee, "Capacitive micromachined ultrasonic transducers with integrated optoelectronic readout," *IEEE Ultrasonics Symposium*, pp.875-881, 2001.
- [46] N.A. Hall and F.L. Degertekin, "Integrated optical interferometric detection method for micromachined capacitive acoustic transducers," *Applied Physics Letters*, Vol. 80, pp. 3859-61, 2002.

- [47] M. Mino, "Position Sensing Grating Interferometer for a Specular Object," *Optical Review*, Vol. 5, No. 3, pp.191-195, 1998.
- [48] K. Kamiya, T. Nomura, S. Okuda, H. Tashiro, and K. Yoshikawa, "Position-Sensing Grating Interferometer For a Specular Object-Analysis considering the aberration-," *Proc. SPIE* Vol. 4416, pp. 416-419, 2001.
- [49] C. Q. David and D. M. Freeman, "Using a Light Microscope to Measure Motions with Nanometer Accuracy," *Optical Engineering*, Vol. 37, pp. 1299-1304, 1998.
- [50] M. R. Hart, R. A. Conant, K. Y. Lau, and R. S. Muller, "Stroboscopic Interferometer System for Dynamic MEMS Characterization," *Journal of MEMS*, Vol. 9, pp. 409-418, 2000.
- [51] C. Rembe and R. S. Muller, "Measurement System for Full Three-Dimensional Motion Characterization of MEMS," *Journal of MEMS*, Vol. 11, No.5, pp. 479-488, 2002.
- [52] E. Novak, D. Wan, P. Unruh, J. Schmit, "Dynamic MEMS Measurement Using a Strobed Interferometric System with Combined Coherence Sensing and Phase Information," *ASPE Winter Topical Meeting*, pp. 104-107, Gainesville, Florida, January 22-23, 2003.
- [53] T. Stievator, W. Rabinovich, H. Newman, J. Ebel, R. Mahon, D. McGee, and P. Goetz, "Microcavity Interferometry for MEMS Device Characterization," *Journal of MEMS*, Vol. 12, pp. 109-116, 2003
- [54] R. A. Rawton *et al.*, "MEMS characterization using scanning laser vibrometer," *Proc. SPIE Symposium Microelectronic Manufacturing*, 1999.
- [55] J. E. Graebner, "Optical Scanning Interferometer for Dynamic Imaging of High-Frequency Surface Motion", *IEEE Ultrasonics Symposium*, pp. 733-736, 2000.
- [56] J. E. Graebner, H. F. Safar, B. Barber, P. L. Gammel, J. Herbsommer, L. A. Fetter, J. Pastalan, H. A. Huggins, and R. E. Miller, "Optical Mapping of Surface Vibrations on a Thin-Film Resonator near 2 GHz," *Ultrasonics Symposium*, pp. 635-638, 2000.
- [57] J. E. Graebner, B. Barber, P. L. Gammel, D. S. Greywall, and S. Gopani, "Dynamic visualization of subangstrom high-frequency surface vibrations," *Applied Physics Letters*, Vol. 78, pp. 159-161, 2001.
- [58] www.veeco.com

- [59] www.polytec.com
- [60] D Daly, "Microlens Arrays," Taylor & Francis, 2001.
- [61] N.F. Borrelli, "Microoptics Technology," Marcel Dekker, 1999
- [62] X. Shen and L Lin, "Micro Plastic Embossing Process: Experimental and Theoretical Characterizations," *Transducers*, Munich, Germany, June 10-14, 2001.
- [63] H. Sankur, E. Motamedi, R. Hall, W.J. Gunning, M. Khoshnevisan, "Fabrication of refractive microlens arrays," *Proc. SPIE, Micro-Optics/Micromechanics and Laser Scanning and Shaping*, Vol. 2383, pp. 179-183, 1995.
- [64] Z.D. Popovic, R.A. Sprague, and G.A. Neville Connell, "Technique for monolithic fabrication of microlens arrays," *Applied Optics*, 27(7), pp. 1281-1284, April 1988.
- [65] N.J. Phillips and C.A. Barnett, "Micro-optic studies using photopolymers," *Proc. SPIE, Miniature and Micro-Optics*, Vol. 1544, pp.10-21, 1991.
- [66] P. Nussbaum, R. Völkel, H. Herzig, M. Eisner, and S. Haselbeck, "Design ,fabrication and testing of microlens arrays for sensors and Microsystems," *Pure Applied Optics*, Vol. 6, pp. 617-636, 1997.
- [67] D. L. MacFarlane, V. Narayan, J. A. Tatum, W. R. Cox, and D. J. Hayes, "Microproject Fabrication of Microlens Arrays," *IEEE Photonics Technology Letters*, Vol. 6, No. 9, September, 1994.
- [68] C.R. King, L.Y. Lin and M.C. Wu, "Out-of-Plane Refractive Microlens Fabricated by Surface Micromachining," *IEEE Photonics Technology Letters*, 8(10), pp. 1349-1351, October 1996.
- [69] T. Shiono, K. Setsune, O. Yamazaki, and K. Wasa, "Rectangular-apertured micro-Fresnel lens array fabricated by electron-beam lithography," *Applied Optics*, Vol. 26, No. 3, pp. 587-591, February, 1987.
- [70] J. Jahns and S. J. Walker, "Two-dimensional array of diffractive microlenses fabricated by thin film deposition," *Applied Optics*, Vol. 29, No. 7, pp.931-936, March, 1990.
- [71] M. Haruna, M. Takahashi, K. Wakahayashi, and H. Nishihara, "Laser beam lithographed micro-Fresnel lenses," *Applied Optics*, Vol. 29, No. 34, pp.5120-5126, December, 1990.

- [72] M. C. Wu, L. Lin, S. Lee, and K. S. J. Pister, "Micromachined free-space integrated micro-optics," *Sensors and Actuators A*, Vol. 50, pp.127-134, 1995.
- [73] X. Zhang, Q. Tang, X. Yi, Z. Zhang, and X. Pei, "Cylindrical microlens array fabrication by argon ion-beam etching," *Optical Engineering*, Vol. 39, No. 11, pp. 3001-3007, November 2000.
- [74] S. Park, H. Jeon, Y. Sung, and G. Yeom, "Refractive sapphire microlenses fabricated by chlorine-based inductively coupled plasma etching," *Applied Optics*, Vol. 40, No. 22, pp.3698-3702, August 2001.
- [75] M.G. Moharam, T.K. Gaylord, G.T. Sincerbox, H. Werilich, and B. Yung, "Diffraction characteristics of photoresist surface-relief gratings," *Applied Optics*, Vol. 23, No. 18, pp. 3214-3220, September 1984.
- [76] R. C. Enger and S. K. Case, "High-frequency holography transmission grating in photoresist," *Journal of Optical Society of America*, Vol. 73, No. 9, pp. 1113-1118, September 1983.
- [77] P. Ehbets, H. P. Herzig, P. Nussbaum, P. Blattner, and R. Dändliker, "Interferometric fabrication of modulated submicrometer grating in photoresist," *Applied Optics*, Vol. 34, No. 14, pp. 2540-2547, 1995.
- [78] A. G. Lopez and H. G. Craighead, "Subwavelength surface-relief gratings fabrication by microcontact printing of self-assembled monolayers," *Applied Optics*, Vol. 40, No. 13, pp. 2068-2075, May 2001.
- [79] A. Schilling and H. P. Herzig, "Phase function encoding of diffractive structures," *Applied Optics*, Vol. 39, No. 29, pp. 5273-5279, October 2000.
- [80] G. T. A. Kovacs, "Micromachined Transducers," McGraw-Hill, 1998.
- [81] G. M. Hocker, D. Youngner, E. Deutsch, A. Volpicelli, S. Senturia, M. Butler, M. Sicclair, T. Plowman, and A. J. Picco, "The Polychromator: A programmable MEMS Diffraction Grating for Synthetic Spectra," *Solid-State Sensor and Actuator Workshop*, Hilton Head Island South Carolina, pp. 89-91, June 2000.
- [82] E. S. Hung and S. D. Senturia, "Extending the Travel Range of Analog-Tuned Electrostatic Actuators," *Journal of MEMS*, Vol. 8, No. 4, pp. 497-505, December, 1999.
- [83] D. M. Bloom, "The Grating Light Valve: revolutionizing display technology," *Proceedings of SPIE*, Vol. 3013, pp.165-171, February 10-12, 1997.

- [84] S. R. Kubota, "The grating light valve projector," *Optics and Photonics News*, September 2002.
- [85] R. W. Corrigan, D. T. Amm, P. A. Alioshin, B. Staker, D. A. Lehoty, K. P. Gross, and B. R. Lang, "Calibration of a Scanned Linear Grating Light Valve Projection System," *SID International Symposium, Digest of Technical Papers*, pp. 220-223, May, 1999.
- [86] O. Solgaard, F. S. A. Sandejas, and D. M. Bloom, "Deformable grating optical modulator," *Optics Letters*, Vol. 17, No. 9, pp. 688-690, May, 1992.
- [87] M. Mehregany, S. D. Senturia, J. H. Lang, and P. Nagarkar, "Micromotor fabrication," *IEEE Transactions on Electron Devices*, Vol. 39, No. 9, pp. 2060-2069, September 1992.
- [88] C. Kim, A. P. Pisano, and R. S. Muller, "Silicon-Processed Overhanging Microgripper," *Journal of MEMS*, Vol. 1, No. 1, pp. 31-36, March, 1992.
- [89] J. N. Randall, C. Goldsmith, D. Denniston, and T. Lin, "Fabrication of Micromechanical Switches for Routing Radio Frequency Signals," *Journal of Vacuum Science and Technology*, Vol. B14, No. 6, pp. 3692-3696, November/December, 1996.
- [90] E. R. Deutsch, "Achieving large stable vertical displacement in surface-micromachined MEMS," *Ph.D. Thesis*, MIT, 2002.
- [91] E. P. Furlani, E. H. Lee, and H. Luo, "Analysis of grating light valves with partial surface electrodes," *Journal of Applied Physics*, Vol. 83, No. 2, pp. 629-634, 1998.
- [92] G. G. Yaralioglu, A. Atalar, S. R. Manalis, and C. F. Quate, "Analysis and design of an interdigital cantilever as a displacement sensor," *Journal of Applied Physics*, Vol. 83, No. 12, pp. 7405-7415, June 1998.
- [93] ZMI 4004, and 2000 data sheet, www.zygo.com
- [94] J.W. Goodman, "Introduction to Fourier Optics," McGraw-Hill, 1996
- [95] W. Lee and F. L. Degertekin, "Rigorous Coupled-Wave Analysis of Multilayered Grating Structures," *IEEE Journal of Lightwave Technology*, to be published.
- [96] W. Lee and F. L. Degertekin, "Rigorous coupled-wave analysis for multilayered grating structures," *Proceedings of 2003 Symposium on Integrated Optics: Devices, Materials, and Technologies VII*, vol. 4987, pp. 264-273, 2003.

- [97] K. Lizuka, "Engineering Optics," Springer-Verlag, 1983
- [98] Zygo NewView 200 interferometer, www.zygo.com
- [99] K. M. Shilling, "Two dimensional analysis of mesoscale parts using image processing techniques," *Master thesis*, Georgia Tech, 2002.
- [100] J. C. Bravman, et al., "Thin films: stresses and mechanical properties," *MRS Symposium proceeding*, **Vol. 130**, 1988.
- [101] W. Lewis, "Thin film and surface," The English University Press Ltd., 1946.
- [102] <http://www.gmassoc.com>
- [103] Y. Yang, M. Gretillat, S.D. Senturia, "Effect of air damping on the dynamics of nonuniform deformations of microstructures," *TRANSDUCERS '97, 1997 International Conference on Solid State Sensors and Actuators*, **Vol. 2**, pp. 1093 – 1096, 1997.
- [104] W. Lee, N. Hall and F.L. Degertekin, "Micromachined Acoustic Sensor Array with Diffraction-Based Optical Interferometric Detection," *Proceedings of SPIE Symposium on MOEMS Display and Imaging Devices*, **Vol. 4985**, pp. 140-151, 2003
- [105] J. D. Hoffman, "Numerical Methods for Engineers and Scientists," McGraw-Hill, Inc. New York, 1993
- [106] W. Lee, N. A. Hall, Z. Zhou, and F. L. Degertekin, "Fabrication and characterization of a micromachined acoustic sensor with integrated optical readout," *IEEE Journal of Selected Topics in Quantum Electronics*, May/June, 2004.